Energy Balance Models with Realistic Albedo, Monthly Insolation, Milankovitch Cycles, and Simplified Earth-Like Planetary Modeling

A Thesis submitted in partial fulfillment of the requirements for the degree of Master of Science at George Mason University

by

Christian Johann Taubenberger
Bachelor of Science
George Mason University, 2017

Director: Linda A. Hinnov, Professor
George Mason University

Fall Semester 2020
George Mason University
Fairfax, VA

Copyright 2020 Christian Johann Taubenberger
All Rights Reserved

DEDICATION

ACKNOWLEDGEMENTS

First and foremost, I am deeply grateful to my committee chair, Dr. Linda Hinnov, for her assistance at every stage of the research project, and guidance and suggestions throughout my time at George Mason University. My heartfelt thanks also go out to committee members, Dr. Stacey Verardo and Dr. Natalie Burls, along with everyone else in the AOES and GGS departments who helped me define my path forward. Finally, I would like to express my gratitude to my parents, grandmother, friends, and my fiancée, whose support, encouragement, and recommendations assisted my project in many ways.

TABLE OF CONTENTS

LIST OF TABLES

LIST OF FIGURES

LIST OF EQUATIONS

LIST OF ABBREVIATIONS AND SYMBOLS

Variable / Abbreviation	Definition	Designation in other works
AL	Initial albedo	
ALBEDO	Albedo, empty slate for initial AL	α
α_{ice}	Ice albedo	AICE
AM	Absolute difference between TEMP – TM	
ASOL	Incoming shortwave radiation	E_{in}, R↓
A & B	Longwave radiation coefficients 1 & 2. Empirically determined constants, designed to replicate the greenhouse effect of clouds, water vapor, and CO_2	
β	Axial Obliquity	
C	Transport coefficient	E_{trans}, k_1, F
CALB	Cloud albedo	
CLOUD	Cloud amounts (zoned)	*n (Budyko)*
DP	Temperature at the next latitude minus the TCRIT times IN	
e	Orbital eccentricity	
Energy	Units: Joules	
IN	Weighting function π/zones of longitude	
Insolation	Units: W/m^2 "A function of the energy received by the Earth from the Sun per unit of time per unit of area" (Berger et al, 2010) Energy per unit time = Joules/Second = Watts, and per unit area makes it $Watts/m^2$	Sa, Solar radiation
LATICE	Latitude of ice-line	Φ_{ice}

LATZ	Latitudinal Zones	y, ζ
NL	Number of latitude	
η	Albedo Function (Walsh)	
OL	Outgoing longwave radiation (OLR)	Walsh: E_{out}, Budyko: I (Kcal/(cm^2month)) Henderson-Sellers: R↑ OLR
σ6	Sixth-degree approximation by Legendre series	
S	Mean annual radiation	
SOLCON	Solar constant (=S_X*1370/4)	Q
S_X	Fraction of the solar constant used	S/S_o
$\overline{T}$	Mean annual global surface temperature	TM
τ_a	Transmissivity of the atmosphere (Henderson-Sellers)	
TCRIT	Critical temperature where ice starts to form	T_c
TEMP	Surface temperature at a specific latitude	
T_e	Effective Temperature	
ToA	Top of Atmosphere	
TSI	Total Solar Irradiance	
TSTART	Initial temperature values for the model	
v	Wind speed (Sellers)	
Watts	Joules/Second	
0D	Zero-dimensional model	
1D	One-dimensional model	
2D	Two-dimensional model	

ABSTRACT

ENERGY BALANCE MODELS WITH REALISTIC ALBEDO, MONTHLY INSOLATION, MILANKOVITCH CYCLES, AND SIMPLIFIED EARTH-LIKE PLANETARY MODELING

Christian Johann Taubenberger, M.S.

George Mason University, 2020

Thesis Director: Dr. Linda A. Hinnov

Energy balance modeling with simple flows is largely overlooked today in favor of the realism of sophisticated Earth system models. However, much can be learned from simple energy balance models (EBM's), especially for paleoclimate modeling and for exoplanets. In fact, with some modest adjustments, EBM's allow for a comparable output model to some general circulation models. Here, the classic Budyko-Sellers one-dimensional energy balance model is revitalized in MATLAB to include zero-dimensional (0D), multiple one-dimensional (1D), and multiple two-dimensional (2D) versions with realistic monthly albedo, monthly insolation, and an algorithm for mean annual insolation for any star-orbiting planet with non-zero obliquity and orbital eccentricity, and a rotation rate that is significantly faster than that of its orbit. The revitalized EBMs are applied to characterize the energy balance of Earth, while also showcasing their applicability for a range of realistic obliquities and orbital eccentricities. The significance of specific variables was tested, such as changes to insolation, latitudinal heat transport, outgoing longwave radiation, initial surface and cloud albedos, initial temperatures, and astronomical parameters. Model results were found to rely most

heavily on initial albedo of Earth's surface and clouds, as well as orbitally forced monthly insolation changes. The goal is to accurately model the energy balance of any planet with simplistic, limited data. In this study, the groundwork is laid for more specific questions to be answered with this catalog of models.

CHAPTER 1: INTRODUCTION

This study focuses on modernizing the computation of a basic energy balance model (EBM) for the Earth, and developing enhancements for applications to planets other than Earth, including exoplanets. After their initial conception, EBM's with orbital and insolation forcing have been chronically underutilized, as general circulation models overtook the defining role of planetary modeling, with their capacity for finer tuning and detailed scenarios. In this thesis, energy balance modeling is revitalized in recognition of the merits of less computationally intensive, simplistic modeling, especially for use with limited parameter inputs for modeling systems outside of Earth.

Limiting variables helps determine which parameters are needed to simulate planets with many unknowns (North, 1975). This thesis discusses the history of energy balance modeling, its uses for modeling Earth compared to more advanced models, and potential uses for planetary modeling of non-Earth climates using Mars, and beginning the foundations for using Pluto, as prototypes for exoplanetary modeling.

Questions and problems that can be pursued with the EBM tool developed in this thesis include:

- How does the EBM respond to changes in incoming shortwave (solar) radiation? This is a fundamental question that originally motivated the development of the EBM.
- How does the EBM respond to surface (latitudinal) heat transport? This can provide insights into feedbacks from different planetary modes of circulation.
- How does the EBM respond to changes in outgoing longwave infrared radiation? This can provide insights into feedbacks from greenhouse gas concentrations.
- How does the EBM simulate monthly and seasonal changes?
- How does initial input albedo effect the EBM?
- How does the EBM respond to different insolation forcing due to variable astronomical parameters (Milankovitch cycles)? The application of Milankovitch-forced insolation averaged per month over the year, for three time slices, the present day (0 ka), the Last Glacial Maximum (24 ka), and the Eemian Interglacial (128 Ka) provides new insights into Earth's basic surface climate responses to Milankovitch cycles.
- Determine how planetary obliquity and orbital eccentricity are affected with the application of sixth degree Legendre expansions for the zonal (latitudinal) distribution of mean annual insolation.

The classic Budyko-Sellers EBM by McGuffie and Henderson-Sellers (2005) is converted from BASIC programming language into MATLAB, and enhanced with the inclusion of Milankovitch forcing, realistic Clouds and the Earth's Radiant Energy System (CERES) Energy Balanced and Filled (EBAF) surface albedo data product as input albedo, monthly insolation, and Legendre series expansion of the mean annual insolation, together with other changes described above. Simplistic approaches are created for modeling exoplanet climates. A catalog is designed with three collections of scripts: 0D, 1D, and quasi-2D EBMs, which will be used according to available input information and question(s) to be addressed.

Initial parameters for input surface albedo and temperature were tested for their influence on outputs, input surface albedo was determined to significantly impact model outputs, which, along with the albedo of ice (α_{ice}) and the albedo of clouds along the cloud fraction profile provided insight into how significant the inclusion of realistic albedo is to model accuracy. Initial temperatures were found to have a far less significant impact on model output values, and did not drastically change outputs from expected values until an extreme departure from global averages were used. This provides critical insight into how, while realistic albedo is required for true simulation, highly accurate starting temperatures are not. The critical temperature (T_c), where ice starts to form on both land and ocean surface is shown to have more impactful changes with variations to the T_c of the ocean, rather than land.

Changes to the heat transport coefficient, C, influences global stability through the increase or decrease of heat transport from one zone to another. Changes to insolation through Milankovitch cycles produces a discernable impact on the ice-albedo feedback; and the influence of the history of the climate system is observed in tests of a climate hysteresis effect. The results of these tests allowed for an initial look at how the different versions of the model could be used for systems other than Earth, such as Mars, and the preliminary collection of data needed for Pluto was also started.

CHAPTER 2: LITERATURE REVIEW

The energy balance in the Earth climate system can be described by the equation (Budyko, 1969):

Equation 1: $\boldsymbol{E_{In} = E_{Out} + E_{Tran}}$

which relates incoming shortwave radiation from the Sun E_{In} to outgoing longwave radiation (OLR) from the Earth E_{Out} plus the energy flux transferred out of a latitude zone to its colder adjacent latitude zone E_{Tran}.

E_{in} is the quantity, in W/m^2, of solar radiation as it reaches Earth's atmosphere. This quantity is often referred to as insolation (see Glossary). The most recent measured value for Earth is 1361 W/m^2 (Kopp and Lean, 2011).

E_{Out} is modeled empirically as follows:

Equation 2: $\boldsymbol{E_{Out}}$ **= A + BT**

where parameters A (204 W/m^2) and B (2.17 Wm^{-2}°C^{-1}) are empirically determined constants that account for the effects of greenhouse gases and in some cases longwave cloud forcings, while T refers to the mean annual surface temperature of a specific latitude in °C (Graves et al., 1993; McGuffie and Henderson-Sellers, 1988, 1997, 2005, 2014). A and B are used to characterize the relationship between OLR and surface temperature (**Figure 1**). The parameters have been computed from real atmospheric

conditions or estimated from satellite data (**Figure 1**; Graves et al., 1993; North and Kim, 2017). Parameter B is inversely proportional to temperature anomalies by radiative cooling, in other words, a larger B value will result in the faster radiative dampening of temperature anomalies (Graves et al., 1993). B varies over latitude and longitude (in the tropics), and is higher at higher latitudes (Graves et al., 1993). A and B can also change due to the chemical composition of the atmosphere (Warren and Schneider, 1979). Budyko (1969) used the values of A = 202 W/m^2 and B = 1.45W/m^2°C, and Sellers (1969) equates A = 211 W/m^2 and B = 1.68W/m^2°C. In **Figure 1**, 90°N can be roughly correlated to the far left of the temperature axis, and 30°N, the right, where more OLR can be attributed to warmer regions.

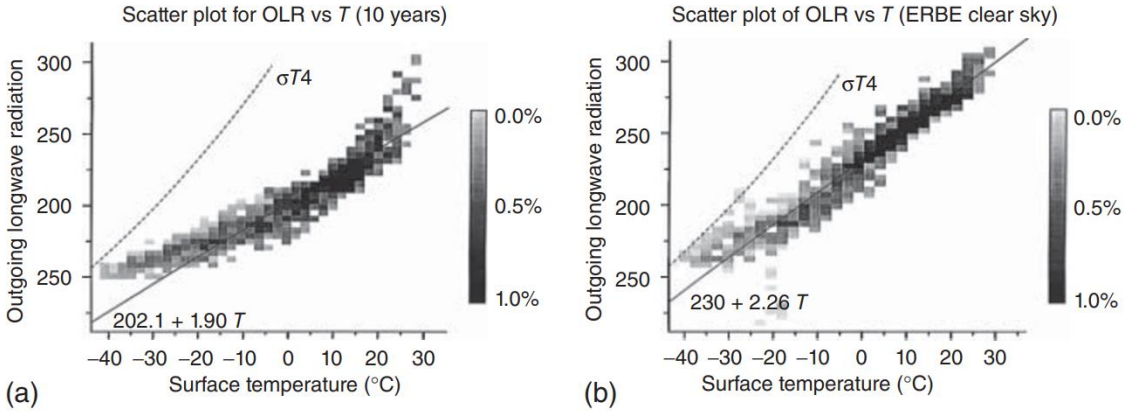

Figure 1: Outgoing longwave radiation (OLR) as a function of temperature T, different values taken between 30°N and 90°N, and the 202.1+1.90T fit (solid line). a. is the derived from data without accounting for the presence or absence of clouds. b. represents the clear sky values where cloudy pixels have been removed pre-averaging. Darker values indicate higher occurrence frequency. Dashed line represents the blackbody curve (Graves et al., 1993).

E_{Tran} accounts for zonal heat transport or "latitudinal heat flux" which is the loss of energy by a zone of latitude to its colder neighbors:

Equation 3: $\boldsymbol{E_{Tran}}$**= C(T-**$\boldsymbol{\bar{T}}$**)**

where C represents the heat transport coefficient and $\bar{T}$ is the mean annual global surface temperature (McGuffie and Henderson-Sellers, 2005; Walsh and Rackauckas, 2015). C has had a variety of assumed values, originally 3.79 Wm^{-2}/°C (Budyko, 1969), this was argued to be lower (3.74 Wm^{-2}/°C) in a later study based on Ellis and Vonder Haar (1976) observations simulate a smoother ice-line which better agreed with the most up to date global average albedo at the time, 0.303 (Warren and Schneider, 1979). C (i.e. k_1) was set to 3.81 Wm^{-2}/°C in McGuffie and Henderson-Seller's model (1986).

In order to determine how dependent T is on solar radiation with other factors influencing outgoing longwave radiation the following equations were derived (Eqs. 1 and 2 in Budyko, 1969):

Equation 4: $\boldsymbol{I = a + BT - (a_1 + B_1 T)n}$

Equation 5: $\boldsymbol{I = Q(1 - \alpha) - A}$

I is the outgoing longwave radiation (OLR) per unit area (kcal/cm²/month), and *a*, *B*, a_1, and B_1, are dimensional coefficients equal to 14.0, 0.14, 3.0, and 0.10, respectively, α is albedo, and *A* is the change in heat as a result of circulation, including heat redistribution, and water phase transformation. *A* should not be confused with (unitalicized) A and B in **Equation 2**. Linear functions of the surface temperature for non-cloud covered sky are represented by $\boldsymbol{a + BT}$, and functions for cloud covered sky are represented by $\boldsymbol{(a_1 + B_1 T)n}$. Finally, *n* is the fraction of cloudiness for Earth, equal to 0.5 (Budyko,

1969). *Q*, or "solar radiation coming to the outer boundary of the atmosphere" (Budyko, 1969) averages 340.25 W/m^2 per day for solar radiation arriving at the "top of the atmosphere" (ToA) for Earth, which depends on the eccentricity of Earth's orbit (Budyko, 1969; McGehee and Lehman, 2012). *Q* is the solar constant, 1361 W/m^2 (Kopp and Lean, 2011), divided by 4 to account for incident area of a disk of radius r divided by the area of a sphere $4\pi r^2$, where *r* is the radius of the Earth. The variable α corresponds to the planetary albedo, 0.33, and *A* (**Equation 5**) is the gain or loss in heat as a result of atmospheric and hydrospheric circulation, equal to 0 for Earth as a whole (Budyko, 1969).

In their one-dimensional EBMs, Budyko (1969) and Sellers (1969) were interested in the latitudinal distribution of energy at the Earth's surface (**Figures 2** and **3).** Budyko's (1969) figure shows the relationship of temperature, both observed and the average latitudinal distribution, to degrees of latitude for the Northern Hemisphere. Sellers' (1969) figure shows the same relationship of observed temperature to latitude, with the additions of wind speed (v) and planetary albedo (α_s). Sellers models these values across both hemispheres, and the effect of more ice and higher albedo in the Southern Hemisphere compared to the Northern Hemisphere is shown by the cooler observed temperatures (Sellers, 1969). Budyko's latitudinal ice line equilibrium position (η) is shown according to the albedo function, α (*y*,η), as it changes with solar constant $\Delta Q/Q$, where *y* is there sine of latitude (θ). It is assumed that there is ice above a specific latitude $y = \eta$, and no ice below $y = \eta$. Setting T*(η) equal to T_c produces the relationship between equilibrium ice-line position and *Q* (**Figure 4)** (Walsh and Rackaukas, 2015).

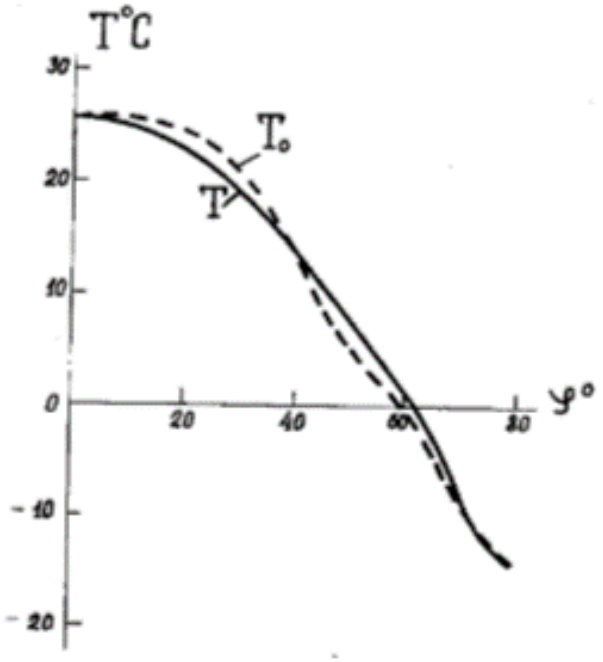

Figure 2: Budyko (1969): Degrees of Northern latitude (ζ°), T (observed temperature) and T_o (average latitudinal distribution of temperature) in °C

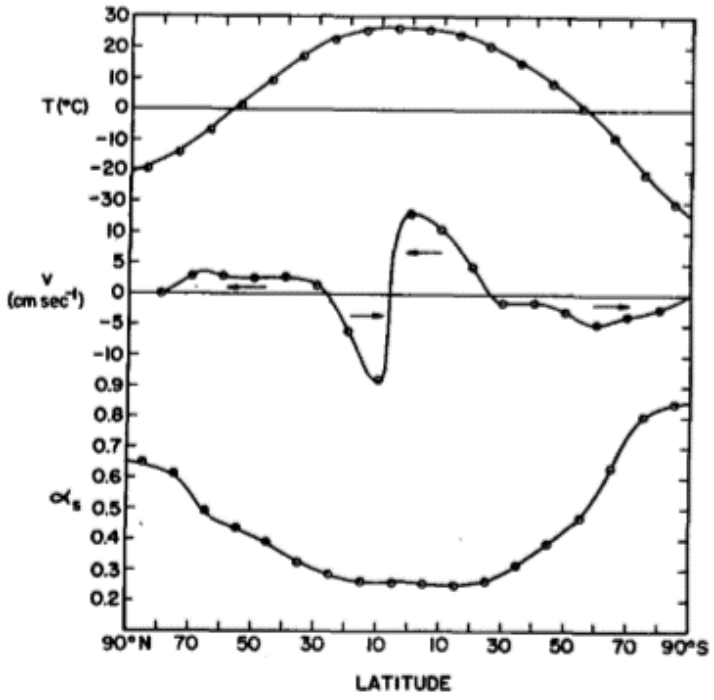

Figure 3: Sellers (1969): Mean annual sea level temperature (T°C), wind speed (v), and planetary albedo (α_s)

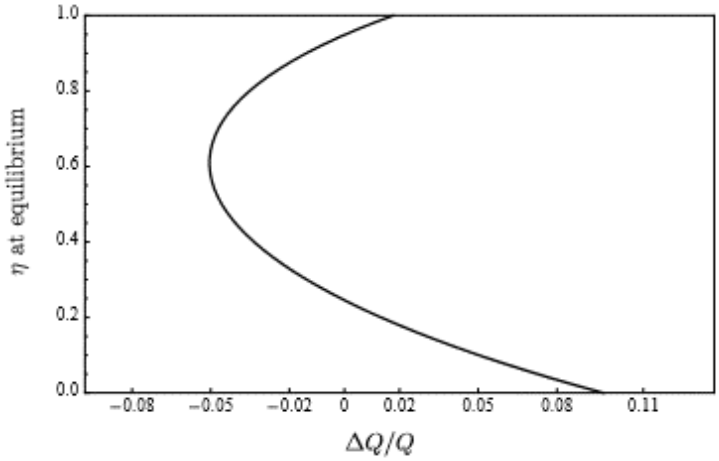

Figure 4: Walsh & Rackaukas (2015): Ice line equilibrium position (sine of latitude) with respect to Budyko modeling and albedo function (α (*y*,η)) as a function of changes in Q as defined by the solar constant.

T_c is the critical temperature at which ice covers the Earth's surface, when α increases from 0.32, the albedo for land, to 0.62, the albedo for ice. T_c differs according to land surface (T_c = 0°C) or ocean surface (T_c = -1.8°C), the latter due to salinity. Critical temperature for the ocean surface was set equal to -13°C in McGuffie and Henderson-Sellers (2005) in a crude attempt to indirectly account for heat capacity and the requirement of the top 100-150 meters of water to be cooled to -1.8°C temperature for ice to start forming at the surface (National Snow and Ice Data Center, 2020). In **Figure 4**, T_c = -10°C, representing the average critical temperature for freezing on Earth (McGuffie and Henderson-Sellers, 2005; Walsh and Rackaukas, 2015). The ice line is defined as follows: for T>-10°C, there is no ice cover, and for T<-10°C, there is ice cover (Budyko, 1969; North, 1975).

2.1 The Evolution of Energy Balance Models

Gerald R. North has been instrumental in popularizing the use of energy balance models (EBMs) since the 1970's. His work has provided a practical framework for incorporating new empirically collected data into modeling efforts (North, 1975). Model parameterization sensitivities were solved for seasonal models in order to study the effects of orbital and stochastic forcing elements on temperature (North et al., 1981). North has also discussed the limitations of energy balance models: simple models best model space and time scales of climate of the near-surface environment; going beyond the surface becomes too complex due to temperature sensitivity to atmospheric circulation, and for the same reason, most EBM's do not account for precipitation (North and Kim, 2017; although see Siler et al., 2018). EBM's are well suited for rapid modeling of paleoclimates, as they are computationally economical for successive runs with differing parameters, and work well when averaged over longer time scales, as the potential for errors is reduced.

North's comments also touch on another motivation for this thesis, in that an exoplanet's habitable zone, as well as its atmospheric, chemical, oceanic dynamical, and orbital parameters may fit well within the capabilities of EBMs (North and Kim, 2017). North (1975) emphasizes that models need to provide reliable results; once that is established, the models can provide useful means for deciding which parameters are needed to simulate planets with many unknowns. EBM's prove potent here by already limiting the complexity of variable interactions.

By classical definitions, zero-dimensional (0D) EBMs, focused on changes affecting radiative transfer properties of the atmosphere, refer to the entire planet as a single body which has an effective temperature (T_e). One-dimensional EBMs divide the planet into latitudinal zones, with albedo and surface temperature modeled for each zone. One-dimensional EBMs provide for meridional (poleward) heat transfer and an adjustable ice line for the planet. Ice-albedo feedback is a critical feature, accounting for significant differences between the albedo for ice and ice-free planetary surfaces (Budyko, 1969; North, 1975).

The sequence of approximations in which each successive calculation introduces smaller space and time scales proposed by North (1981) removed the issues of discontinuity of meridional temperature distribution at the ice line in Budyko's (1969) model due to the inherent discontinuity of the albedo function (η). Sellers similarly assumed an albedo function across the ice line using a continuous transition (Walsh and Rackaukas, 2015).

The heat transport coefficient C (**Equation 3**), when determined from present-day temperature distributions, accurately predicts the total annual heat transport across all latitude zones when compared to observations of transport. However, in tropical zones, Budyko parameterization of heat transport struggles to accurately model seasonal deviations from the mean annual value compared to observed Ellis and Vonder Haar net heat transports (Warren and Schneider, 1979).

2.2 Mean Annual Insolation by Latitude

Latitudinally zoned mean annual insolation can be approximated using sixth order Legendre series expansion for any star-orbiting planet with non-zero obliquity and orbital eccentricity (Nadeau and McGehee, 2017). Without using Legendre series expansion, one could alternatively calculate orbital parameters, such as distance to the Sun, or solar declination angles over the course of a year, given that models include latitude-longitude grids. However, insolation and latitude relationships may become complicated over long time-scales (Nadeau and McGehee, 2017). Nadeau and McGehee (2017) define mean annual insolation ($\bar{I}$) as a function of sine of latitude (y) using the orbital parameters of obliquity (β) and eccentricity (e) with a Legendre series expansion:

Equation 6: $\boldsymbol{\sigma_6(y,\beta) = 1 - \frac{5}{8}p_2(cos\beta)p_2(y) - \left(\frac{9}{64}\right)p_4(cos\beta)p_4(y) - \frac{65}{1024}p_6(cos\beta)p_6(y)}$

$p_k's$ refer to the Legendre polynomials of order k:

$p_2(y) = (3y^2 - 1)/2$

$p_4(y) = (35y^4 - 30y^2 + 3)/8$

$p_6(y) = (231y^6 - 315y^4 + 105y^2 - 5)/16$

Insolation is integrated over one annual orbit, then across all longitudes to find the average annual insolation for any latitude on Earth's surface. The algorithm is general enough to work for any star-orbiting planet with enough given physical knowns, as long as its rotation rate is significantly shorter than its orbital period (Nadeau and McGehee, 2017). Sixth-degree approximations (σ_6) most accurately represent more complicated insolation distributions, such as for Pluto (**Figure 5**). σ_6 works well for representing

insolation that were covered by previous degrees of approximation as well, and as such is used for all insolation as function of latitude.

Figure 5 displays the insolation distributions for both Earth and Pluto, with increase in approximation from 2^{nd} degree, to 4^{th} degree, to 6^{th} degree, the fit improves. More complex orbits, as seen in Pluto, require higher degrees of approximation. Planets with simple orbits, such as Earth, can be accurately represented by just a 2^{nd} degree approximation (Eq 2. in North, 1975).

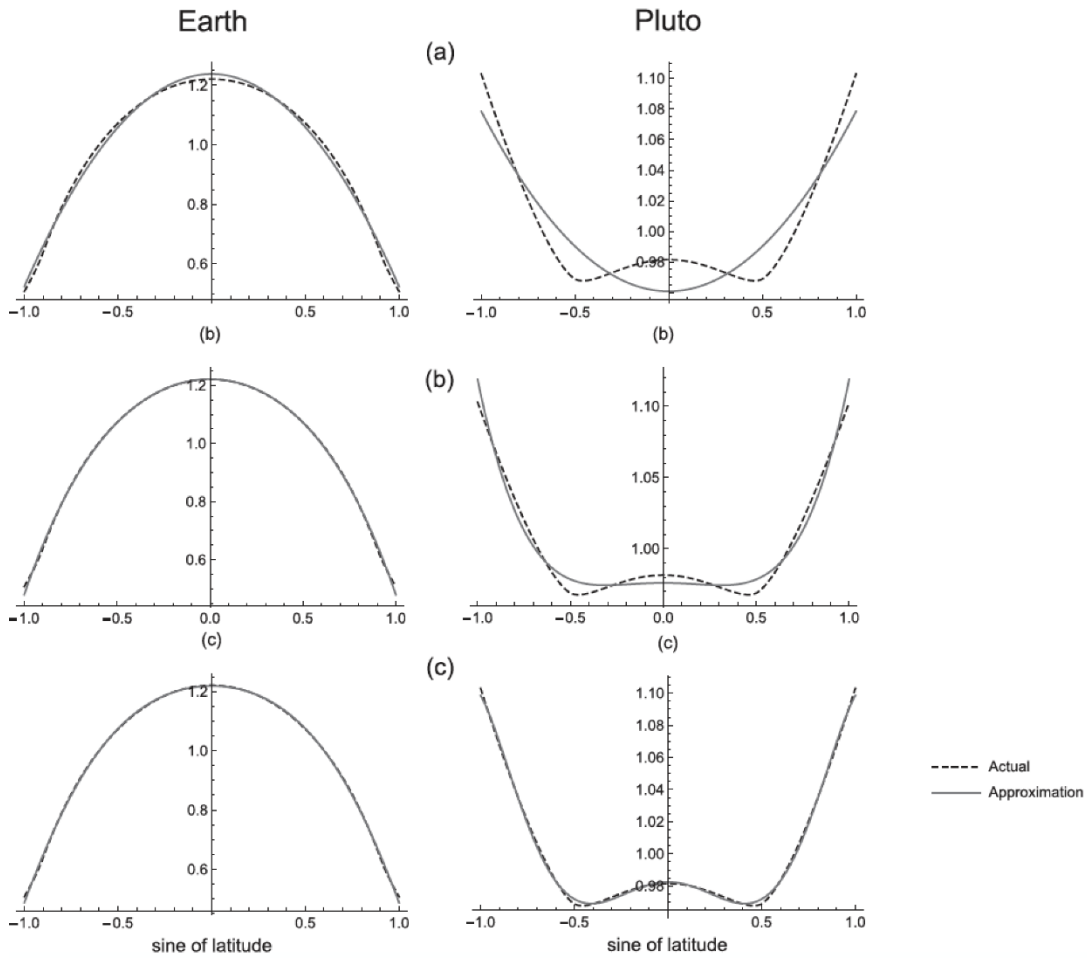

Figure 5: Insolation distributions for Earth and Pluto based on 2nd (a), 4th (b), and 6th (c) order Legendre polynomial approximations (Fig. 1 of Nadeau and McGehee, 2017).

2.3 Total Solar Irradiance

The accepted value of the total solar irradiance (TSI), also known as the solar constant at the "top of the atmosphere" (ToA), has been a long-standing problem. Budyko (1969) referred to total solar irradiance as 1.92 cal/(cm^2minute), i.e., 1339 W/m^2. In the late 1990's and early 2000's, with the advent of satellites, TSI was estimated as 1365.4 ± 1.3 W/m^2 (Passos et al., 2007; Lean, 2009). Climate models and empirical calculations for

energy balance used numbers close to this value for more than a decade; McGuffie and Henderson-Sellers (2005) assumed 1370 W/m^2. Eventually it was discovered that scattered light, undetected by older solar radiometers, produced erroneously high irradiance measurements; NASA's Total Irradiance Monitor on board the Solar Radiation and Climate Experiment determined a more accurate value of 1360.8 ± 0.5 W/m^2 (Kopp and Lean, 2011). This value is the currently accepted TSI for the Earth, and is adopted in this study.

2.4 Astronomically forced Insolation: Milankovitch cycles

Variations in Earth's orbital characteristics can have large-scale impacts on the climate system. Astronomical parameters, such as precession, obliquity, and eccentricity, fluctuate cyclically due to gravitational interactions with other bodies in the Solar System (Milankovitch, 1941; Berger, 1978; Berger et al., 2010). Changes in the parameters alters the Earth's position relative to the Sun, inducing variations in the solar irradiance that reaches Earth. Milankovitch demonstrated that these fluctuations have specific cycles and impact the Earth to different degrees depending on geographic location and time of year.

The retrograde precession of Earth's rotational axis in relation to the fixed stars has a periodicity of approximately 25,771.5 years (Eq. 39 in Capitaine et al., 2003). This motion, in combination with the slower prograde apsidal precession of the Earth's orbit with a periodicity of approximately 113,187.8 years (Table 4.1 in Fitzpatrick, 2012), shortens the effective precession of Earth's longitude of perihelion to a periodicity of approximately 21,000 years. Milankovitch originally hypothesized that Earth obliquity, or axial tilt, which varies between 22.1° and 24.5° from the Earth's orbital plane, at a

41,000- year periodicity, was the largest contributor to climate variations. This is due to the significant effect that obliquity contributes toward the amount of solar radiation received in the polar regions. Higher obliquity results in more solar radiation intercepted at the poles during summer months. Currently, Earth's obliquity equals 23.44° and is decreasing (NASA, 2016). **Figure 6** indicates that the precession, modulated by the orbital eccentricity, dominates insolation near the equator, and obliquity assumes a greater role for insolation at middle and higher latitudes (Berger, 1978).

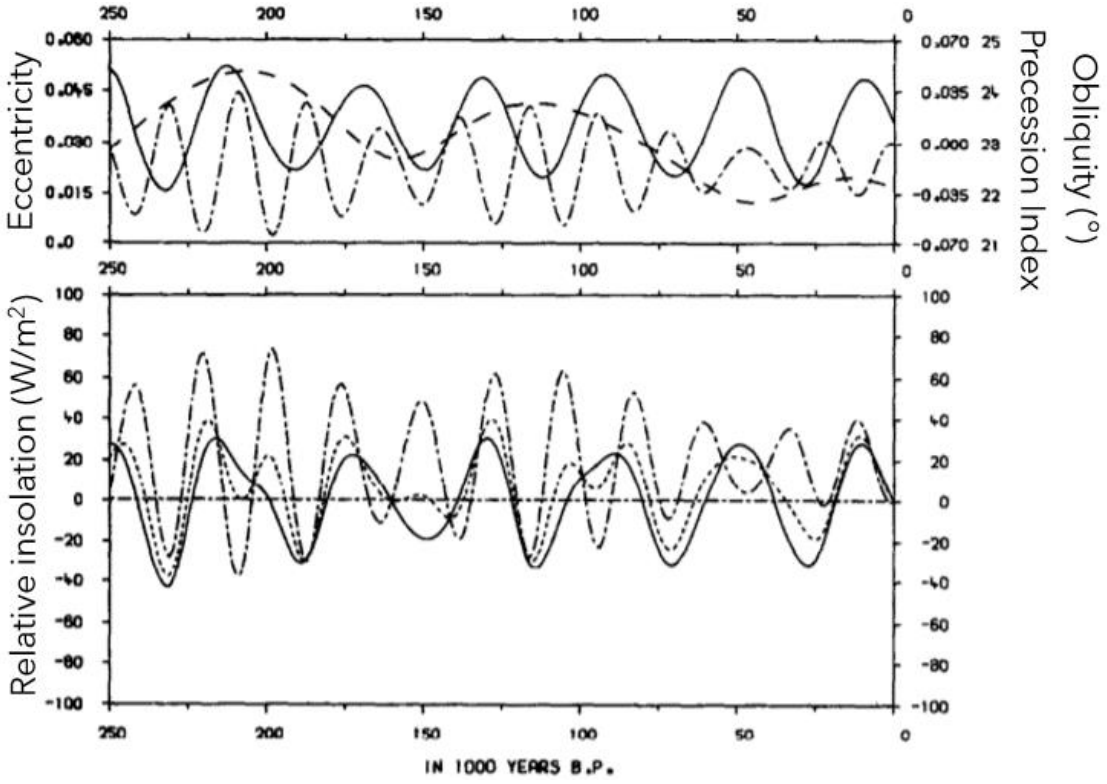

Figure 6: Long term variations of Earth's orbital parameters. Top: orbital eccentricity (dashed line), precession index (dash-dotted line), obliquity (solid line). Bottom: Caloric summer Northern Hemisphere solar radiation. 80°N (solid), 65°N (dashed), 10°N (dash- dotted). (From Berger, 1978.)

While climate cycles with periodicities matching those of the astronomical parameters have been found throughout the geological record, the relative influence of the orbital eccentricity, obliquity and precession index on climate change as a general rule does not match the influence predicted by the Milankovitch cycles. For example, over the last 458,000 years, 100,000-year orbital eccentricity accounted for 50% of climatic variance related to the glaciations, obliquity accounted for 25%, and the precession index only 10% (Hays et al., 1976). Further back in time however, i.e., from 2.6 Ma to 1.6 Ma, obliquity's influence on glaciations surpassed that of orbital eccentricity. There have been many studies devoted to investigating this change (e.g., Huybers, 2006; Raymo et al., 2006; Raymo and Huybers, 2008); one explanation is that it is due to the complexity of the ice-albedo feedback (McGehee and Lehman, 2012). Periods of orbital eccentricity overwhelmingly associate with periods of glaciation, rather than the phasing of obliquity or precession (Hays et al., 1976).

Earth's orbital eccentricity, or the degree to which Earth's orbit stretches from circularity to an ellipse due to the gravitational influence of other planets, ranges from near zero at its minimum, to near 0.07 at its maximum over an approximately 100,000-year cycle, together with an even higher-magnitude 405,000-year cycle (Laskar et al., 2004a). Earth's current orbital eccentricity is reported as 0.01671022 (NASA, 2016) (and estimated as 0.016702361 by Laskar et al., 2004a).

The evolution of Earth's precession index (top), obliquity (middle), and orbital eccentricity (bottom) is shown in **Figure 18** over the period of -150kyr to present, showing clear cycles. This astronomical solution allows for the modeling of Earth's

climate over long timescales, to account for changes to astronomical parameters, and allow for the impact of solar irradiance and ice-albedo feedback to be investigated.

2.5 BASIC Energy Balance Modeling

The Budyko (1969) and Sellers (1969) models were formulated as a BASIC computer model by Henderson-Sellers and McGuffie (1986), with the simple goal to model input and output radiation fluxes, equator-to-pole transport of energy, and ice-albedo feedback. This showcased the balance of the planetary radiation budget and the approximate global climate in simplistic terms. Future editions would provide for increasing model capabilities, while retaining the original goal of simplicity. In 2005, *A Climate Modeling Primer*, *Third Edition*, evolved the model from equator-to-pole to a full pole-to-pole model. The *Fourth Edition*, released in 2014, returned to an equator-to-pole format, providing an Excel module. The primary source of the models developed in this study originated from the *Third Edition* version.

In zero-dimensional models, incoming shortwave radiation and outgoing longwave radiation are balanced through the surface temperature variable, T **(Figure 7)**. In other words, T is the critical dependent variable used to solve the climate equations (McGuffie and Henderson-Sellers, 2014). The change in temperature over time is based upon the differing rate of incoming and outgoing radiation over the area of the planet**.** In the case of Earth, this is chiefly resolved by the oceans (McGuffie and Henderson-Sellers (2005).

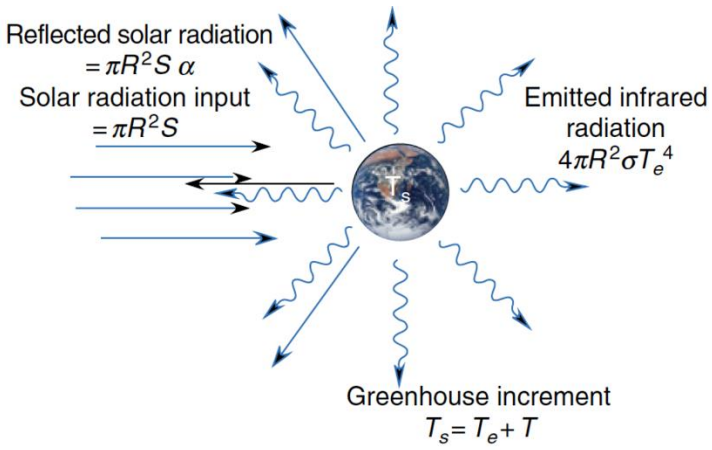

Figure 7: Energy fluxes in a zero-dimensional EBM, from Fig. 3.1 in McGuffie and Henderson-Sellers (2014).

Incoming shortwave radiation is a function of solar flux at the TOA (S) and the planetary albedo (α):

Equation 7: $\boldsymbol{E_{in} = \frac{(1-a)S}{4}}$

McGuffie and Henderson-Sellers used S = 1370 Wm^{-2}, and α = 0.3, as close approximations of the exact Earth values. Outgoing longwave radiation can be estimated using the Stefan equation and T, accounting for the transmissivity of the atmosphere $\varepsilon\tau_a$:

Equation 8: $\boldsymbol{E_{out} = \varepsilon\sigma T^4 \tau_a}$

For a zero-dimensional model, this allows for the balance of incoming and outgoing radiation for a single point by combining the two, where $\varepsilon\tau_a$ = 0.62, the albedo of ice, and σ the Stefan-Boltzmann constant, $5.67 \times 10^{-8} Wm^{-2}K^{-4}$. Applying these values to Equations **7** and **8**, results in a temperature of T = 287K, the globally averaged surface

temperature of Earth (McGuffie and Henderson-Sellers, 2005). **Equation 9** indicates that incoming shortwave radiation equals outgoing longwave radiation:

$$\textbf{Equation 9: } \frac{(1-\alpha)S}{4} = \varepsilon \tau_a \sigma T^4$$

For one-dimensional modeling, where each zone of latitude (*i*) is individually considered, **Equation 10** was formulated.

$$\textbf{Equation 10: } S_i\left(1 - \alpha(T_i)\right) = E_{out}(T_i) + F(T_i)$$

$F(T_i)$, from in **Equation 3**, refers to the loss of energy by a zone of latitude to colder neighboring zones, and serves as the origin term for C, the transport coefficient.

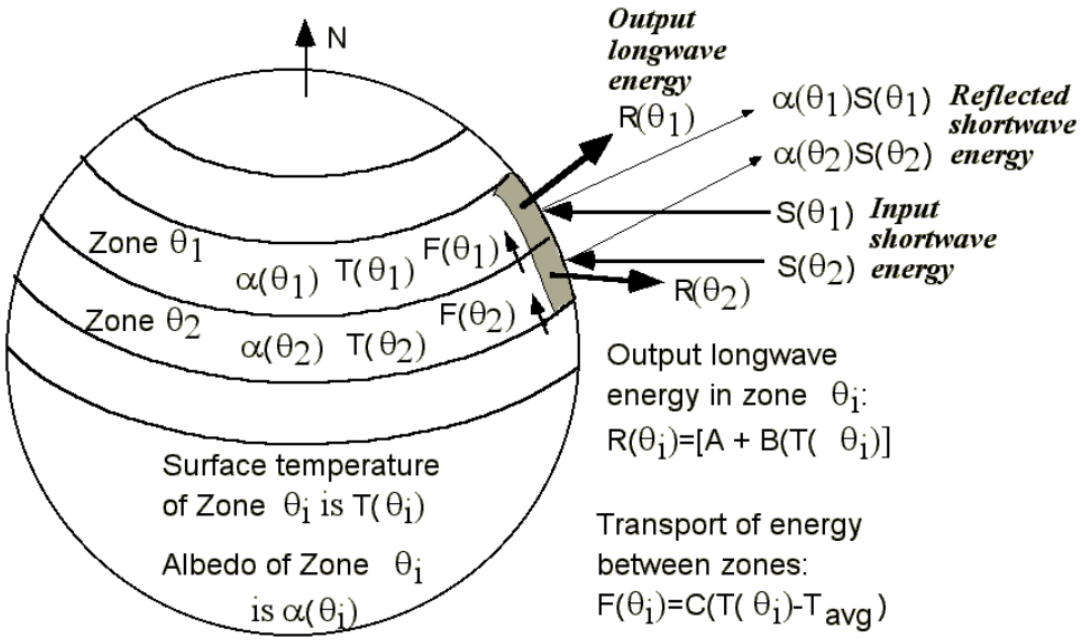

Figure 8: Budyko-Sellers type model for zonal transport of radiation based on Shodor Foundation, 1998.

Figure 8 illustrates the 1D energy balance model, showing incoming shortwave radiation, outgoing longwave radiation, and the *F* transport of energy between zones parameter. This energy balance system was parameterized for the model using Budyko's and Sellers' concepts of shortwave in is equal to longwave out plus transport out, as described in **Equation 1** and input into **Equation 11**.

Equation 11: $\boldsymbol{S(\theta)\{1-\alpha(\theta)\} = C\{T(\theta)-\overline{T}\} + \{A + BT(\theta)\}}$

Many of these terms are most likely familiar at this point, having been described by Budyko-Sellers inspired variables. C is the transport coefficient. A and B being the satellite data constants representing the effects greenhouse gases described in **Equation 2**, and θ is latitude (McGuffie and Henderson-Sellers, 2005).

Equation 12: $\boldsymbol{T(\theta) = \{S(\theta)[1-\alpha(\theta)] - A + C\overline{T}\} / (C + B)}$

The model isolates $T(\theta)$ in order to solve for temperature at each latitude zone, and depends on just the temperature at which ice covers the surface (T_c), the albedo of ice (α_{ice}), the albedo of the surface (α), cloud amounts, and cloud albedo (CALB). There are also initial starting constants that are not initially prompted for one to change, but that can be easily altered. These were added as input values in the online Shodor Foundation version of the original model (http://www.shodor.org/master/environmental/general/energy/energy.html) that only represented equator to pole, and kept as front-facing editable variables in all versions of this EBM. Those starting constants were: initial temperature of zones (T_{start}), longwave radiation loss constants A and B, the transport coefficient C, the solar constant (S), the

fraction of the solar constant used (S_x), and the number of iterations to run in order to reach equilibrium (McGuffie and Henderson-Sellers, 2005; Shodor Foundation, 1998).

Iterations were initially set to 50 through the variable *H.* As the model would run through its functions 50 times towards equilibrium of the poleward transfer of heat. With all of the initial parameters accounted for, quick calculations before the main function loop of the script were added, such as determining Q, or "SOLCON" from the solar constant.

Equation 13: $$\boldsymbol{SOLCON = S_X * \frac{S}{4}}$$

S was originally set to 1370 Wm^{-2}. Used alongside monthly insolation, the inclusion of this function results in a better fit to observed temperatures, and allows for the fraction of the solar constant, used to adjust for historical solar radiation and model paleoclimates, to be correlated with the spread of the solar flux over the top of the atmosphere as the Earth rotates throughout the day. From there, the temperature, albedo, and radiation fluxes for each zone can be determined as outputs to the model.

Although originally it was included simply to demonstrate what fraction of the solar constant was required to obtain Snowball Earth, solar fraction is included for its demonstration of hysteresis (see Section 5.1), produced in the results of the one-dimensional EBM. It is also included for its purpose in paleoclimate modeling, where solar radiation can be scaled back to better represent the Faint Young Sun hypothesis. This idea, that the Sun's output would be a fraction of its current intensity as stellar evolution is rewound, and would be offset by other increased climate parameters such as a stronger greenhouse effect, are important to include in a model (Feulner, 2012).

The Henderson-Sellers (2005) model was set to a 10°x10° resolution, with each zone of latitude occupying 10° on Earth. Increasing this resolution was one of the primary motivations for recreating the model in MATLAB, and is discussed next.

CHAPTER 3: MATERIALS AND METHODS

Given the outdated nature and other limitations of BASIC programming, the initial phase of this project involved updating the EBM from BASIC to MATLAB. Once MATLAB successfully replicated the original BASIC outputs, additions and replacement of parameters with more accurate input data were instituted. The BASIC program did not have the capacity to model non-Earth systems, and parameters were updated to represent better realistic starting albedo, mean annual insolation, monthly insolation, etc. This was all utilized to improve upon the model during the update into MATLAB.

Extending the model from equator-to-pole heat transfer to pole-to-pole modeling allows for a better global simulation and a full one-dimensional model experience. The next objective was to allow for a more accurate representation of Earth, with a binary representation of Earth's land and oceans in a 2D map provided by the *land-or-ocean.m* script by Chavas (2020) through the variable Zres. This script takes an input matrix of points, representing latitude and longitude, and a coastal model provided by MATLAB ("coast.mat"), and returns with points assigned with 1 for land and 0 for ocean. This permits the definition of high-resolution latitudinal zones, so that albedo can be simulated more authentically. However, the significant impact of starting albedo was revealed using this method, and in order to achieve a more accurate Earth, a more advanced version of the model (TwoD_CERES) retains the binary representation only for its continent and ocean "flagging" purpose when applying critical temperatures. Instead TwoD_CERES incorporates NASA's Clouds and the Earth's Radiant Energy System (CERES) Energy

Balanced and Filled (EBAF) data product for surface albedo. Nadeau mean annual insolation is used to compute a global temperature.

In order to accommodate the varying computational needs or known input data about the planet to be modeled, zero-dimensional (0D), one-dimensional (1D), and quasi-two-dimensional (q2D) versions of the EBM have been separately created.

The 0D version treats the entire globe as a single body. This is useful as a simplistic general model for planets with limited known data for the required input values. It also allows for quick comparisons among planets.

The 1D version allows for more specific control over planetary surfaces utilizing an input vector map from pole to pole over one line of longitude. It allows one to create their own landscape or to customize it for a given planet, and it incorporates latitudinal transport and approximations of ice-lines using albedo.

The q2D version outputs the globe as a 2D map, however, it is not a true 2D model, such as a GCM, with no heat transport defined from East to West, i.e., it depicts a non-rotating Earth.

The nominal model, working with a 10^{o}x10^{o} resolution for latitude and longitude resulted in a single output for each of these 10^{o}x10^{o} large zones, poorly defining these zones, especially for smaller landmasses with significant coast to land ratios. Increasing the resolution to 1^{o}x1^{o} accurately defines land and ocean surfaces. Albedo input maps for Zres and CERES are shown in **Figure 9** and **Figure 10**, respectively. Temperature and albedo model outputs can be incorporated into the global map, producing visual portrayals of the q2D EBM's outputs such as those discussed in Chapter 4 and 5.

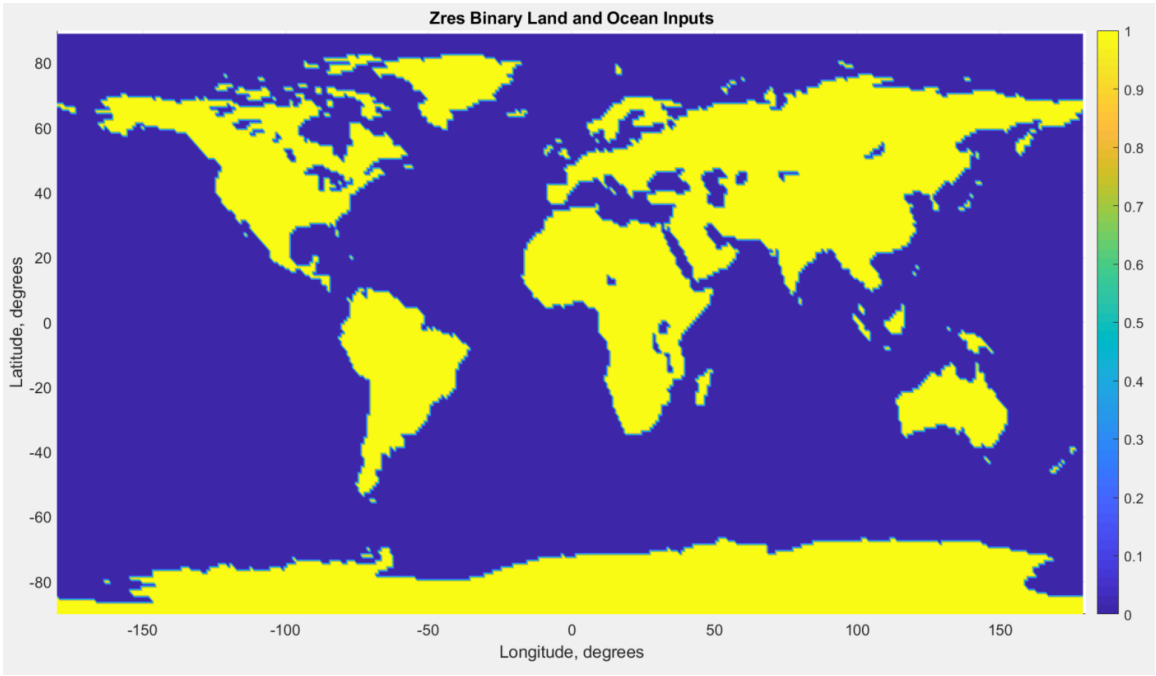

Figure 9: Input binary 1°x1° resolution Zres 'Land vs Ocean' map

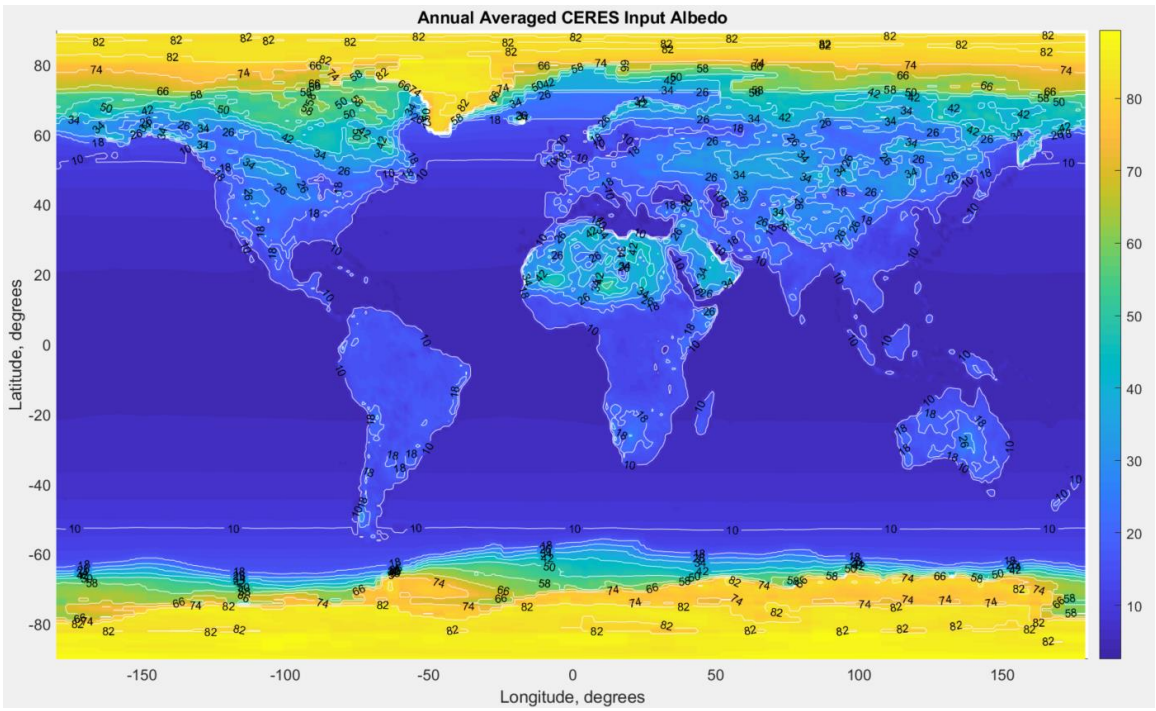

Figure 10: Input realistic 1°x1° resolution annually averaged CERES albedo map

A graphical user interface (GUI) was created using MATLAB's GUIDE system, allowing for straightforward and rapid altering of input values. Values for the solar constant, solar fraction, chosen month, time slice Laskar insolation, A, B, C, T_c of land, T_c of ocean, α_{ice}, CALB, β, e, and selection of a single longitude value vs. a global output are among those available for out-of-script editing. Other less commonly swapped parameters have also been incorporated early into the model to remain clear and accessible. Each EBM version maintains a unique GUI adapted to fit the parameters used in the version, example for TwoD_CERES in **Figure 11**.

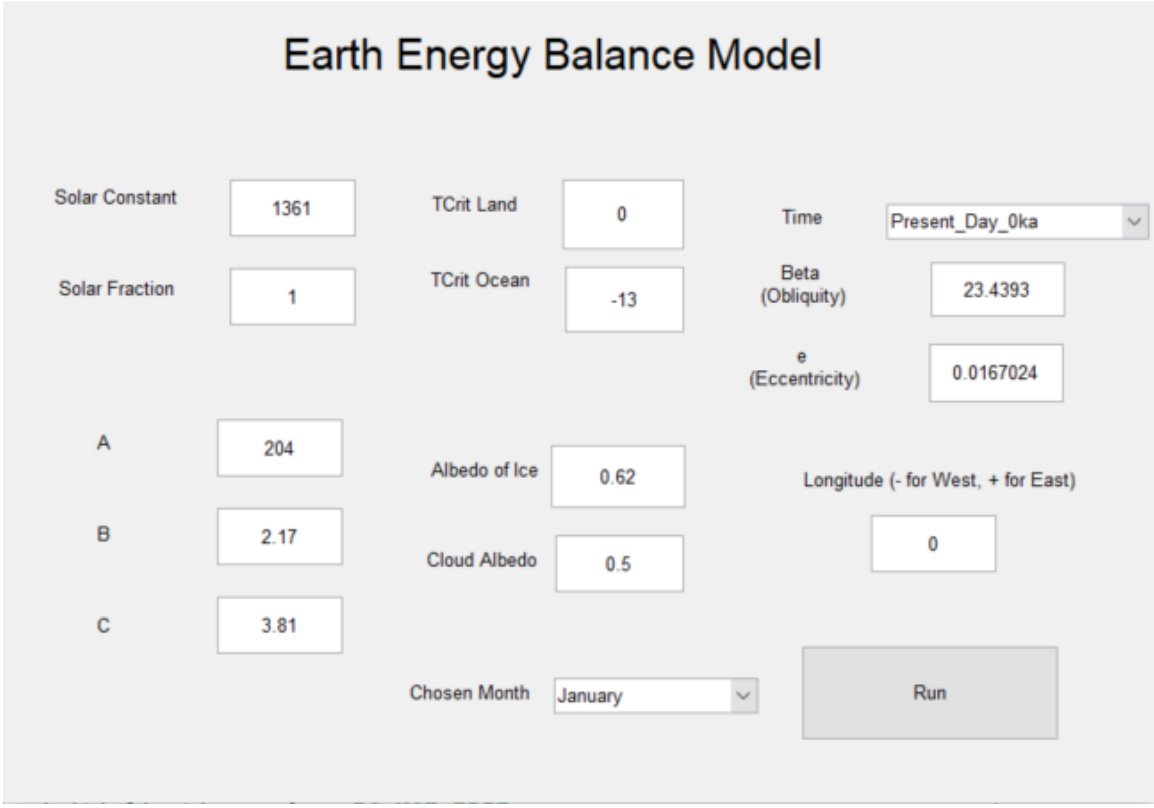

Figure 11: Sample GUI inputs with default values for CERES-Monthly Insolation driven Earth.

3.1 Model Versions

Within this thesis study, several energy balance model versions have been created to varying degrees of complexity. Each contains different model parameters that can be used based on the number of known variables one is attempting to work with, as well as the type of system desired. The models range from zero-dimensional, meaning a single entity represents the whole system; one-dimensional, representing single longitude outputs, to two-dimensional, which incorporates computationally created maps displaying outputs for all longitudes across the globe.

Figure 12 shows a flowchart of the various versions available to be used, and summarizes their parameterizations. There are two 0D, four 1D, and three 2D models. Each "step" forward in the model versions incorporates the features of the previous most advanced version, to the degree that is applicable. This means that the 1D models include every function of the most advanced 0D models, and the 2D models include all functions from 1D and 0D models. Versions that originate from previous models include everything in the previous model, except where specifically contradictory, i.e. for 2D Mars, the initial albedo comes from MGS TES surface albedo data rather than the binary land and ocean data.

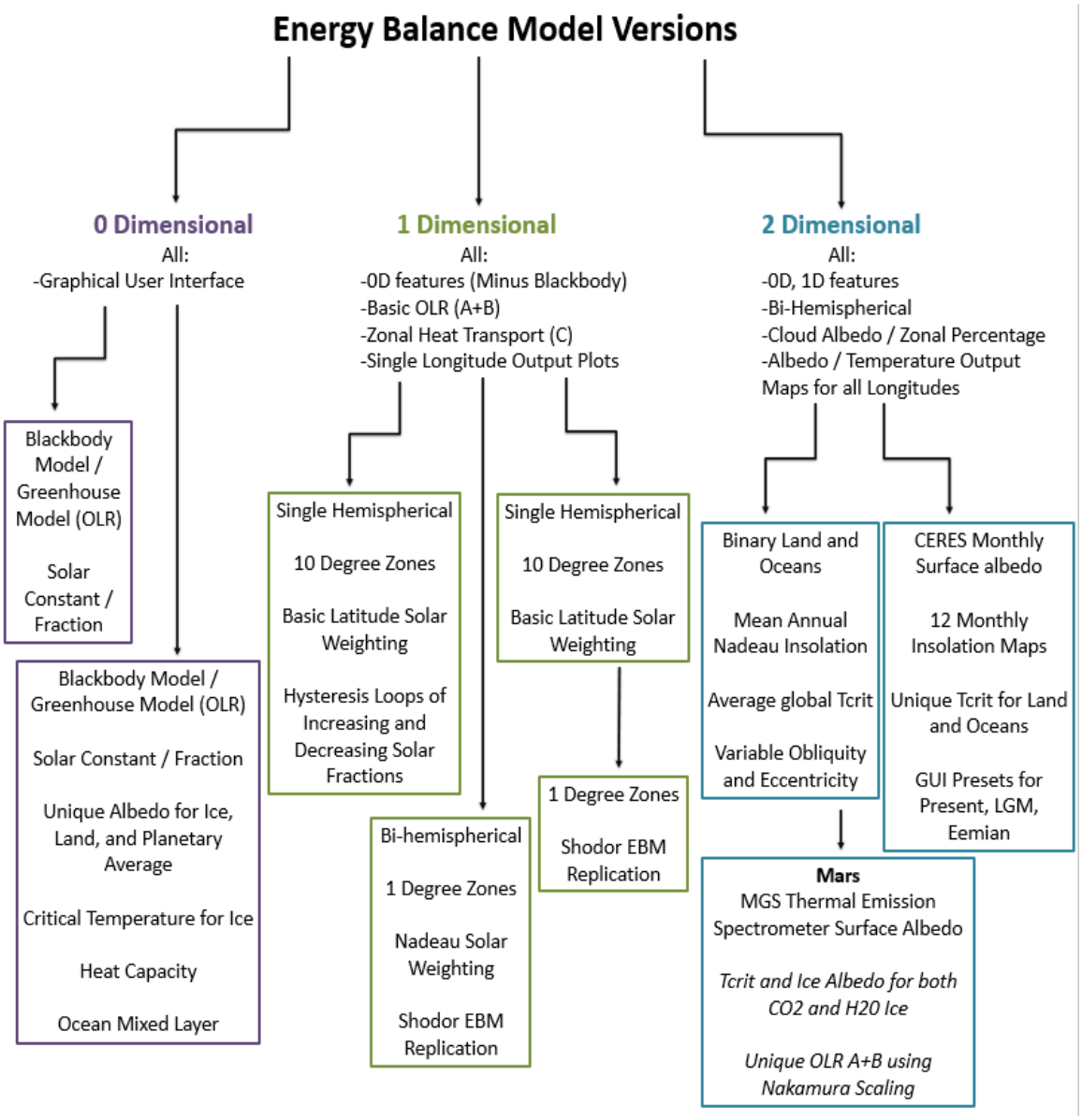

Figure 12: All EBM versions presented in this model cluster, containing brief descriptions of what they entail.

3.2 Zero-Dimensional EBMs

The zero-dimensional models differ only in their complexity of parameters, with ZeroD_EBM_V2 accommodating for the influence of α_{ice} from the planetary average α,

the heat capacity of the oceans, and mixing of the ocean layers. Critical temperature for ice has also been introduced so that more accurate global temperatures can be modeled between planetary systems.

3.3 One-Dimensional EBMs

The single hemisphere one-dimensional models that are distinguished primarily by their ten-degree zones vs. one-degree zones were both kept as individual versions due to an interesting scenario: one-degree zones glaciate significantly "earlier" as solar fraction is reduced, compared to the same ten-degree zone model parameters. **Figure 13** shows the ten-degree model on the left, and the one-degree model on the right for the same solar fraction of 0.825, which at present day insolation values should be low enough to cause the runaway glaciation effect observed at under ~0.83 Sx. It is not until the solar fraction reaches 0.800 that the Earth becomes completely glaciated in the ten-degree model.

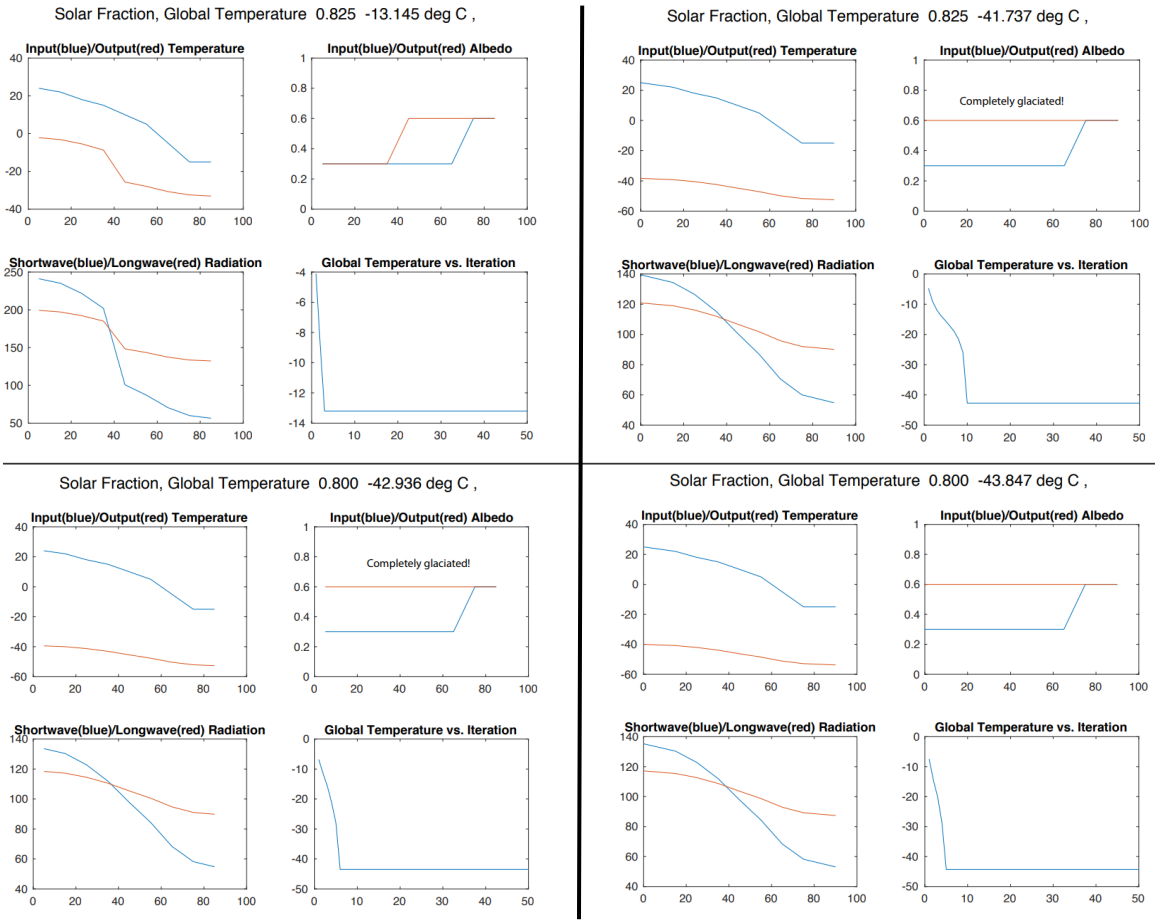

Figure 13: Differences between OneD_EBM 10-degree (left) and 1-degree (right) resolution model outputs for S_x set to 0.825 and 0.800.

Initial input albedo (AL) was interpolated from the Henderson-Sellers and McGuffie (2005) ten-degree zones for the one-dimensional two-hemisphere model. This allowed for the first step towards a global two-dimensional model in its original annual average form.

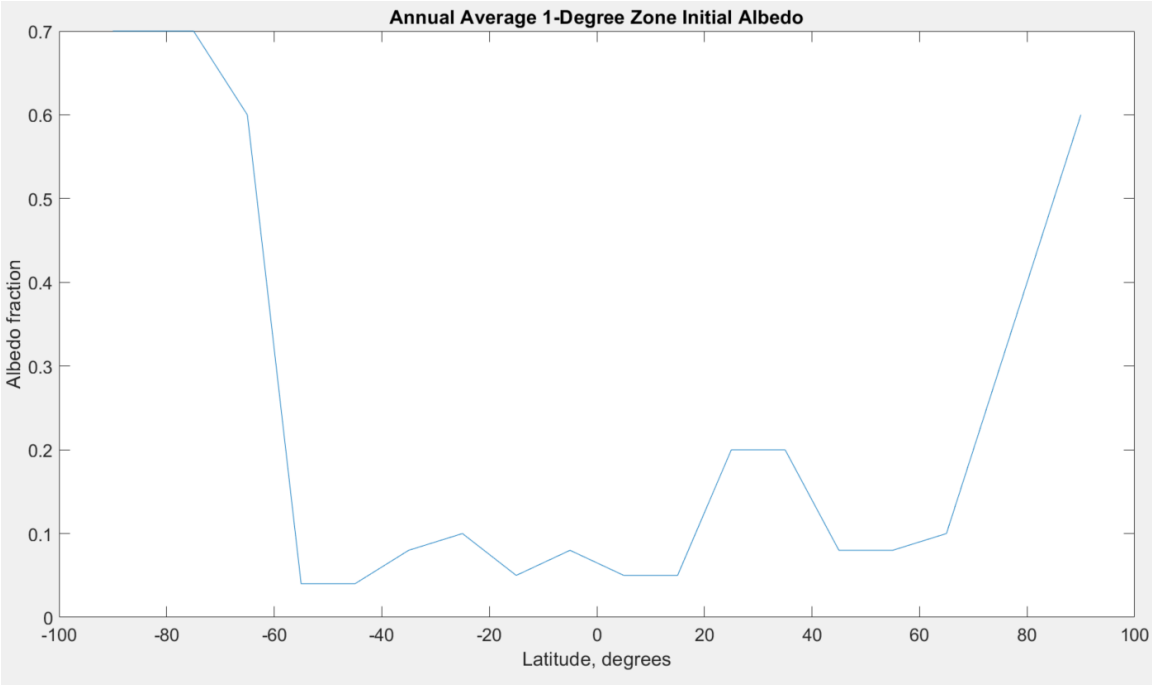

Figure 14: Annual averaged starting albedo for a two-hemisphere one-dimensional EBM at one-degree resolution across all latitudes (Henderson-Sellers and McGuffie, 2005).

3.4 Two-Dimensional CERES Realistic Albedo

Like the one-dimensional EBMs, input albedo is required for each zone of latitude, for Earth this is based on two variations, “Zres” binary land (1) vs. ocean (0) averaged over all longitudes, or realistic CERES EBAF surface albedo. For Mars, Mars Global Surveyor Thermal Emission Spectrometer (MGS TES) could be used. To replace the binary land (1) and ocean (0) “Zres” map as the initial surface albedo map for TwoD_CERES.m, realistic surface albedo maps were created using Clouds and the Earth’s Radiant Energy System (CERES) Energy Balanced and Filled (EBAF) data products.

CERES EBAF Level 3b provides a global record of monthly averages of shortwave and longwave fluxes separated into upward and downward traveling fluxes (Loeb et al., 2018). Clear-sky fluxes that do not include interference from clouds of 1°x1° regions, allows the preparation of detailed albedo maps, by calculating the ratio of upward traveling shortwave radiation (Sup) to downward traveling shortwave radiation (SDown), and averaging over 15 years of data from 2000-2014 using NcreadCERES.m. Data outliers near the poles occur during winter months where SDown = 0 due to 24 hours of perpetual night due to the 23.5-degree tilt (obliquity) of the Earth rotational axis. To remove these outliers, the latitudinal line of zero insolation per month was tracked; all latitudes above the line for that month were set to an albedo of 1.0.

Table 1: Monthly latitudinal extent of the polar zone of perpetual night.

Month	Extent	Latitude of Perpetual Night
	South Pole	
March	90°-0°	90 °S
April	90°-8°	82 °S
May	90°-16°	74 °S
June	90°-24°	66 °S
	North Pole	
September	90°-0°	90 °N
October	90°-8°	82 °N
November	90°-16°	74 °N
December	90°-24°	66 °N

Figure 15 shows the estimated CERES surface albedo maps for the equinoctial months of March (**a**) and September (**c**), averaged from 2000-2014, where perpetual night

is not a factor at either pole. In comparison, the CERES surface albedo map for June (**b**) shows how southern Winter Solstice involves the maximum areal extent delineated at 66.5°S for perpetual night in the Southern Hemisphere. Similarly, (**d**) shows Northern Hemisphere Winter Solstice extent for December. Supplementary material, *Appendix A - Input Albedo Maps for TwoD EBM*, contains all remaining months used for albedo input that could not fit within the main body of this thesis.

The CERES surface albedo maps provide detailed albedo information for land and oceans. Non-ice land albedo ranges from approximately 0.1 - 0.53, compared to ocean albedo which is lower, ranging from 0.027 – 0.14 based on the annual CERES input albedo map, or more conservatively 0.05 - 0.1 (Seitz, 2011). Ocean surface albedo is the reflectivity of the ocean surface to incoming shortwave radiation. It is a major factor in shaping the flow of energy atmospheric and ocean exchanges, and is vital for accurately measuring the surface radiation budget (Li et al., 2006). Ocean surface albedo has been the product of several schemes, which incorporate numerous variables. Solar zenith angle is common among all schemes; other parameters such as wind speed, which becomes more important for larger solar zenith angles, but less important as cloud optical depth increases, are also considered in differing schemes (Li et al., 2006). The CERES data product, using a top-of-atmosphere (TOA) upward clear-sky flux, is insensitive to these different formulations of ocean surface albedo. Cloud forcing is thus more important in comparison with clear-sky forcing with regard to global energy balance of the model (Li et al., 2006). This implication holds true for the 2D EBM, as changes to

cloud albedo (CALB) result in significant output differences. All twelve processed monthly CERES input maps are in the Supplementary Materials (Appendix A).

a.

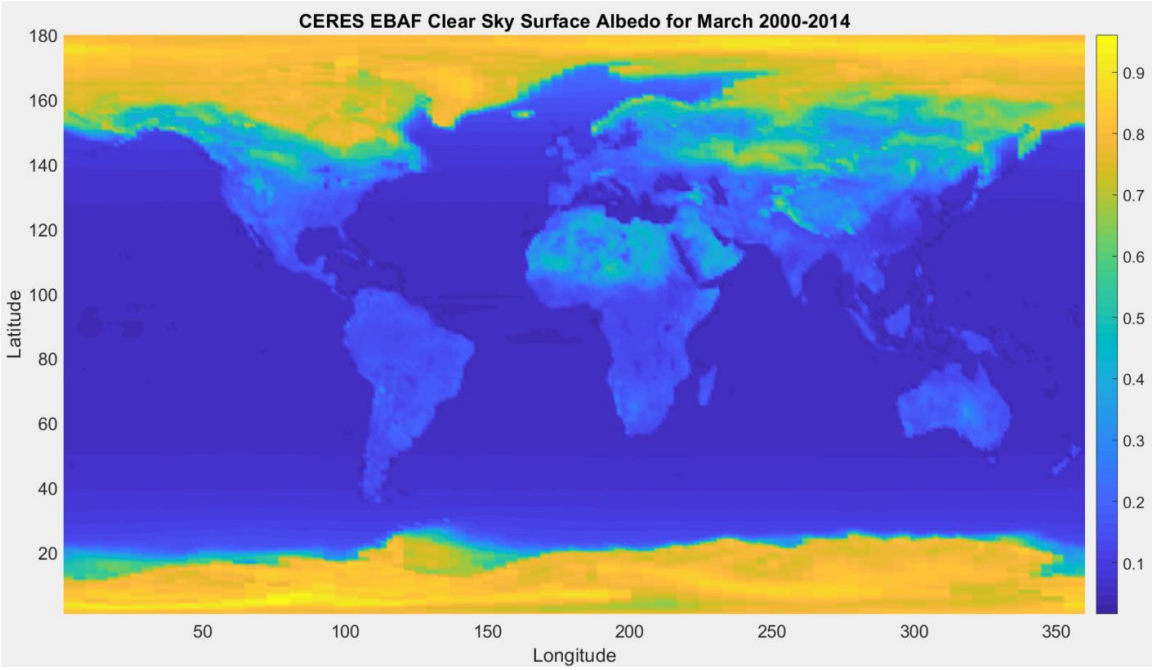

b.

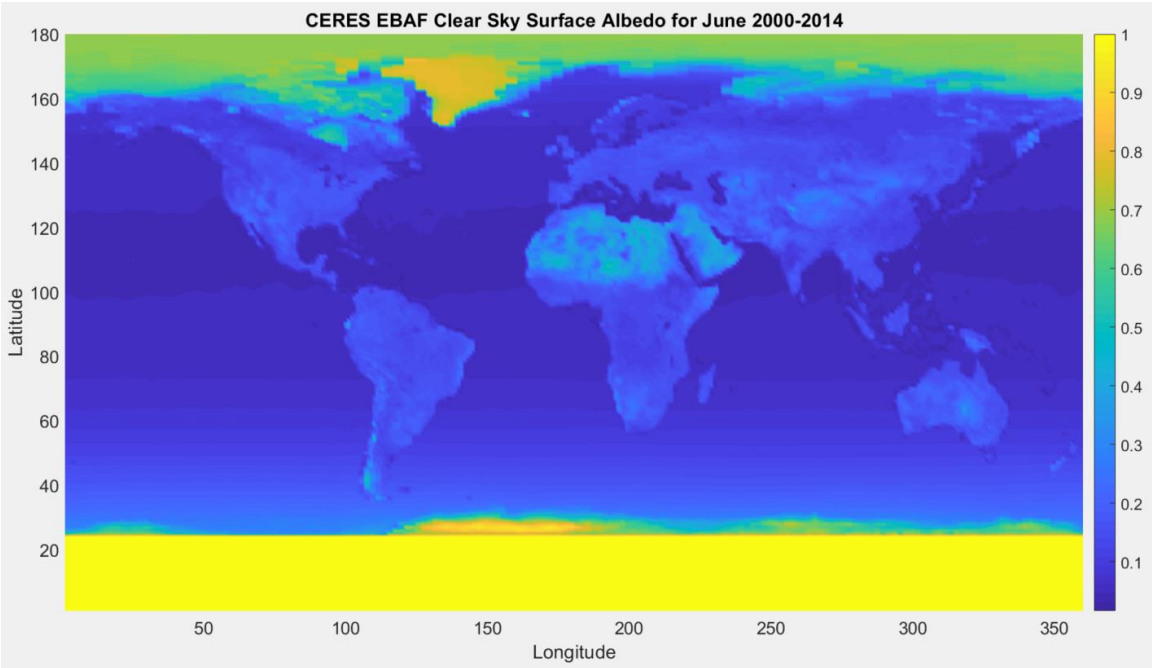

c.

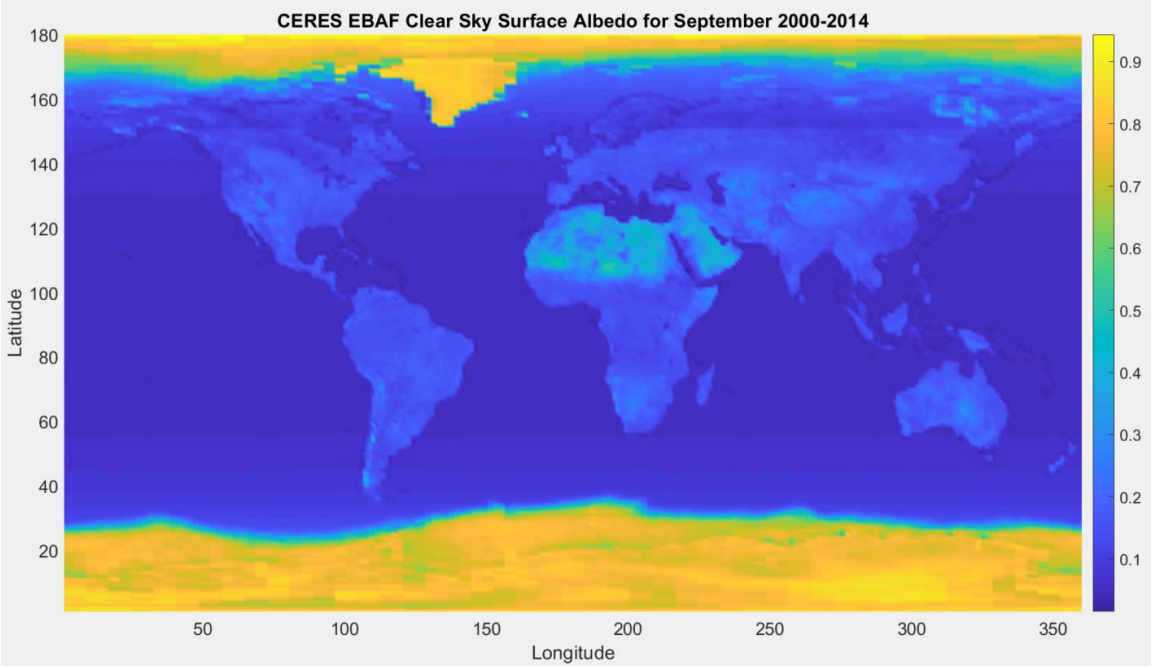

d.

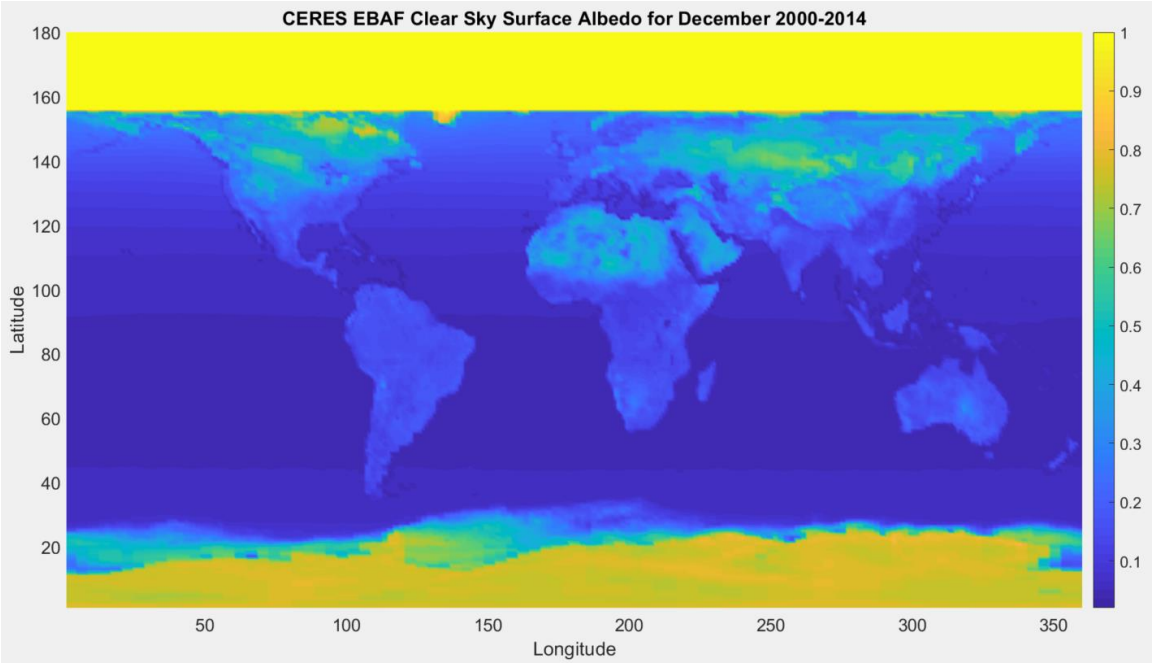

Figure 15: CERES Surface Albedo Maps for the equinoctial (March (a) and September (c)) and solstitial (June (b) and December (d)) months averaged from 2000-2014.

3.5 Monthly Insolation Forcing

To replicate planets other than Earth, and to improve the annual output for Earth, a sixth order Legendre series expansion for mean annual insolation (S) was instituted, along with input variables for obliquity (β) and orbital eccentricity (e). Sixth order Legendre polynomial expansion for Earth, Mars, and Pluto for minimum, current, and maximum obliquity and orbital eccentricity (Laskar et al., 2004a), reveals the importance of accounting for the astronomical parameters (**Figure 16**).

This method, while effective for annual scale model scenarios where the mean value is preferred, such as in TwoD_Zres, is ultimately an additional input used to calculate for global temperature. With the use of realistic monthly CERES input albedos, monthly insolation inputs are introduced for Earth from Kostadinov and Gilb's script "Earth_Orbit_V2.m". Insolation was computed for three time slices in the glacial-interglacial cycle: present-day (0 ka), the Last Glacial Maximum (LGM, 24 ka), and the Last Interglacial (Eemian, 128 ka) (**Fig. 18**, **Tab. 2**).

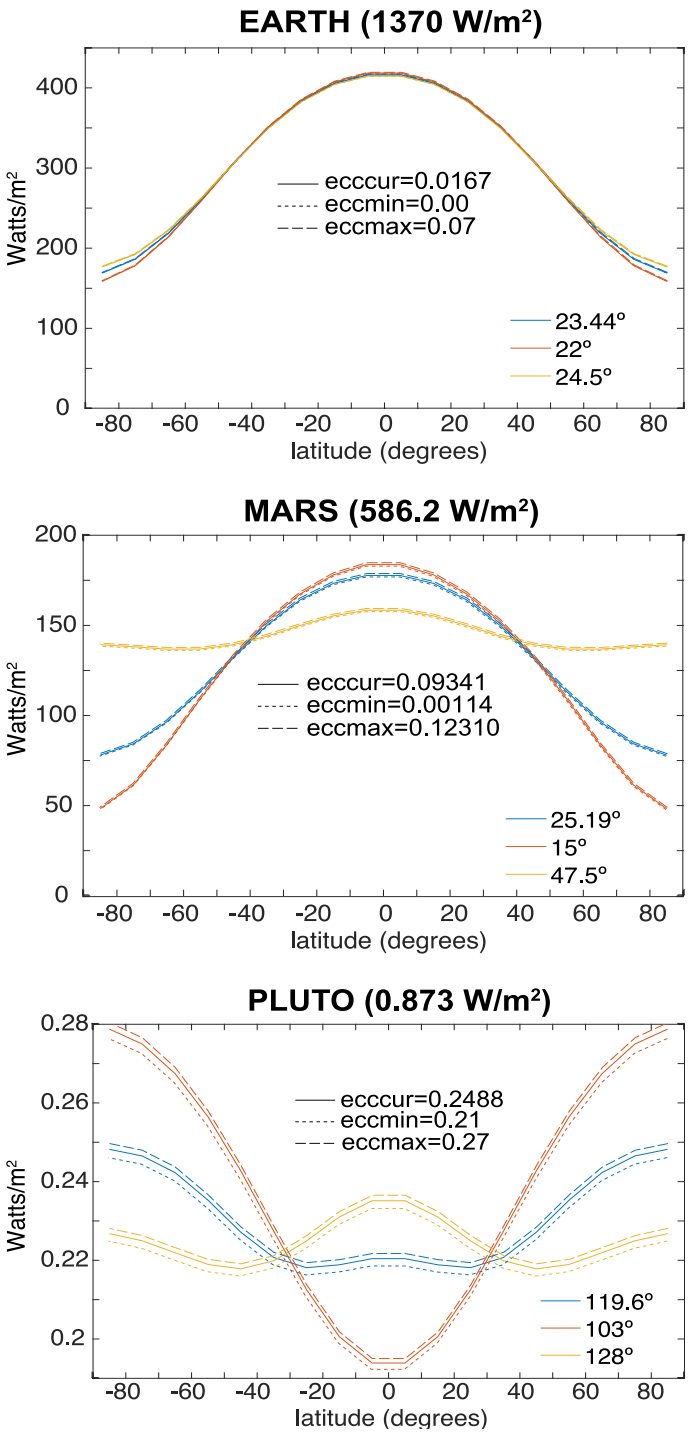

Figure 16: Mean annual insolation S(θ) based on order 6 Legendre polynomial expansion, for Earth (A), Mars (B), and Pluto (C), for different obliquities (colors) and orbital eccentricities (line types).

Earth's climate, forced through Milankovitch parameters acting on insolation, undergoes glacial-interglacial cycles which can be tracked throughout time. The changes in these parameters, which include the Earth's orbital eccentricity, and obliquity, affect the insolation, and the duration and timing of the seasons. Kostadinov and Gilb (2014) calculate insolation using the equation (Berger et al., 2010):

$$\textbf{Equation 14: } W = S_0 \left(\frac{a}{r}\right)^2 \cos z$$

where S_0 is the solar constant, a is the length of the semi-major axis of the Earth's orbit, and r is the Earth-Sun distance:

$$\textbf{Equation 15: } r = (1 - e^2) \,/\, (1 + e * cos(v))$$

where e is the Earth's orbital eccentricity, true anomaly $v = \lambda - \omega$, with ω the longitude of perihelion relative to moving spring equinox and λ the true longitude of the Sun (**Figure 17a**).

The angle z is the zenith angle of the Sun relative to the zenith (overhead) point Z in the local sky, and:

$$\textbf{Equation 16: } \cos z = \sin\theta \sin\delta + \cos\theta \cos\delta \cos H$$

θ is geographical latitude, H is the hour angle of the Sun (H=0 is 12 noon); and the Sun's declination δ, varies over the year according to the true longitude of the Sun, λ, and Earth's obliquity ε:

$$\textbf{Equation 17: } \sin\delta = sin\lambda \sin\varepsilon$$

The relevant variables for the annual orbit of the Earth around the Sun and for the local horizon are shown in **Figure 17b**.

a.

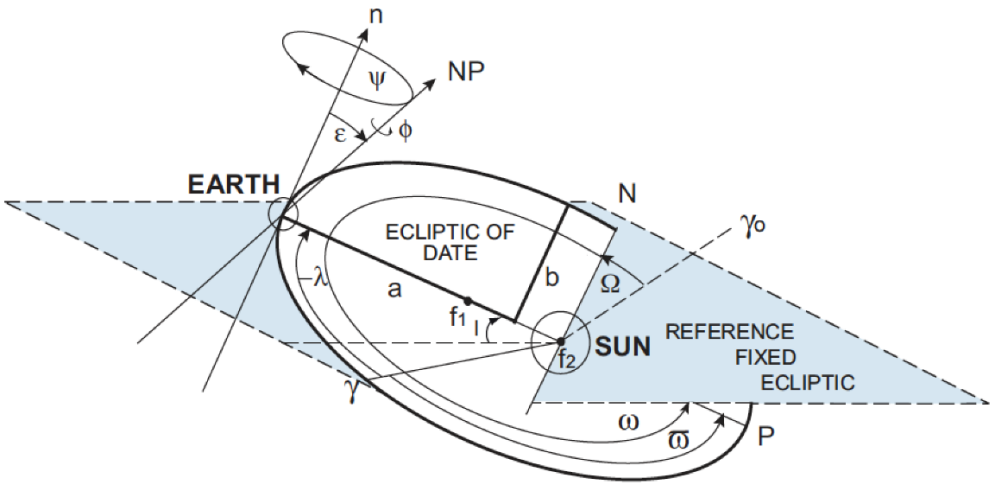

b.

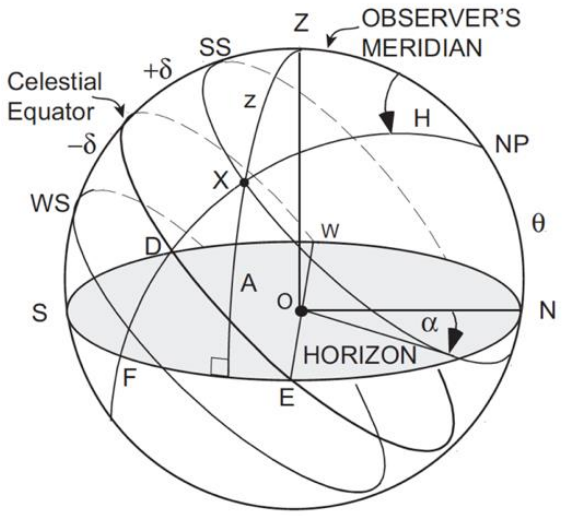

Figure 17: Earth's astronomical parameters. a. The orbital elements, from Figure 3 of Hinnov (2013). b. The celestial sphere with local horizon at geographical latitude θ; "X" marks the location of the Sun at a time prior to meridian transit (noon), from Figure 6 of Hinnov (2013).

a.

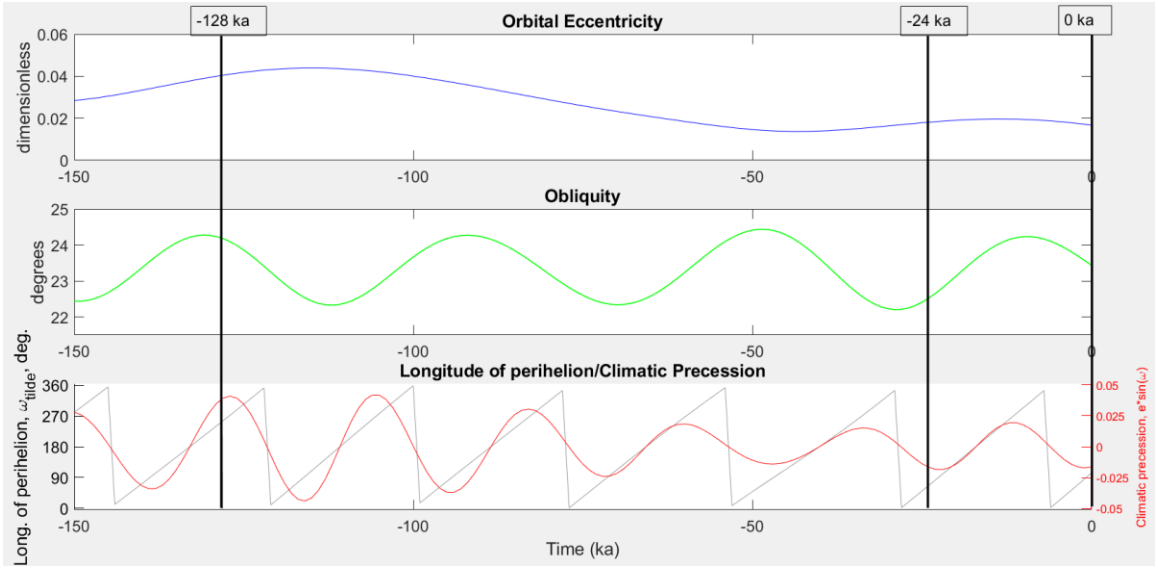

b.

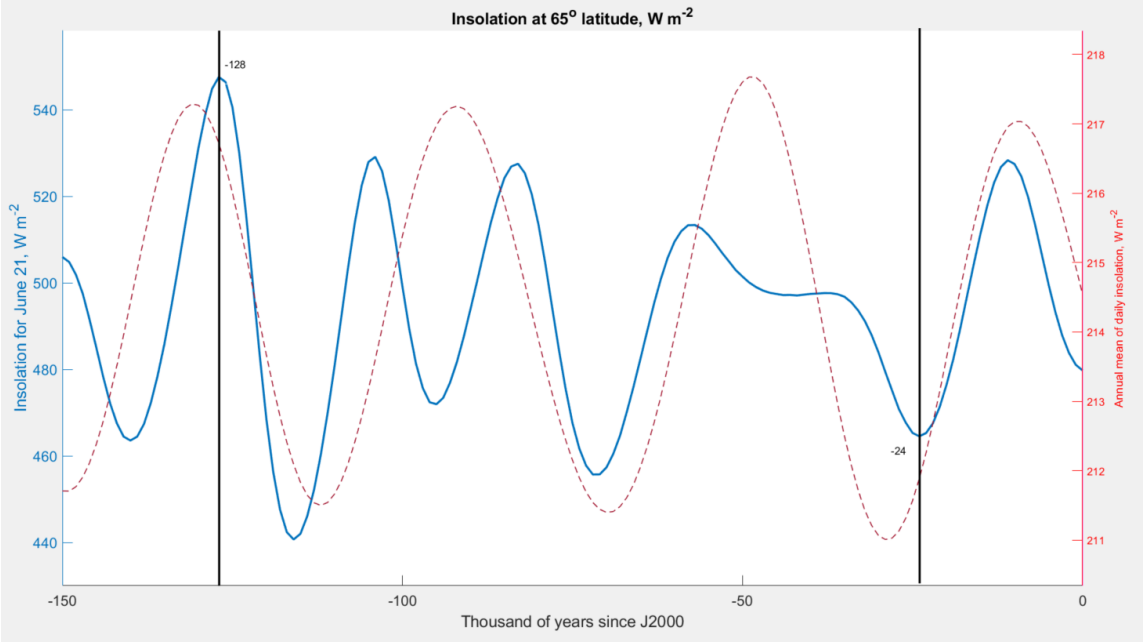

Figure 18: Kostadinov and Gilb's *Earth_orbit-V2.m* calculation of June 21 insolation at 65º North, 0-150 ka. Time slices 0 ka, 24 ka and 128 ka are indicated by vertical lines. a. Orbital parameters (time slice values in Table 2); b. daily insolation for June 21 (blue) and annual mean daily insolation (red) in Wm^{-2}.

Table 2: Earth's astronomical parameters according to the solution of Laskar et al. (2004a) for three time slices at 0 ka, 24 ka, and 128 ka.

	0 ka	24 ka	128 ka
Orbital Eccentricity $\boldsymbol{e}$	0.0167024	0.0180950	0.0404890
Obliquity of the Ecliptic ε	23.4393 deg	22.5230 deg	24.1743 deg
Precession/Longitude of Perihelion ϖ	102.9179 deg.	66.1956 deg	256.9384 deg

Earth_orbit_v2_1.m was modified to an increased resolution of one degree across all latitudes and every day (**Fig. 19**). From this, the average monthly insolation was computed from the daily insolation for the three time slices (**Fig. 20**).

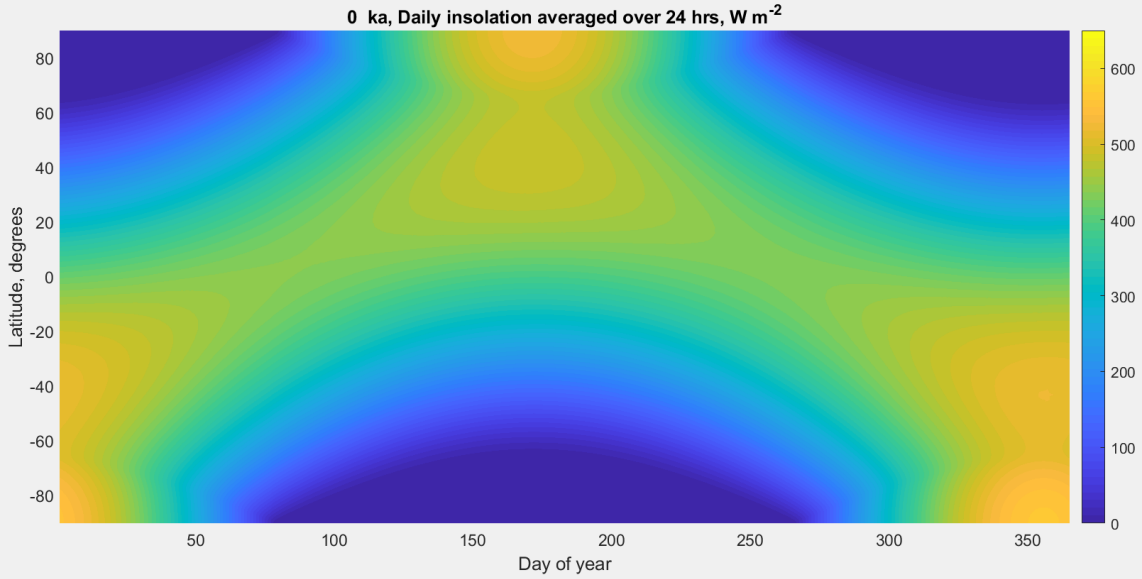

Figure 19: Present-day (0 ka) daily insolation for 365 days; color scale in W/m^2.

a.

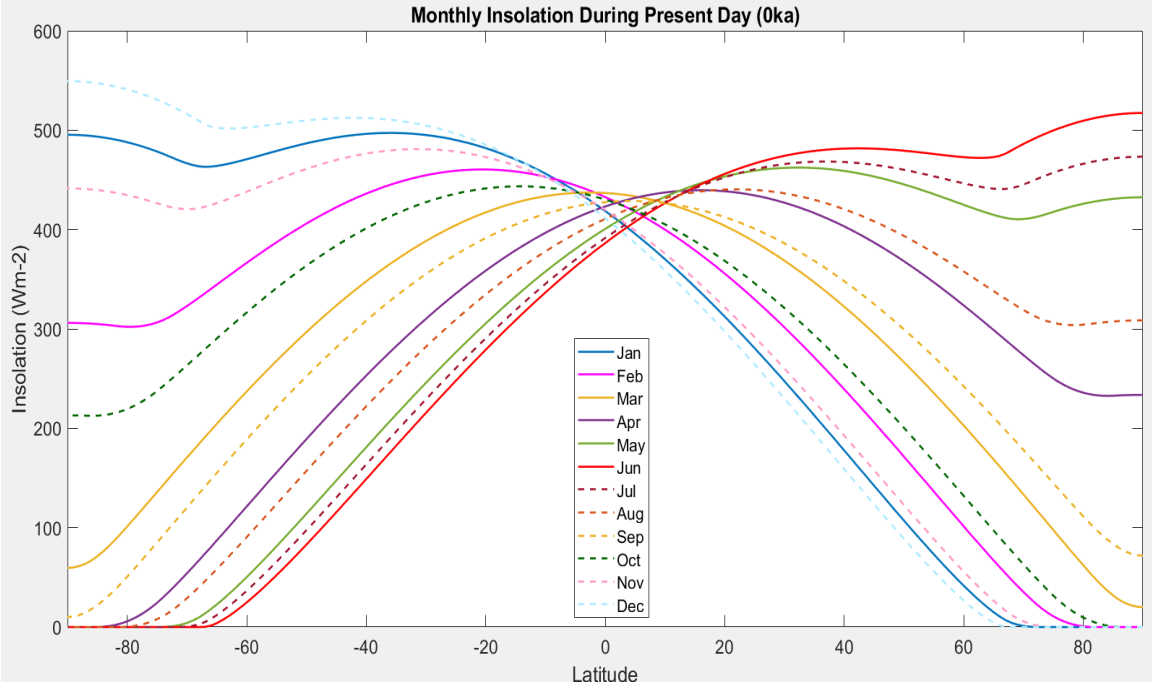
Monthly Insolation During Present Day (0ka)
Insolation (Wm-2)
Latitude
Jan
Feb
Mar
Apr
May
Jun
Jul
Aug
Sep
Oct
Nov
Dec

b.

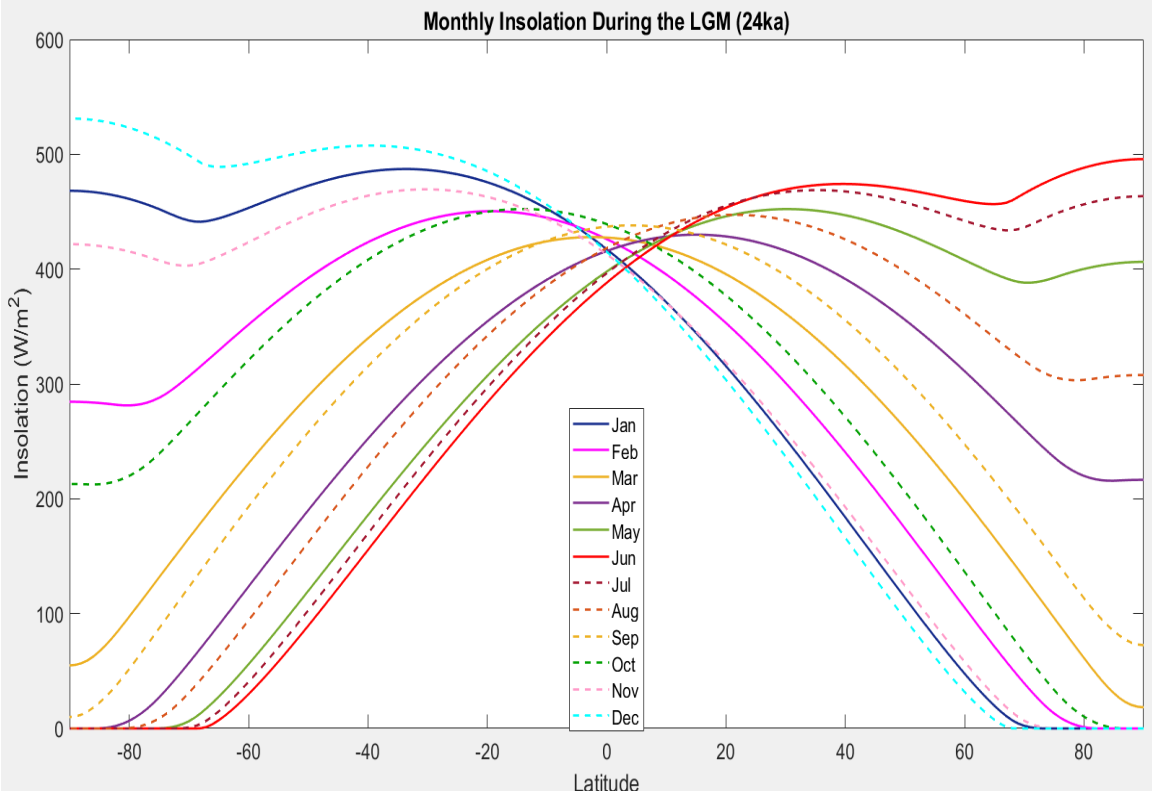
Monthly Insolation During the LGM (24ka)
Insolation (W/m2)
Latitude
Jan
Feb
Mar
Apr
May
Jun
Jul
Aug
Sep
Oct
Nov
Dec

c.

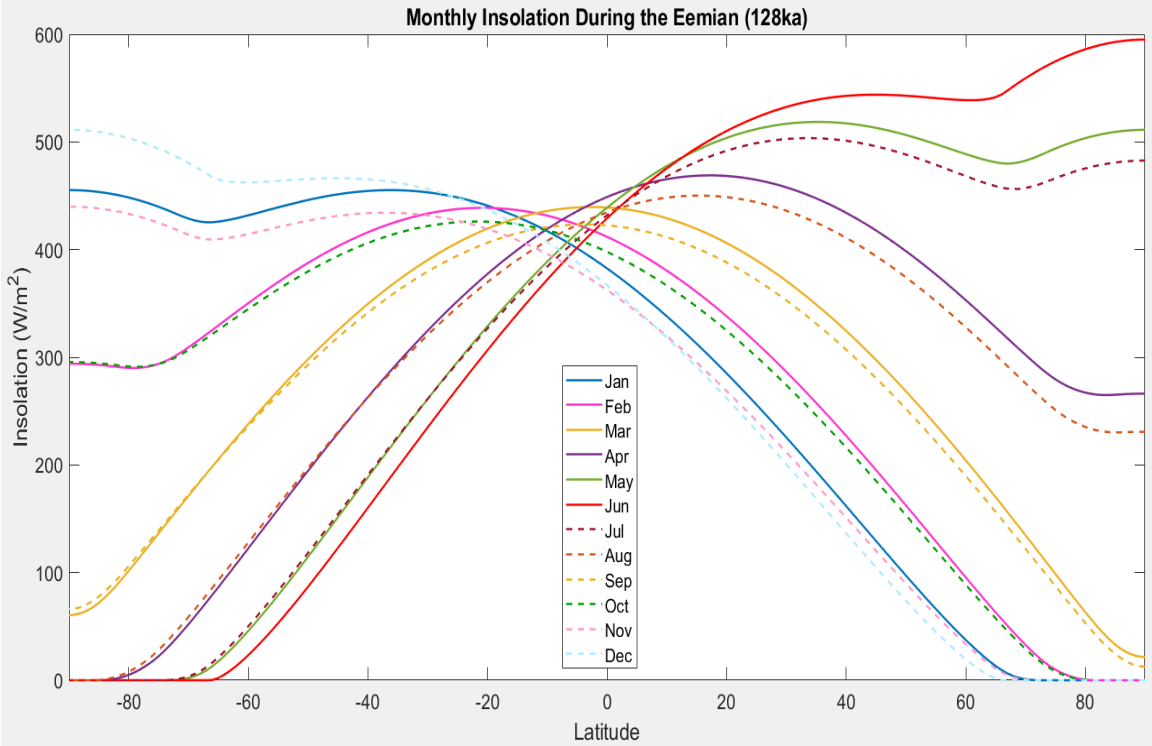

Figure 20: Monthly insolation for 0ka (a), 24ka (b), and 128ka (c) based on output from Earth_orbit_v2_1.m (Kostadinov and Gilb, 2014).

Summer insolation differs for the three time slices in both hemispheres. The asymmetric curves between the two warmest months, June in the Northern Hemisphere, and December in the Southern Hemisphere, do not balance one another. During the Eemian (128 ka), northern June insolation far exceeds southern December insolation, while during both the LGM and present day, southern December insolation exceeds northern June insolation. This imbalance occurs because, for example, for the present day at Southern Summer (Northern Winter), Earth is very close to perihelion, the shortest distance to the Sun, and thus receives the most insolation, while present-day Northern

Summer, at aphelion, receives comparatively less. The values are different in the Eemian because perihelion has shifted from ω=103º to 256º (**Table 2**). Another feature that stands out in the peak solstice months (June and December) are small local decreases in insolation at the Arctic and Antarctic circles. This is due to the competing effects of hours of daylight vs. intensity of the radiation received at 66º North (and South) at the solstices.

If all of these months are averaged together to obtain annual insolation, it compares closely with Hartmann's "Annual-mean, solstice and equinox insolation as functions of latitude" curve (Hartmann, 2016, Figure 2.7, reproduced here in **Figure 21**). This is also equivalent to the global annual insolation of Nadeau and McGehee (2017).

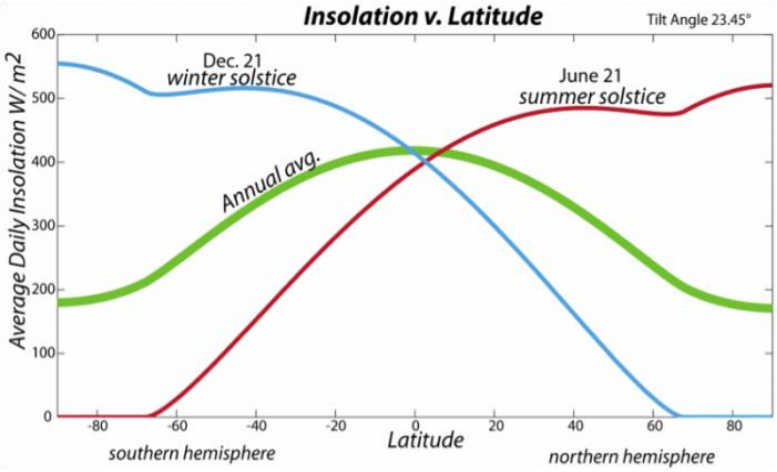

Figure 21: Average daily insolation (W/m^2) over all latitudes for the winter solstice (blue), summer solstice (red), and annual average (green). From Hartmann (2016).

Insolation drops to zero past the point of perpetual night. Equinox months, March and September, remain the only two months with insolation received across every latitude, and as such produce maps such as **Figure 30a** and **30e.**

As time proceeds into the past the zone of perpetual night changes by a few degrees due to the change in obliquity. In the present day, with an obliquity of 23.5°, the largest zone of perpetual night will be from 66.5° to 90º at Winter Solstice. That value, when changed to 68° for June during the LGM (given obliquity of 22.52º, see **Table 2),** for a 1-degree resolution does not record a significant difference. Therefore, 66.5° was kept for all three time slices.

CHAPTER 4: RESULTS

4.1: Zero-Dimensional Model Outputs

Using minimal variables to model a single body system, Zero_D_EBM allows for the basic blackbody and greenhouse temperatures in °C for a planet to be modeled. Using only the solar constant, solar fraction (S_x), planetary albedo (α), and the greenhouse longwave coefficients A and B, global temperature can be procured.

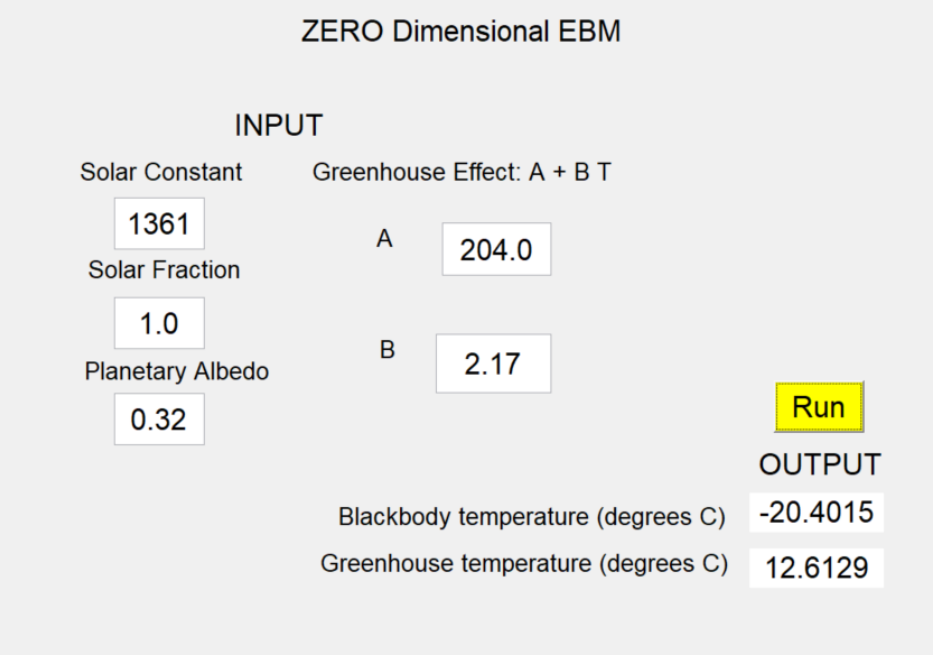

Figure 22: The GUI for Zero_D_EBM showing the default parameters and their results.

Zero_D_EBM produces a blackbody temperature of -20.4°C, and a greenhouse temperature of 12.6°C, which is close to the accepted observed global surface

temperature of 14°C by Jones et al. (1999). Changing A to 201.0 W/m^2 results in 14°C exactly. Using an S of 1370, with original A and B values results in a greenhouse temperature of 13.3°C.

4.2: One-Dimensional Model Outputs

One-dimensional EBM's require starting input zonal temperatures (TSTART). From these starting points, the 1D-EBM runs towards equilibrium for 250 iterations as heat is transferred poleward from the equator. One-dimensional EBM's also require a starting input zonal surface albedo (AL). Other key inputs are daily average solar radiation, A, B, and mean annual insolation, which is constrained by obliquity and orbital eccentricity.

Here, the 1D 2 hemisphere EBM's outputs (**Table 4, Figure 24**) are matched against the outputs of The Shodor Education Foundation's 1 hemisphere energy balance model (Found at: http://www.shodor.org/master/environmental/general/energy/energy.html), using identical inputs to achieve similar results. The Shodor model uses information garnered from McGuffie and Henderson-Sellers original 1997 model, and thus only displays the outputs for a single hemisphere. Both models were set with input information of: A = 204 W/m^2, B = 2.17 $W/m^{2o}C$, C = 3.87 $Wm^{-2}/°C$, T_c = -10°C, CALB = 0.3, S_x = 1.0, SOLCON = 1370 W/m^2, and α_{ice} = 0.62. Initial temperatures, and S (annual radiation) are shown in **Table 3** and **Figure 23**, along with the outputs for the Shodor model.

Table 3: Inputs and outputs of Shodor energy balance model (Shodor, 1998)

Zones	Calculated Zone	S	Initial Temp	Initial Albedo	Final Albedo	Final Temp	Radiation in	Radiation out
80-90	85	0.5	-16.9	0.62	0.62	-13.535	171.25	174.629
70-80	75	0.531	-12.3	0.62	0.62	-12.867	181.867	176.078
60-70	65	0.624	-5.1	0.30	0.30	0.459	213.72	204.996
50-60	55	0.77	2.2	0.30	0.30	6.254	263.725	217.571
40-50	45	0.892	8.8	0.30	0.30	11.097	305.51	228.08
30-40	35	1.021	16.2	0.30	0.30	16.217	349.692	239.19
0-30	25	1.12	22.9	0.30	0.30	20.147	383.6	247.718
0-20	15	1.189	26.1	0.30	0.30	22.886	407.232	253.662
0-10	5	1.219	26.4	0.30	0.30	24.077	417.507	256.247

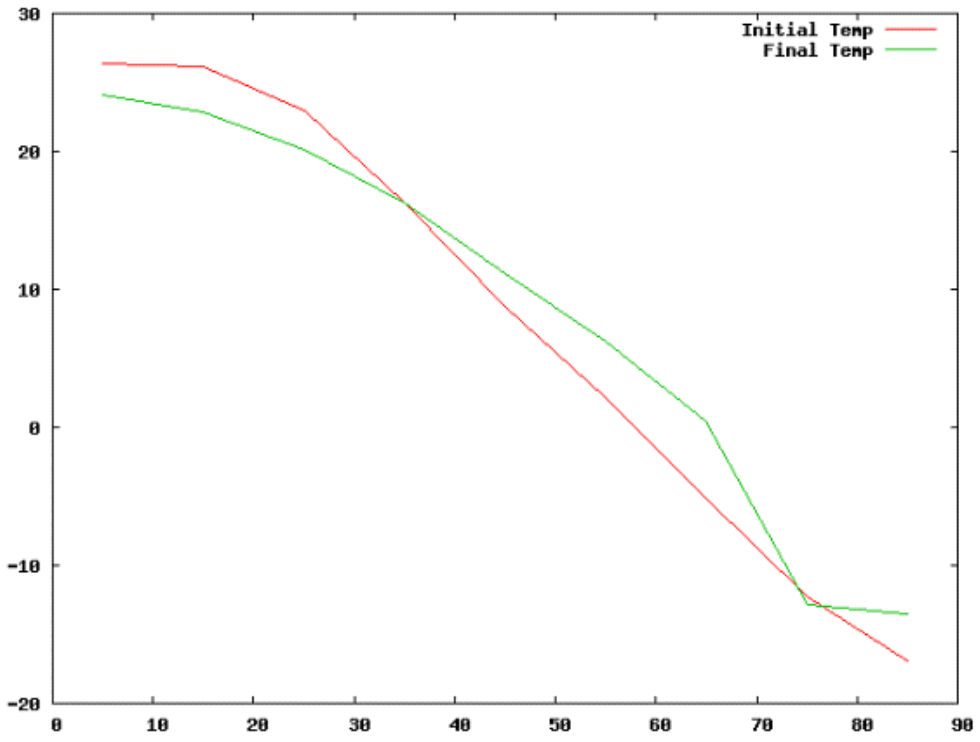

Figure 23: Initial and final temperature across the Northern hemisphere (Shodor, 1998)

Table 4: Outputs from the 1D 2 hemisphere EBM, parameters set identically to Shodor.

Latitude	Temperature	Albedo	Cloudines	Longwave	Abs-Sol
90	-12.7388	0.6200	0.5200	170.7149	64.1814
80	-11.6470	0.6200	0.5800	172.4330	70.7757
70	1.9742	0.3000	0.6200	201.5569	153.0474
60	6.9184	0.3000	0.6300	212.1774	182.9105
50	12.2732	0.3000	0.5700	224.4484	215.2539
40	17.2103	0.3000	0.4600	236.3553	245.0735
30	21.0964	0.3000	0.4000	245.4393	268.5460
20	23.6468	0.3000	0.4200	250.7565	283.9500
10	24.8727	0.3000	0.5000	252.5487	291.3543
-10	24.8727	0.3000	0.5000	252.5487	291.3543
-20	23.6468	0.3000	0.4200	250.7565	283.9500
-30	21.0964	0.3000	0.4000	245.4393	268.5460
-40	17.2103	0.3000	0.4600	236.3553	245.0735
-50	12.2732	0.3000	0.5700	224.4484	215.2539
-60	6.9184	0.3000	0.6300	212.1774	182.9105
-70	1.9742	0.3000	0.6200	201.5569	153.0474
-80	-11.6470	0.6200	0.5800	172.4330	70.7757
-90	-12.7388	0.6200	0.5200	170.7149	64.1814

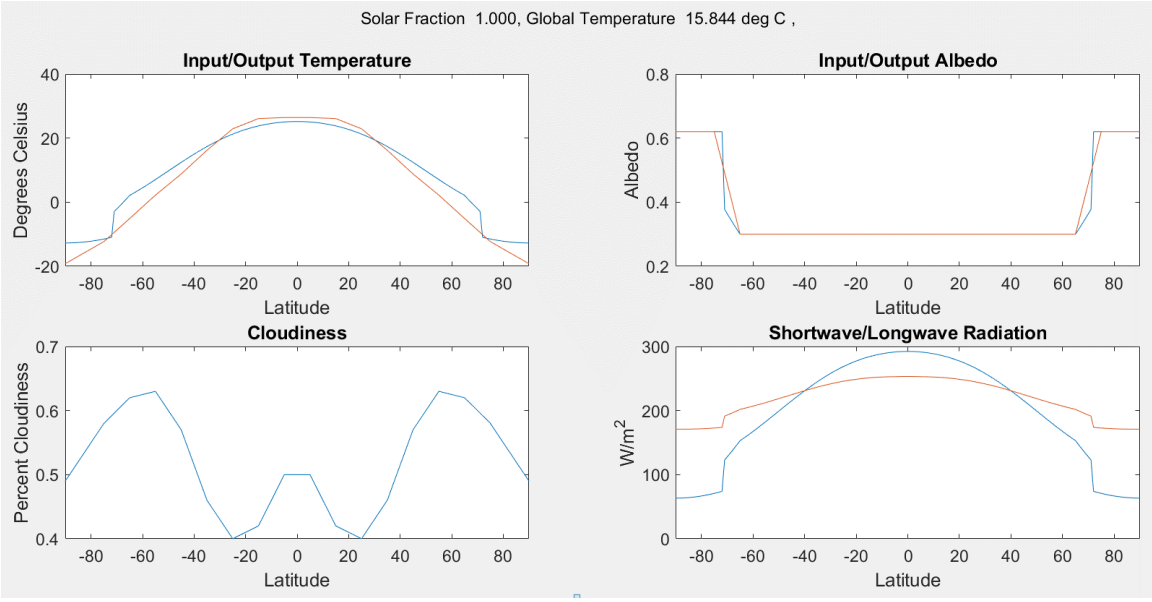

Figure 24: Outputs from the 1D 2 hemisphere EBM, parameters set identically to Shodor. Red lines are inputs, and outgoing longwave radiation. Blue lines are outputs, and incoming shortwave radiation. Cloudiness (blue) is input.

The One-D 2 hemisphere model reproduces Shodor's values closely (compare with **Table 3**). Zonal temperatures agree to within 1-2°C across all latitudinal zones. Based on 1370 W/m^2 input, global mean temperatures indicate 15.84°C (1D 2 hemisphere EBM) versus 14.77°C (Shodor), potentially due to differences in S, given the One-D model uses sixth-degree Nadeau mean annual insolation.

Equation 13 allows for a simple simulation of the effect that solar radiation has on the ice-line and temperature. Solar fraction and surface temperature retain a fairly linear relationship up until the solar fraction values of 0.8307093-0.8307094 of S, where the entire globe begins to reach glaciation temperatures, and the temperatures take on a runaway effect (**Figure 25**). The 1D 2 hemisphere EBM reproduces a similar

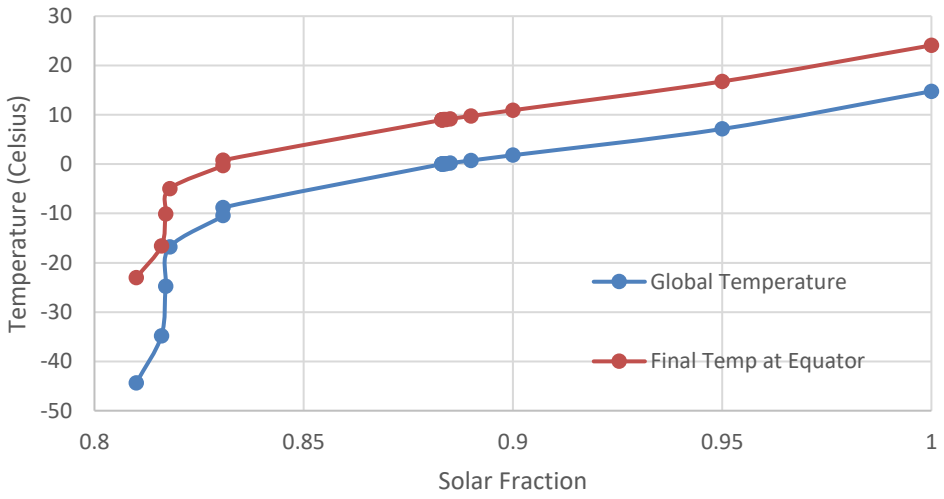

Figure 25: The relationship of temperature (°C) and the fraction of solar flux. Modeled using data from the Shodor Foundation's version of the model.

relationship, using Shodor input values, S_x 0.84 = -9.69°C, S_x 0.83 = -14.98°C, and S_x 0.82 = -38.63°C.

At this critical tipping point with solar fractions of 0.8307093-0.8307094, the linear relationship breaks down. Even minute reductions in the solar fraction past that point have a much more significant effect on the surface temperature across all zones. **Figure 26** takes a closer look at the solar fraction at which all latitudes start to glaciate.

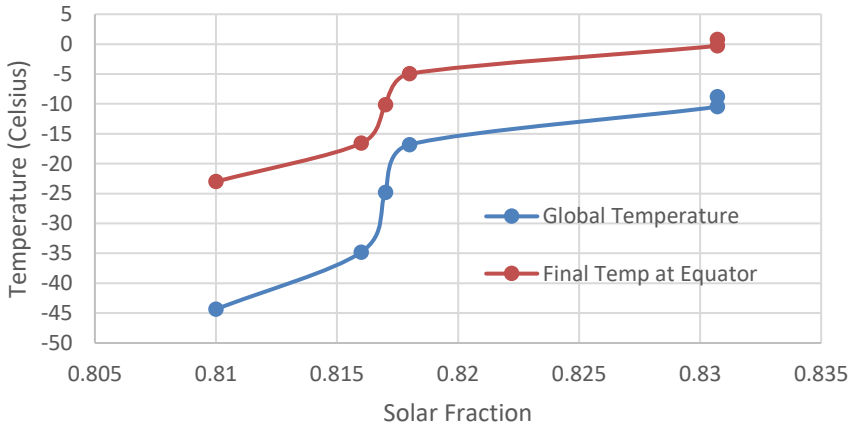

Figure 26: Relationship of surface T and SX from 0.81 and 0.83

All modeled solar fractions share similar trends across varying latitudes. **Figure 27** shows that the temperatures all seem to decrease linearly as they move up the latitudinal zones from equator to the North Pole. However, regardless of the current solar fraction used, all temperatures values significantly decrease between the latitudes of 65 and 75 degrees. Similar to **Figures 25** and **26**, there is a significant change in temperature that accompanies minute changes in the solar fraction.

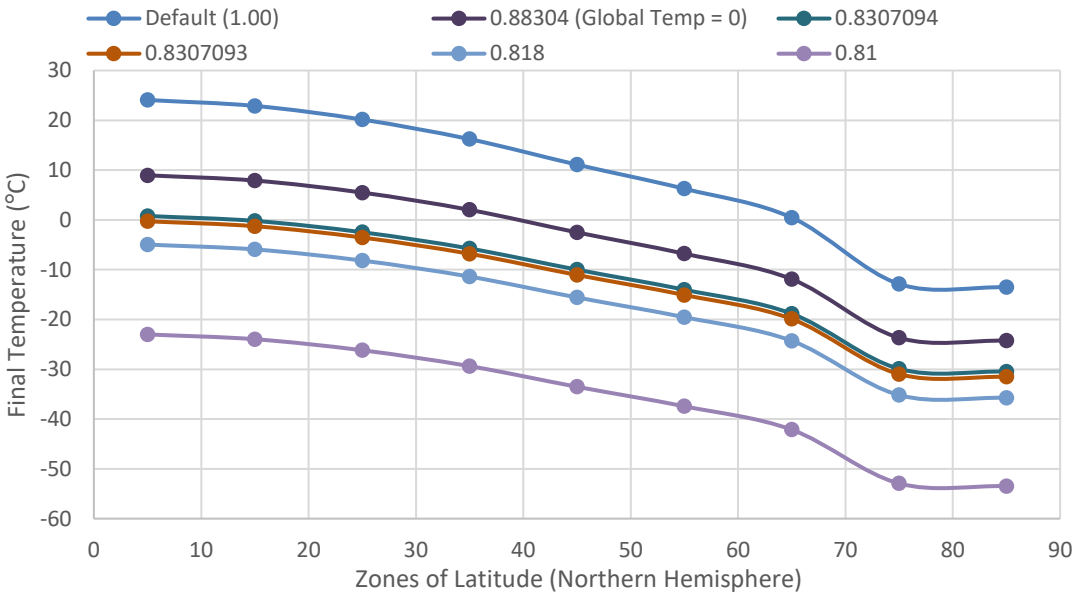

Figure 27: Output temperatures across zones of latitude for the Northern Hemisphere across varied solar fraction values

4.3: Two-Dimensional Model Outputs

Figure 28 shows the output temperature and albedo maps using the binary land-ocean (Zres) map as the input albedo map and **Figure 29** shows annual averaged CERES input albedo using the same mean annual insolation. Immediate differences will be seen on land, where, in the Zres version, the EBM maintains near-global land glaciation, even in the tropics. One will note that the strange "boxes" seen in the high latitudes are not errors, but instead a result of the continents in those lines of longitude decreasing the temperature of those zones.

The TwoD_CERES.m assumes no Earth rotation, no ocean-atmosphere circulation, no ocean heat capacity, and assumes a static present-day cloud fraction profile. Despite the absence of these fundamental dynamics, the model capably produces significant

differences in temperature and albedo when forced by LGM, Eemian, and present-day insolation. This allows for opportunities such as this for evaluating the significance of a specific parameter. Present day global temperatures have a baseline estimate of 14°C (Jones et al., 1999). TwoD_CERES.m produces similar, but slightly colder temperatures when cloud albedo (CALB) is set to 0.5, and slightly warmer temperatures when CALB is set to 0.3.

Without Earth rotation, atmospheric or oceanic circulation, and no cross-longitudinal movement of heat, preventing mixing between lines of longitude, TwoD_CERES is not a true representation the planet. In light of these results, future additions to the model should be considered. Specifically, looking at **Figure 30g**, areas of colder temperature contours in the northern high latitudes on lines of longitude corresponding to the North America and Eurasia. This colder region extends further in longitudes with more landmass, corresponding to Africa and the North American longitudes with more landmass. In some areas, this drag or cinching effect continues down to the Equator, where the contour lines show this extremely well around longitude -100. Both CERES and binary land-ocean Zres maps display this effect, and would likely be ameliorated with the introduction of circulation in a more complex model.

a.

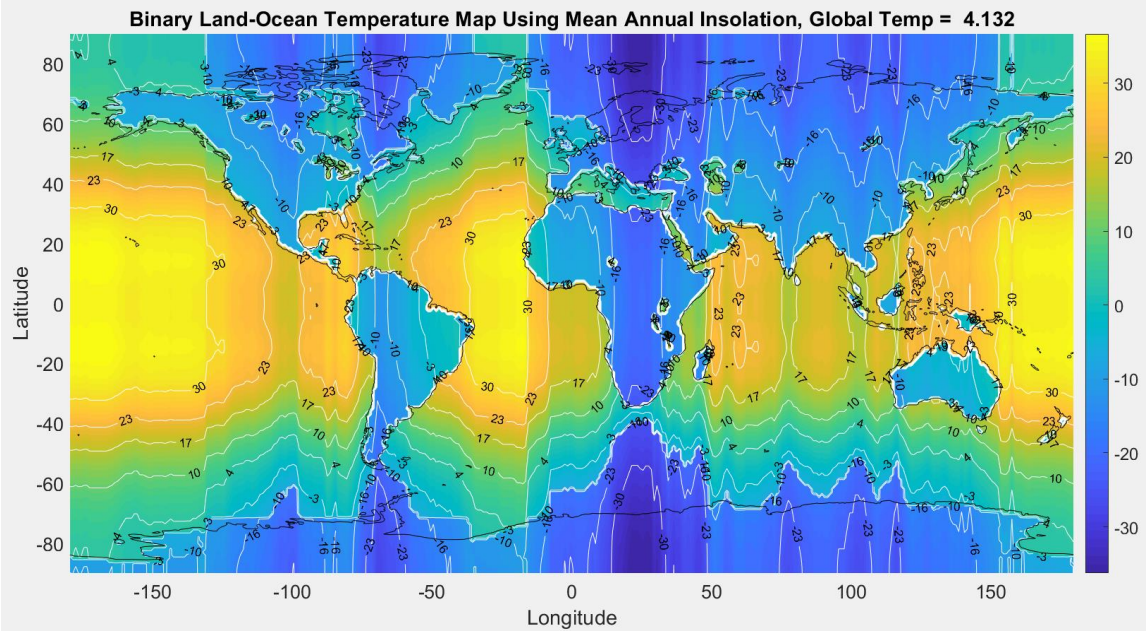

b.

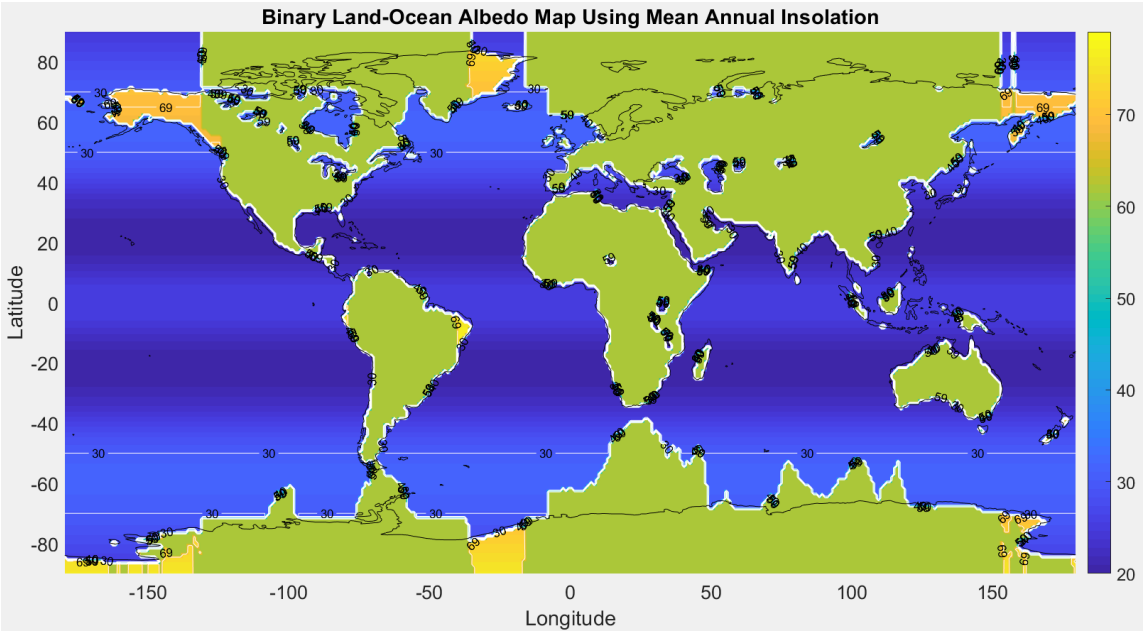

Figure 28: Outputs for the 2D EBM using binary land-ocean albedo input map (Zres) and Nadeau-forced mean annual insolation. Temperature (a) and Albedo (b). Default input values: S = 1361 W/m^2, A = 204 W/m^2, B = 2.17 W/m^2°C, C = 3.81 Wm^{-2}/°C, Tcrit = -10°C (global average), α_{ice} = 0.62, CALB = 0.5.

a.

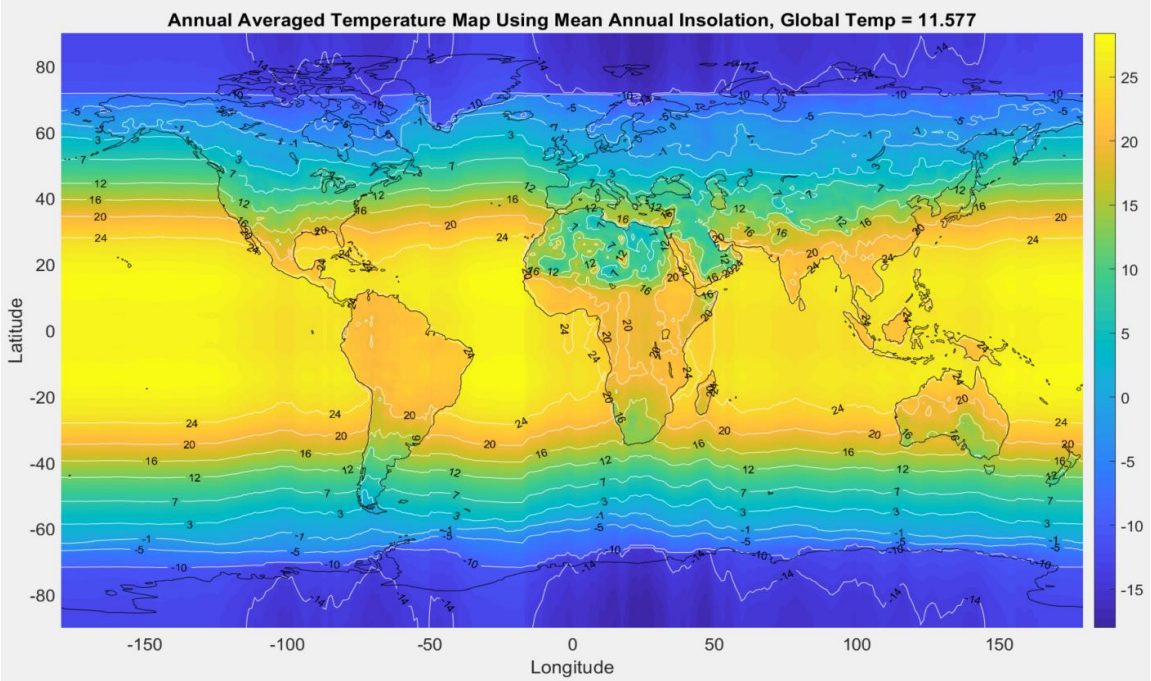

b.

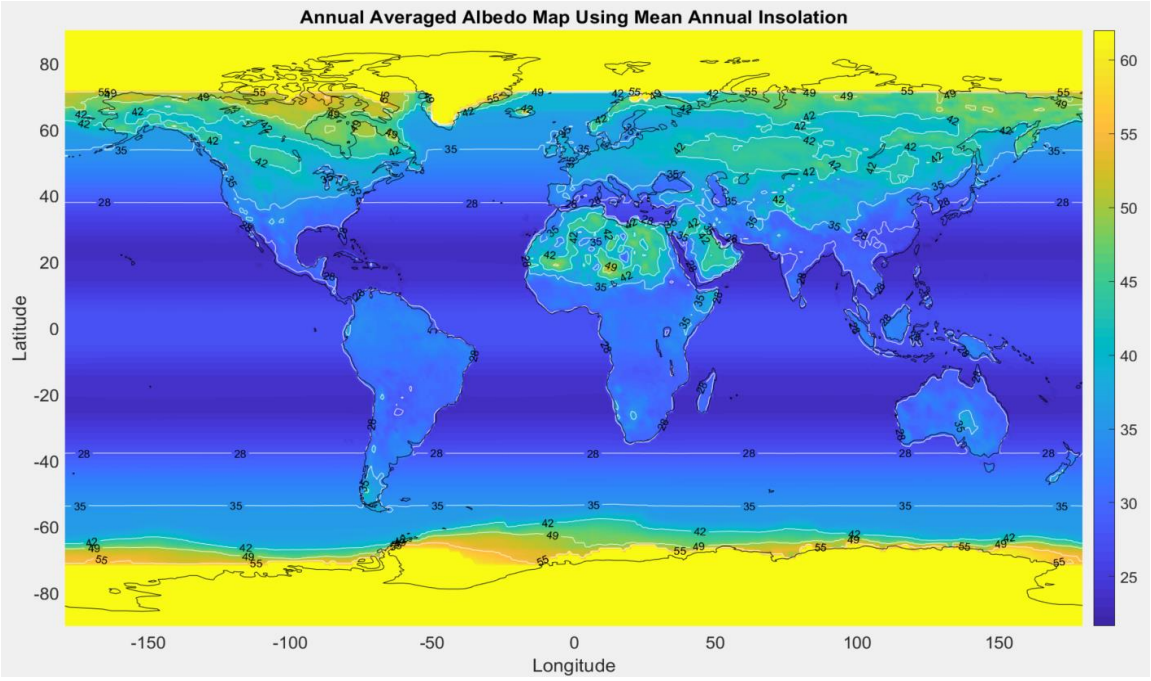

Figure 29: CERES albedo outputs using outputs for the 2D EBM using Nadeau-forced mean annual insolation. Temperature (a) and Albedo (b). Default input values: S = 1361 W/m^2, A = 204 W/m^2, B = 2.17 W/m^2°C, C = 3.81 Wm^{-2}/°C, Tcrit = -10°C (global average), α_{ice} = 0.62, CALB = 0.5.

Comparing CERES to the binary land-ocean data shows a significant change, not only as small changes to the 1°x1° zones, but to the global climate outputs as well. The differences confirm the importance of starting albedo in a system, producing two vastly different global scenarios.

Figure 30a-h display the temperature and albedo output maps for CERES across the two equinoxes and two solstices, the middle points of each season, March (**a, b**), June (**c, d**), September (**e,f**), and December (**g,h**) at present day (0 ka) insolation values, showing strong seasonal differences in global temperature and albedo.

a.

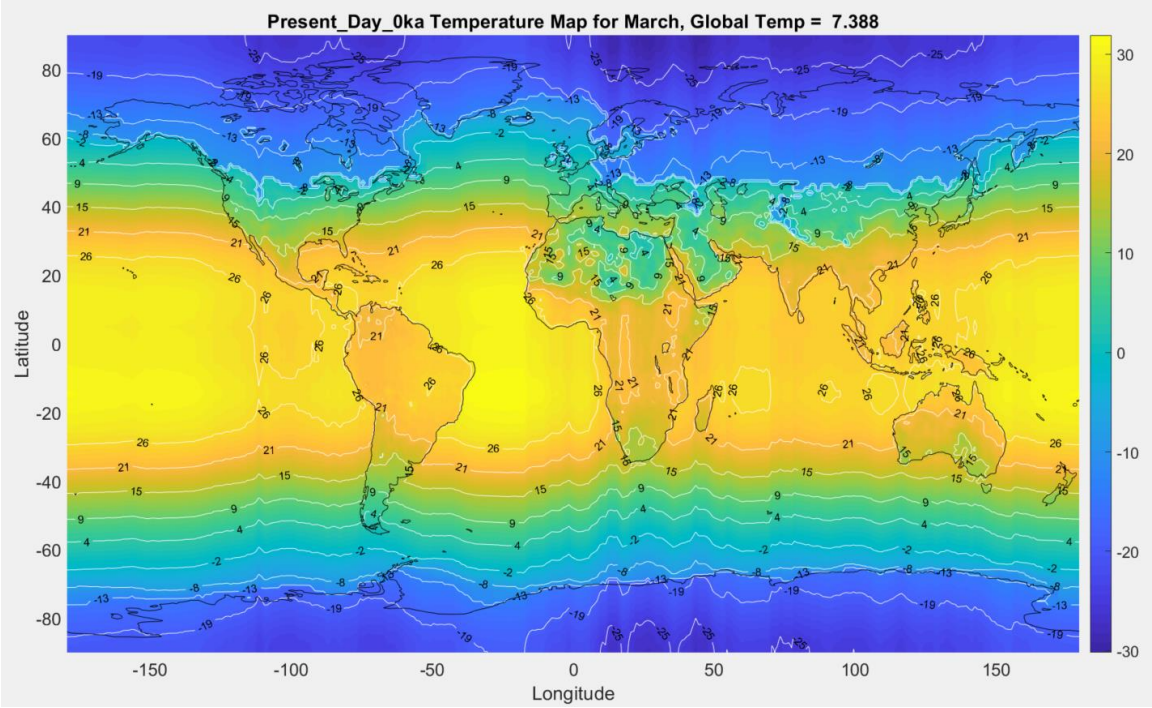
Present_Day_0ka Temperature Map for March, Global Temp = 7.388
Latitude
Longitude
80
60
40
20
0
-20
-40
-60
-80
-150
-100
-50
0
50
100
150
30
20
10
0
-10
-20
-30

b.

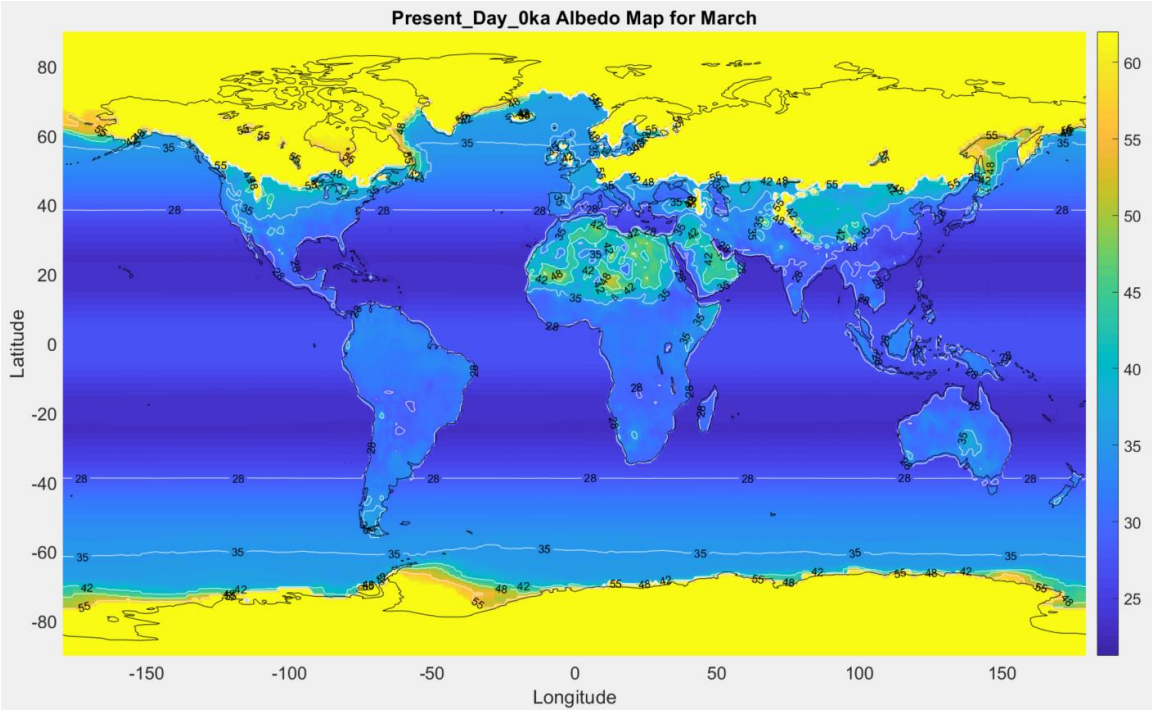
Present_Day_0ka Albedo Map for March
Latitude
Longitude
80
60
40
20
0
-20
-40
-60
-80
-150
-100
-50
0
50
100
150
60
55
50
45
40
35
30
25

c.

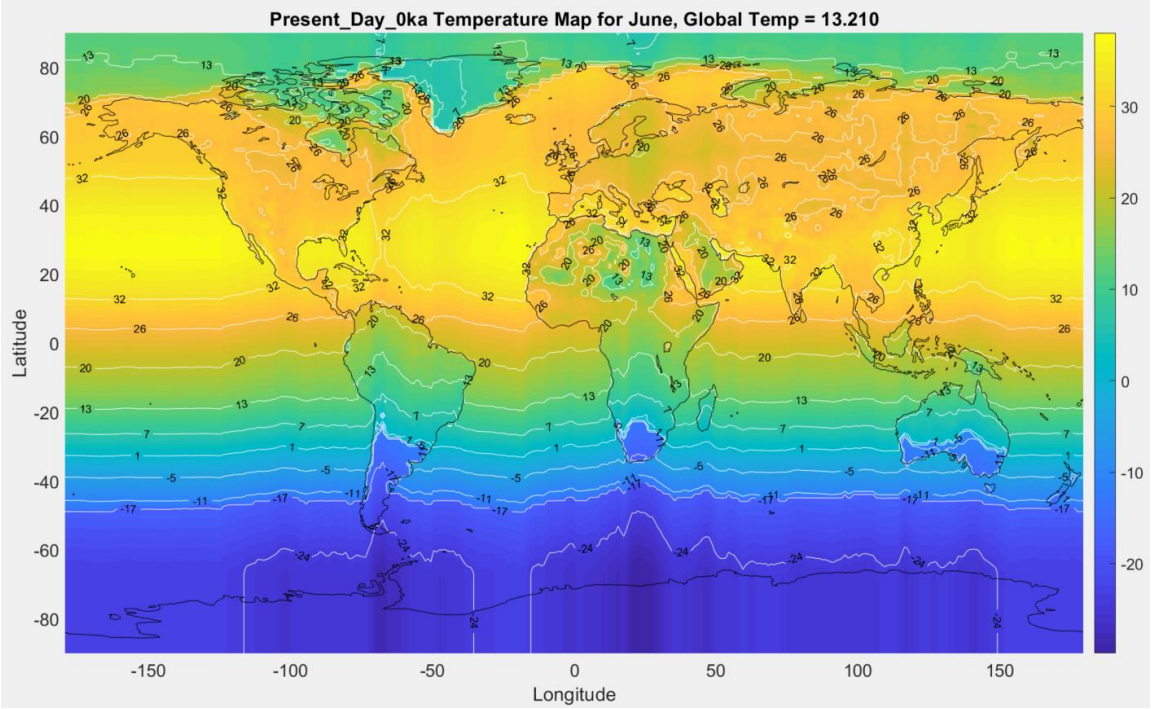
Present_Day_0ka Temperature Map for June, Global Temp = 13.210
Latitude
Longitude
80
60
40
20
0
-20
-40
-60
-80
-150
-100
-50
0
50
100
150
30
20
10
0
-10
-20

d.

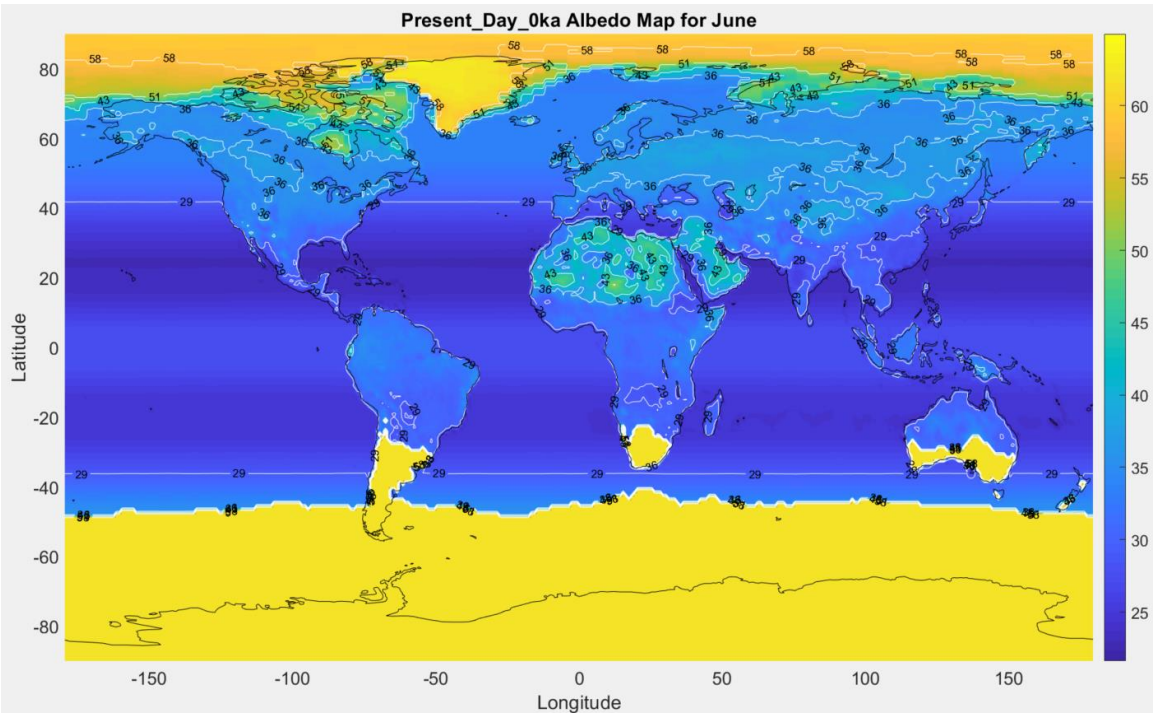
Present_Day_0ka Albedo Map for June
Latitude
Longitude
80
60
40
20
0
-20
-40
-60
-80
-150
-100
-50
0
50
100
150
60
55
50
45
40
35
30
25

e.

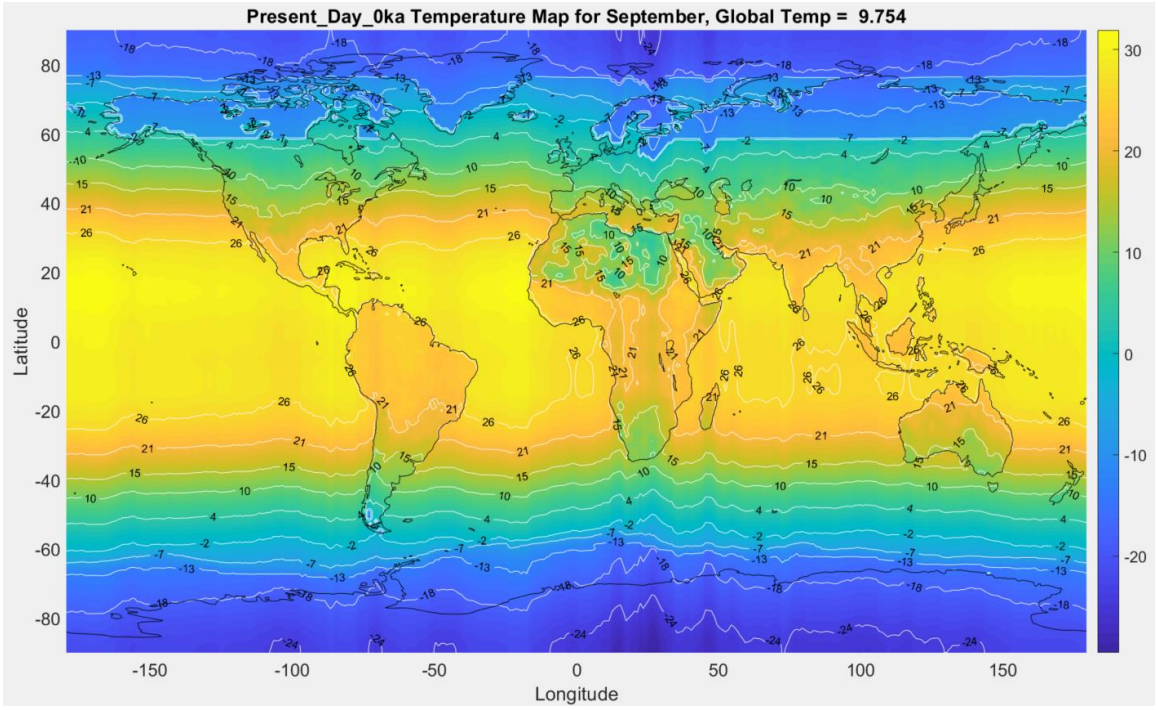
Present_Day_0ka Temperature Map for September, Global Temp = 9.754
Latitude
Longitude
80
60
40
20
0
-20
-40
-60
-80
-150
-100
-50
0
50
100
150
30
20
10
0
-10
-20

f.

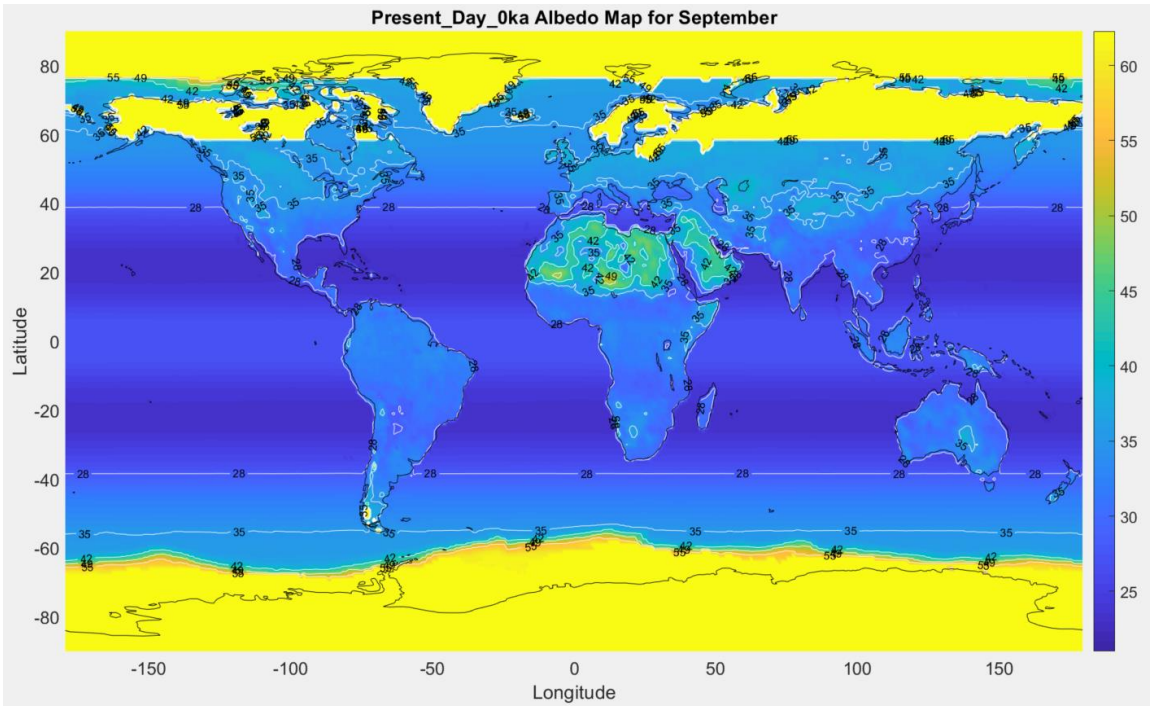
Present_Day_0ka Albedo Map for September
Latitude
Longitude
80
60
40
20
0
-20
-40
-60
-80
-150
-100
-50
0
50
100
150
60
55
50
45
40
35
30
25

g.

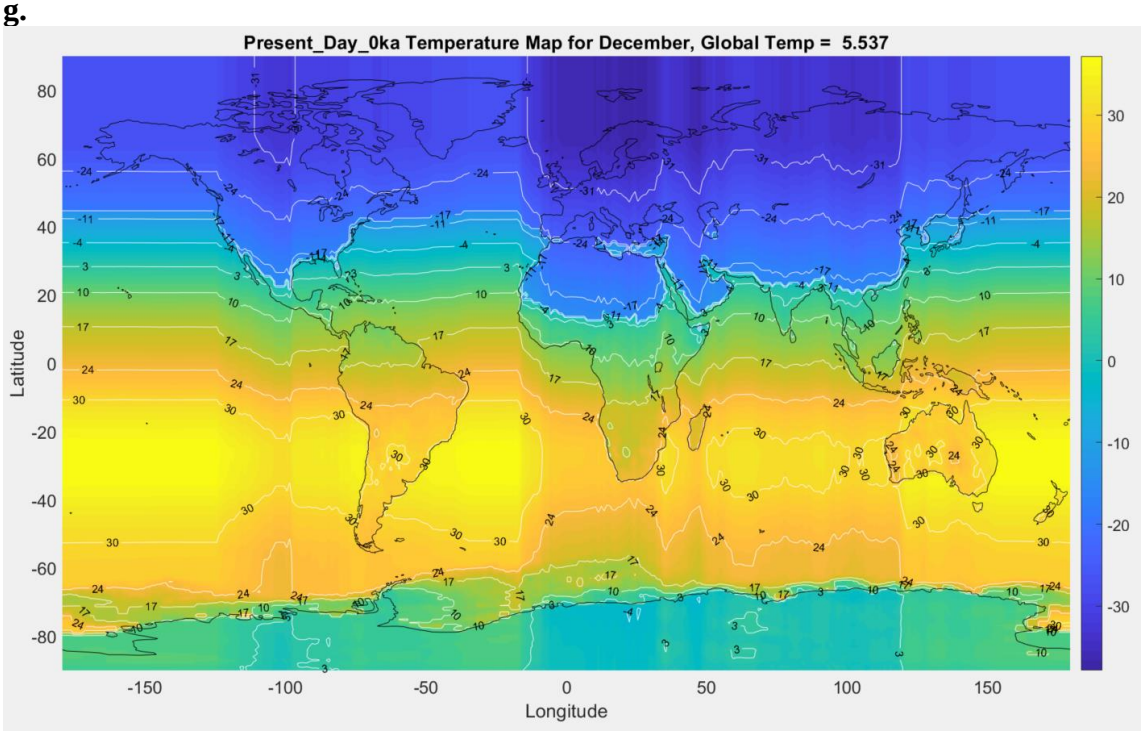

h.

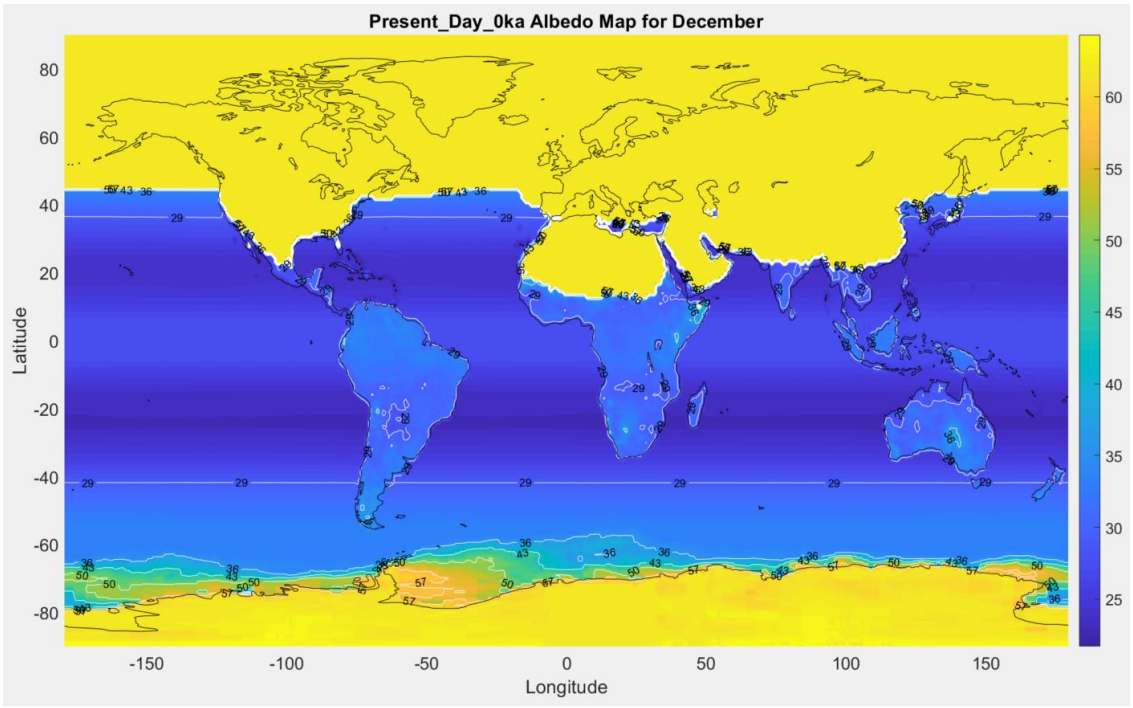

Figure 30: TwoD_CERES global temperature and albedo outputs for March (a, b), June (c, d), September (e,f), and December (g,h). Initial variables of α_{ice} = 0.62, CALB = 0.5, A = 204 W/m^2, B = 2.17 W/m^2°C, C = 3.81 Wm^{-2}/°C, Tcrit Land = 0°C, and Tcrit Ocean = -13°C

CHAPTER 5: DISCUSSION

The EBM provides the basic framework for introducing, for example, dynamical insolation changes. The next step would to use the output albedos and temperatures, such as those displayed in **Figure 30,** as the inputs for successive time steps. This revived method of modeling the energy balance of Earth allows for instructive steps into more specific questions about complex systems which, due to excessive computational demands, cannot realistically be carried out with complicated global circulation models. For example, one might start with a March input albedo map, and produce a first output with March insolation; then use that output as the input albedo for April, etc. for all twelve months would produce an informative time-variable insolation case study to compare with current month by month results. A second twelve-month case study, beginning with September could test for the importance of a climate's history and model replication of seasonal cycles.

This EBM can also be adapted for use in modeling exoplanets, and other Earth-like planets in our Solar System. The inclusion of time-variable insolation throughout repeating model runs, using previous outputs as input values, would allow for a unique look at the change in climates based on continuous insolation values over time. Would this do something unexpected to the EBM?

It will be instructive to use the EBM in this way for paleoclimate modeling. It has been designed primarily for use with Earth, but assuming that it functions well, changes in orbital forcing for example, could be applied the same way to examine a warm and wet

paleo-Mars. The large changes to orbital parameters in a complex orbit such as Pluto over time could also lead to interesting results in a time-variable insolation run.

These tests also help determine the functionality of sixth degree Legendre approximations over various orbital situations. Modeling Mars' chaotic obliquity shifts over automatic successive runs could produce unique results. At a minimum, designing choices to move forward with 0D, 1D, and q2D EBM's based on available input data would significantly improve accessibility of the model for use on planets with less known parameter information. As such, it could prove to be an invaluable tool for adaptive and dynamic modeling of exoplanet climates as information improves. North and Kim (2017) believe that energy balance modeling could experience a resurgence of sorts for use with exoplanets. 0D models would be especially useful, as most exoplanetary data is limited to a single-body format.

5.1: Hysteresis response

Corroboration of the relationship between temperature and the fraction of solar flux is produced in **Figure 31**, showing the sharp decline in global temperatures at ~0.83 S_x (S/S_o in **Figure 31**) due to the runaway feedback glaciation from point A to point B as discussed in Section 4.2 (**Figs 25-27**). Temperatures remain on this colder path even when S_x is increased again, until reaching point C, which is far above the present solar constant value (McGuffie and Henderson-Sellers, 2014).

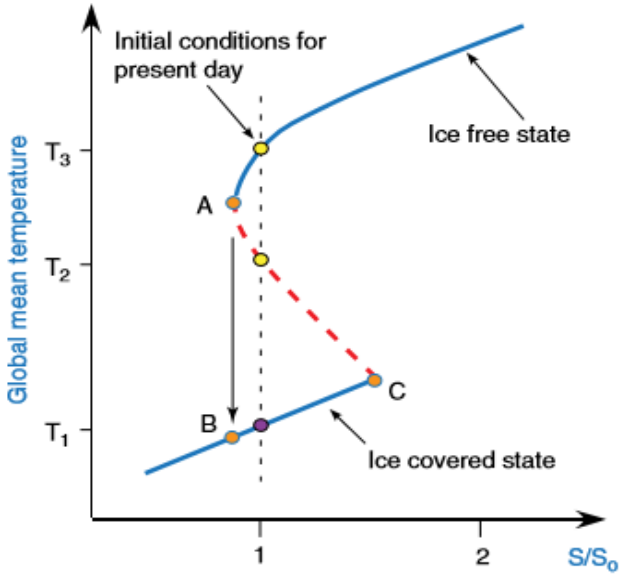

Figure 31: Global mean temperature as a function of solar fraction (Figure 3.7 from McGuffie and Henderson-Sellers, 2014)

This is because Earth's global temperature exhibits a hysteresis response for increasing versus decreasing solar radiation forcing that is dependent on the history of the climate system, not simply the governing parameters. The basic 1D-EBM shows that as solar radiation is decreased from 1.5 times present-day value, temperature decreases linearly and then at 0.83 times present-day value suddenly drops to "snowball earth" conditions (**Figure 32a**). As solar radiation is increased from 0.5 times present-day value, for which the system represents a "snowball earth", it will remain ice covered until solar radiation reaches 1.2 times present-day value, at which time global temperatures increase sufficiently to cause ice to melt (**Figure 32b**). Depending on where the system has been, i.e. past history, it follows different evolutionary paths, in a pattern known as a hysteresis loop.

For present-day TOA insolation of 1361 W/m^2, there can be two very different temperature values depending on which side of the hysteresis loop the system is on, i.e., it does not represent a unique temperature value of expected present-day temperature (~14°C). If the system is emerging from a global glaciation, present-day insolation would heat the Earth up only to approximately -30°C; insolation would need to be 1.2 times present-day value to initiate ice melt. This is due to the global presence of ice and its albedo, which reflects a majority of the insolation, preventing the Earth from heating up until the fraction of insolation that is not reflected (i.e., is absorbed) equals or exceeds the amount needed to increase temperature from its previous value to exceed Tcrit. On the other hand, starting in a global system without polar icecaps, it is more difficult to glaciate the Earth. With steady cooling, temperature maintains a steady decrease, but the ice line does not advance correspondingly. Albedo only becomes a powerful enough factor once it reaches a critical point at 0.83 times present day insolation and enough ice can form to counteract melting.

a.

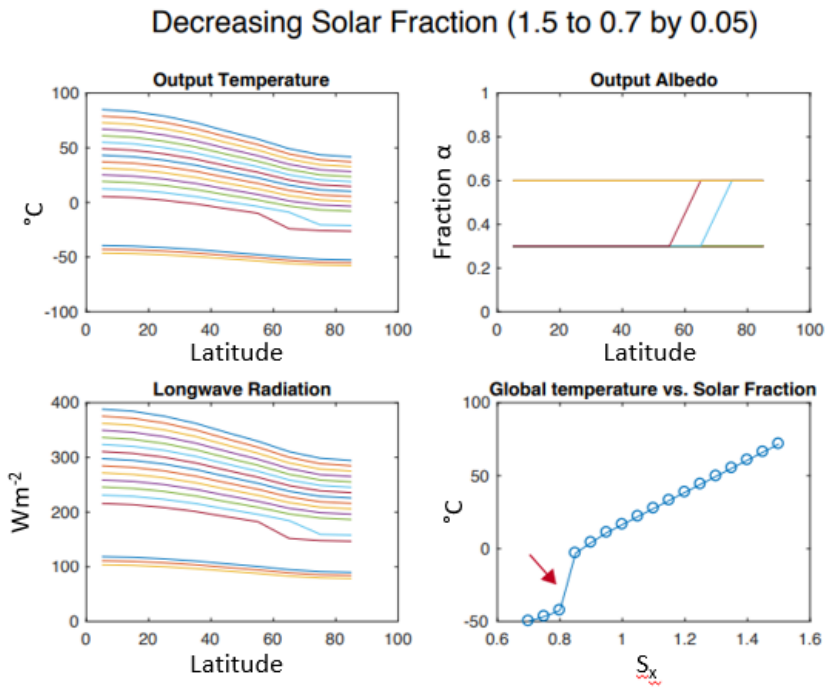

b.

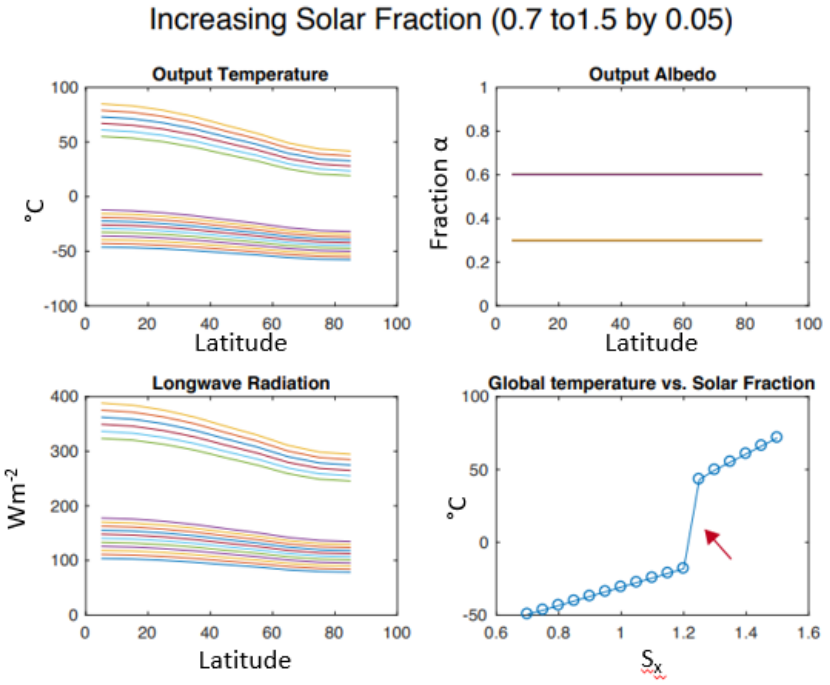

Figure 32: Climate hysteresis demonstrated in a basic 1D-EBM that incorporates the original basic parameters only: incoming solar radiation, albedo, latitudinal

heat transport and outgoing longwave radiation. a. decreasing solar fraction. b. increasing solar fraction. For both a. and b., upper left represents the model's output temperature, upper right the output albedo, lower left the longwave radiation, and lower right the global temperature versus the solar fraction. The red arrows point to times of abrupt shift.

The discovery of the Earth's hysteresis response can be traced to Budyko (1969). He argued that for the existing distribution of continental land masses, two climatic regimes could result, one in which polar ice contrasts greatly with a much warmer equator, and another where no glaciation and low meridional temperature gradients prevail. Small changes in incoming solar radiation would be enough to tip these unstable regimes towards freezing ice-free poles, or conversely, melting polar ice. He does not directly imply the importance of the history of the system, but does indicate that this effect could have major implications for the glacial-interglacial cycles of the Quaternary Period.

5.2: Present-day global temperature (Jones) vs. 2D-EBM temperature

Figure 33 shows average mid-season temperatures (Jones et al., 1999, Plate 4) that can be compared to the model outputs.

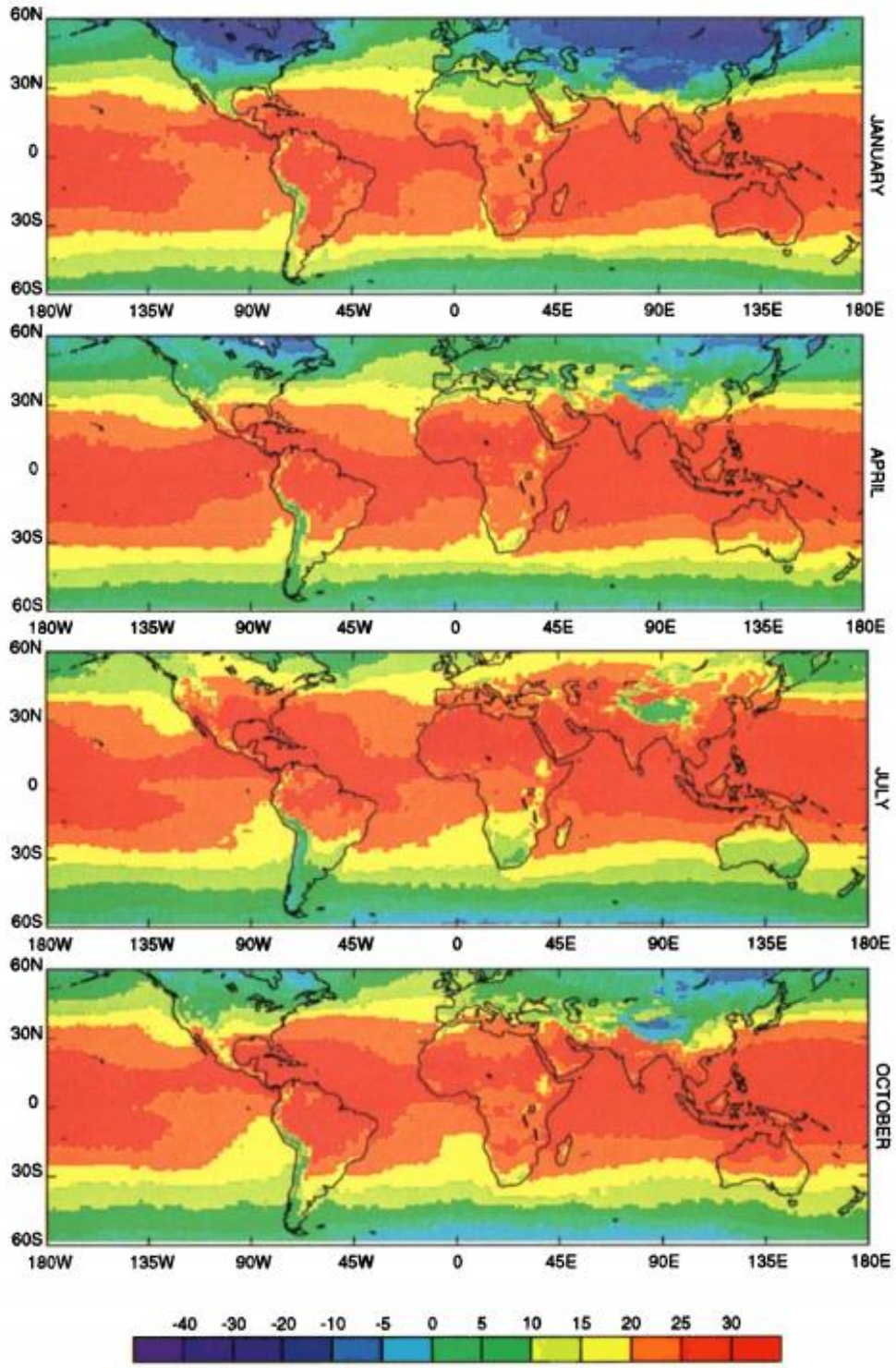

Figure 33: Average air temperature for midseason months of January, April, July, and October from 1961-1990 between 60°S - 60°N (Jones et al, 1999, Plate 4).

The months in **Figure 33** are offset forward by one compared to the chosen midseason months discussed in this thesis. TwoD_CERES model outputs are slightly cooler, but comparable to the annual global average of 14°C (July maximum of 15.9°C and January minimum of 12.2°C.). These observational data are consistent with a global climate model by Hansen et al. (2010) that was also used for evaluation of TwoD model outputs. Comparing to **Figure 33**'s January, TwoD_CERES December has the ITCZ properly situated at 23°S, moved northward in **Figure 33**, so a direct comparison cannot be made. However, using the maximum value of 30°C, both Jones et al. (1999) and TwoD_CERES, the model produces near consistent temperatures with the Jones observations.

5.3: Comparison of 0 ka, 24 ka and 128 ka time slices 2D EBM results

Changes in insolation between LGM and Eemian data reveals a difference of more than 7°C in the warmest locations for each hemisphere's summer (**Fig. 34**). Significant to note, is that for all three time slices, present day albedo and geography are used as the initial conditions of the EBM.

a.

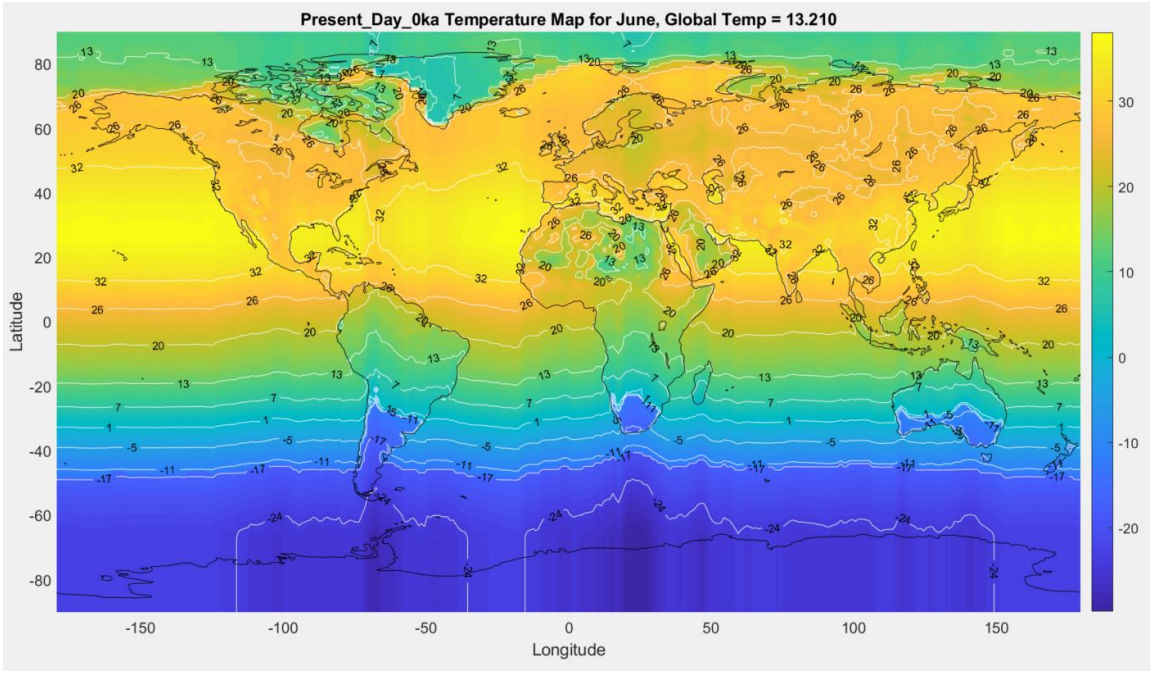
Present_Day_0ka Temperature Map for June, Global Temp = 13.210
Latitude
Longitude
80
60
40
20
0
-20
-40
-60
-80
-150
-100
-50
0
50
100
150
30
20
10
0
-10
-20

b.

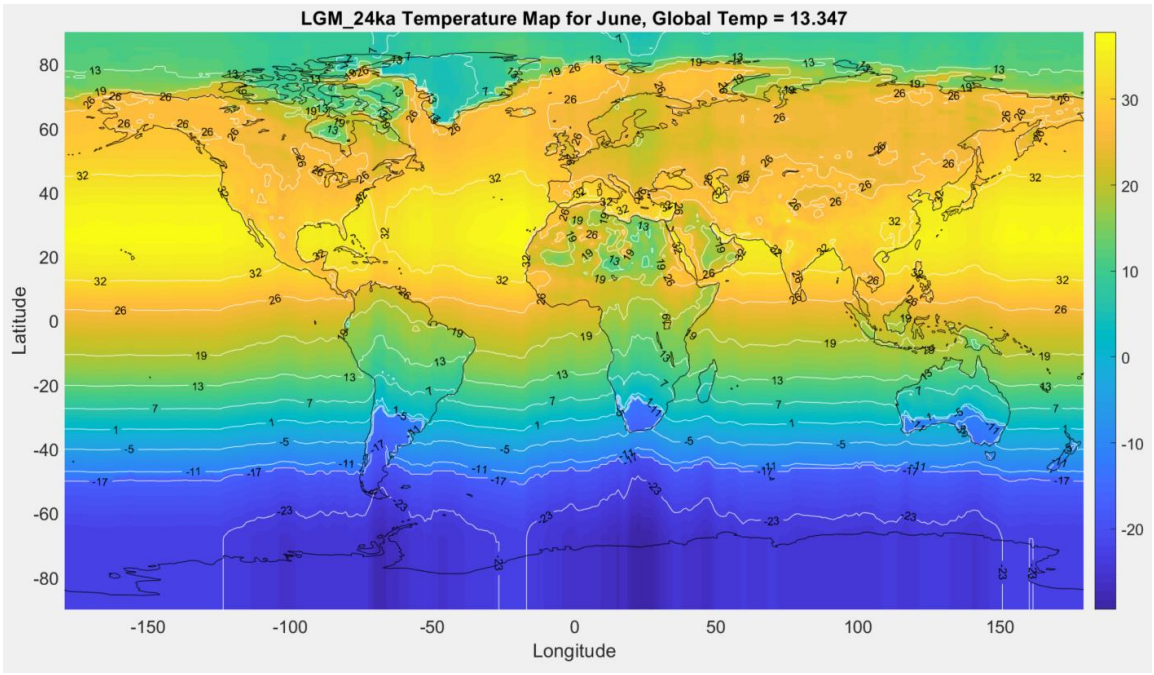
LGM_24ka Temperature Map for June, Global Temp = 13.347
Latitude
Longitude
80
60
40
20
0
-20
-40
-60
-80
-150
-100
-50
0
50
100
150
30
20
10
0
-10
-20

c.

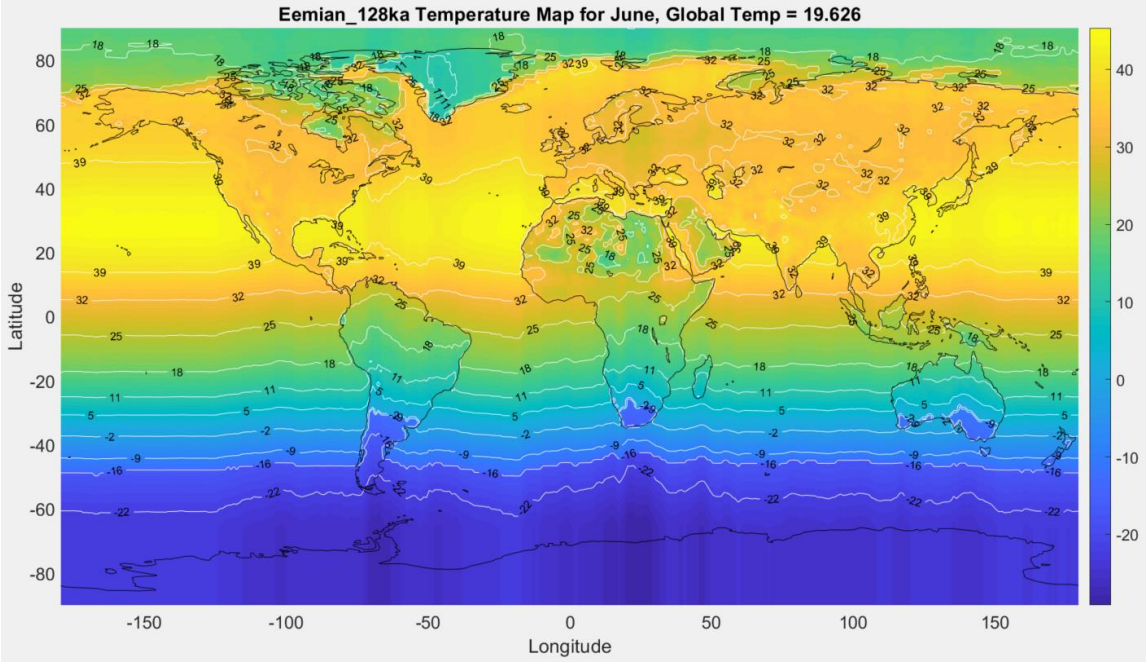

Figure 34: TwoD_CERES.m output temperature maps for June at 0ka (a), 24ka (b), and 128ka (c) insolation profiles. Initial variables of α_{ice} = 0.62, CALB = 0.5, A = 204 W/m^2, B = 2.17 W/m^2°C, C = 3.81 Wm^{-2}/°C, Tcrit Land = 0°C, and Tcrit Ocean = -13°C

The LGM produces warmer temperatures in December (**Figure 35**) than in the Eemian interglacial. One possible cause is the absence of circulation from the TwoD_CERES EBM. Circulation could divert the poleward transfer of heat, and thereby produce colder temperatures in Antarctica. The shifting zone of perpetual night, due to obliquity, and/or the "midnight sun" may also contribute to the differences. We see this inconsistency with the Eemian being colder in more southern regions than the LGM at winter solstice, but warmer overall, specifically in the summer, as Earth's tilt is pointed more directly towards the Sun (obliquity at 128ka = 24.17°, and 24ka = 22.52°, see **Table 2**). Another interesting output occurs in the December Eemian temperature map (**Figure 35c**). In the

temperature map, odd patterns of circular isoclines in the Indian Ocean, and deep southerly invasions of cold temperatures appear to originate from effects of land albedo in the Northern Hemisphere.

a.

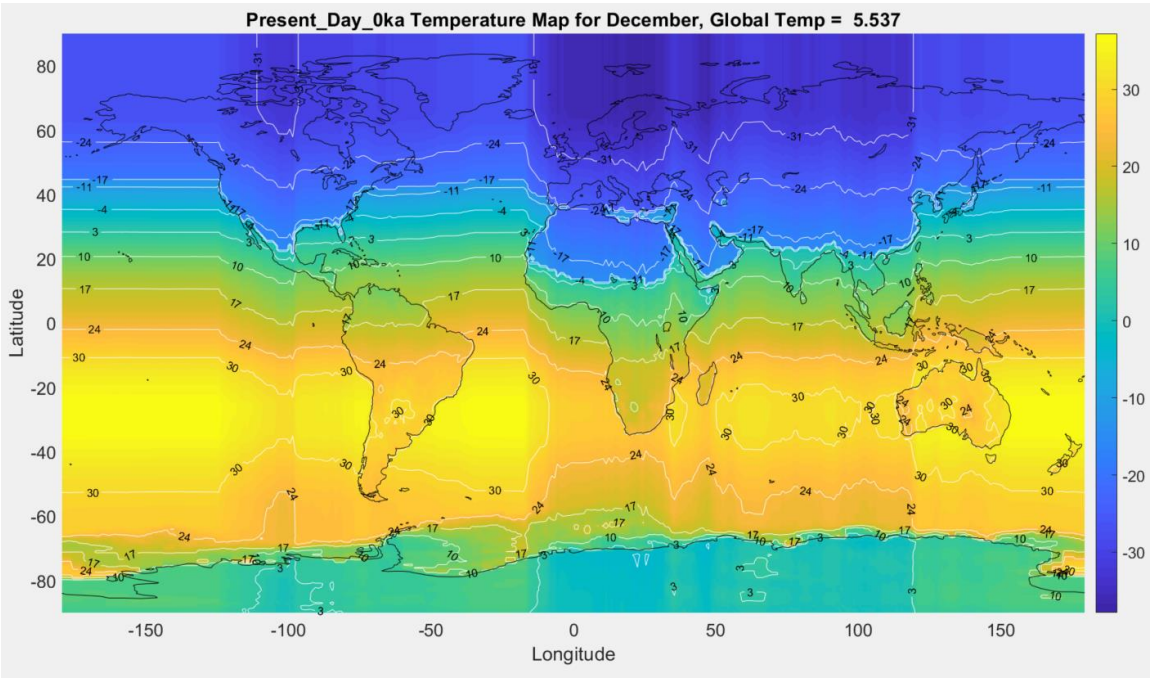

b.

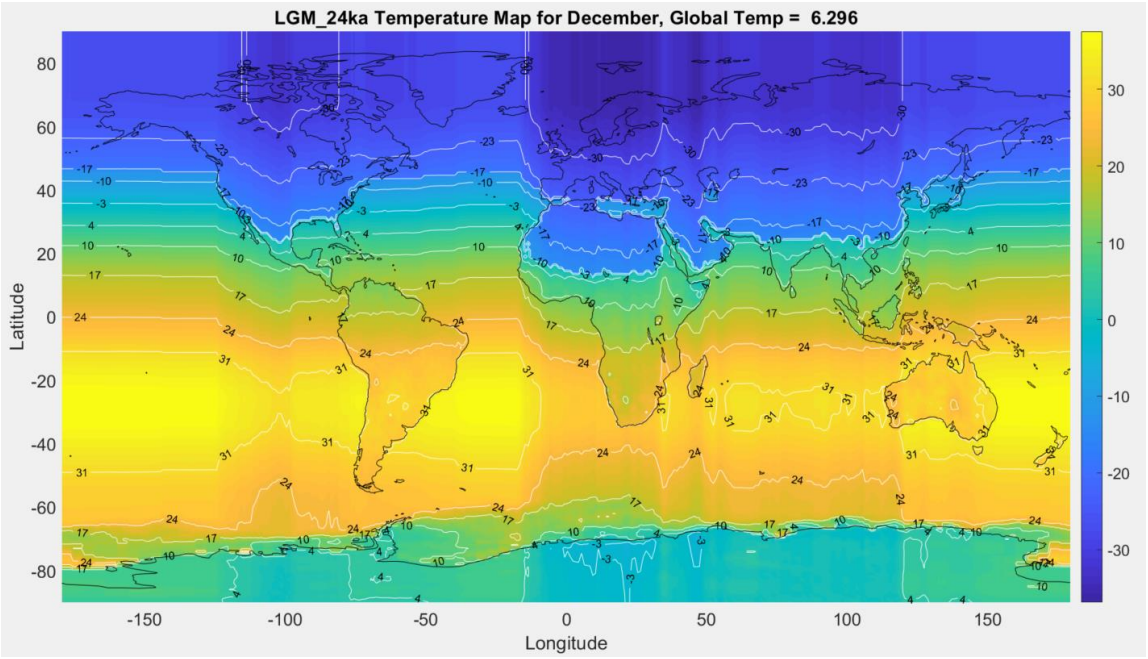

c.

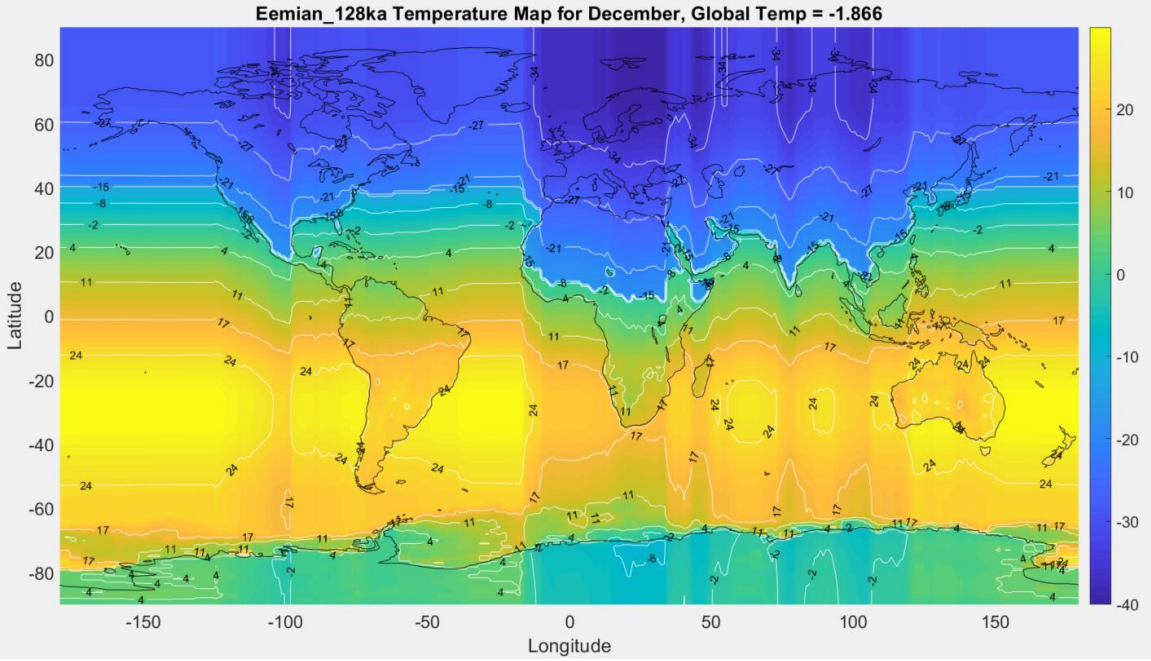

Figure 35: TwoD_CERES.m output temperature maps for December at 0ka (a), 24ka (b), and 128ka (c) insolation profiles. Initial variables of α_{ice} = 0.62, CALB = 0.5, A = 204, B = 2.17, C = 3.81, Tcrit Land = 0°C, and Tcrit Ocean = -13°C

Figure 36 shows temperature difference plots for LGM to present, and Eemian to present for both June and December outputs using the TwoD_CERES script. The sharpest differences such as those seen in **36a** occur at the ice line, where a large change in temperature occurs at the latitudes where the ice line is located in one time slice, but not in the other.

a

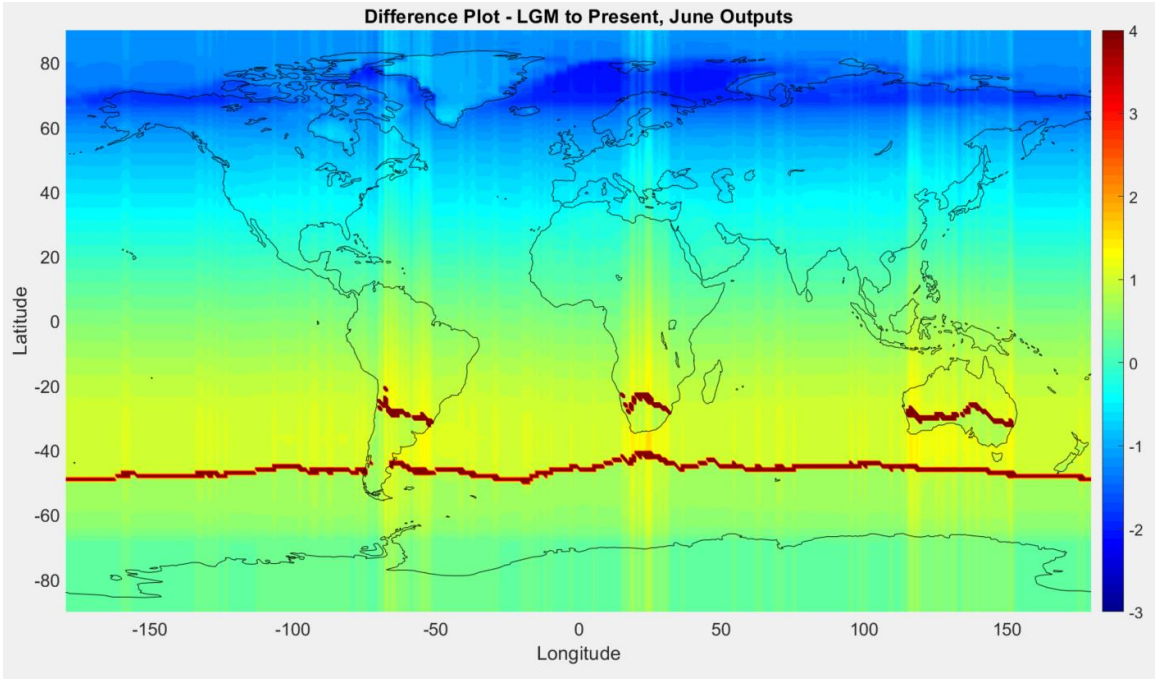
Difference Plot - LGM to Present, June Outputs
Latitude
Longitude
80
60
40
20
0
-20
-40
-60
-80
-150
-100
-50
0
50
100
150
4
3
2
1
0
-1
-2
-3

b

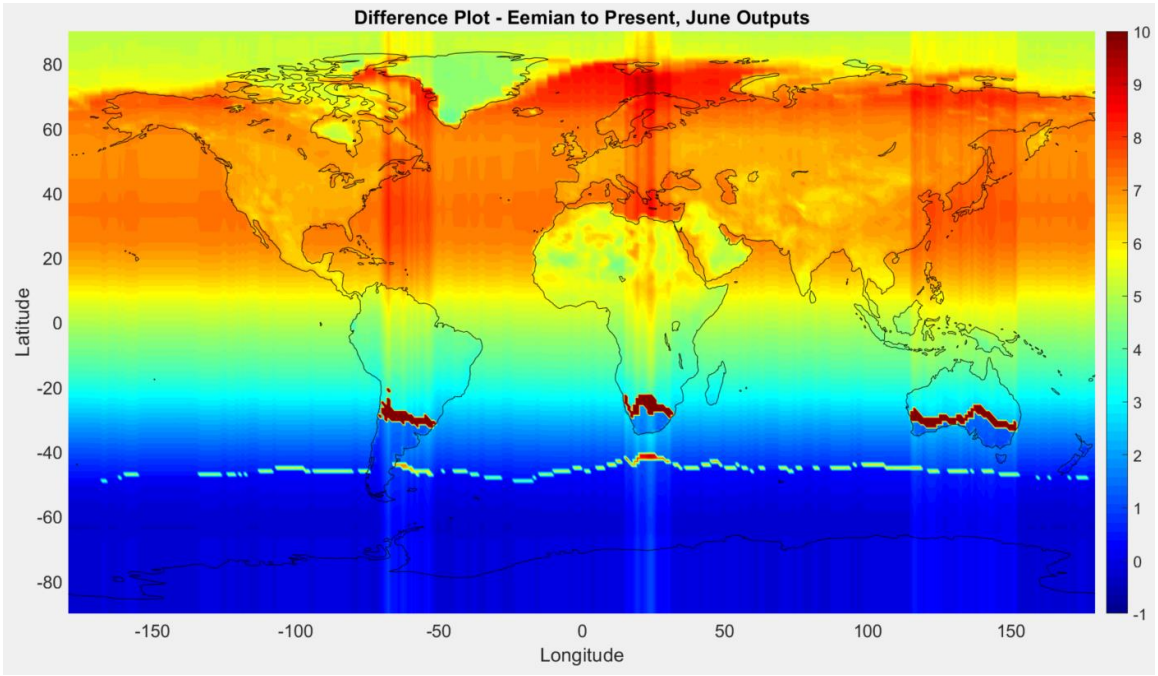
Difference Plot - Eemian to Present, June Outputs
Latitude
Longitude
80
60
40
20
0
-20
-40
-60
-80
-150
-100
-50
0
50
100
150
10
9
8
7
6
5
4
3
2
1
0
-1

c

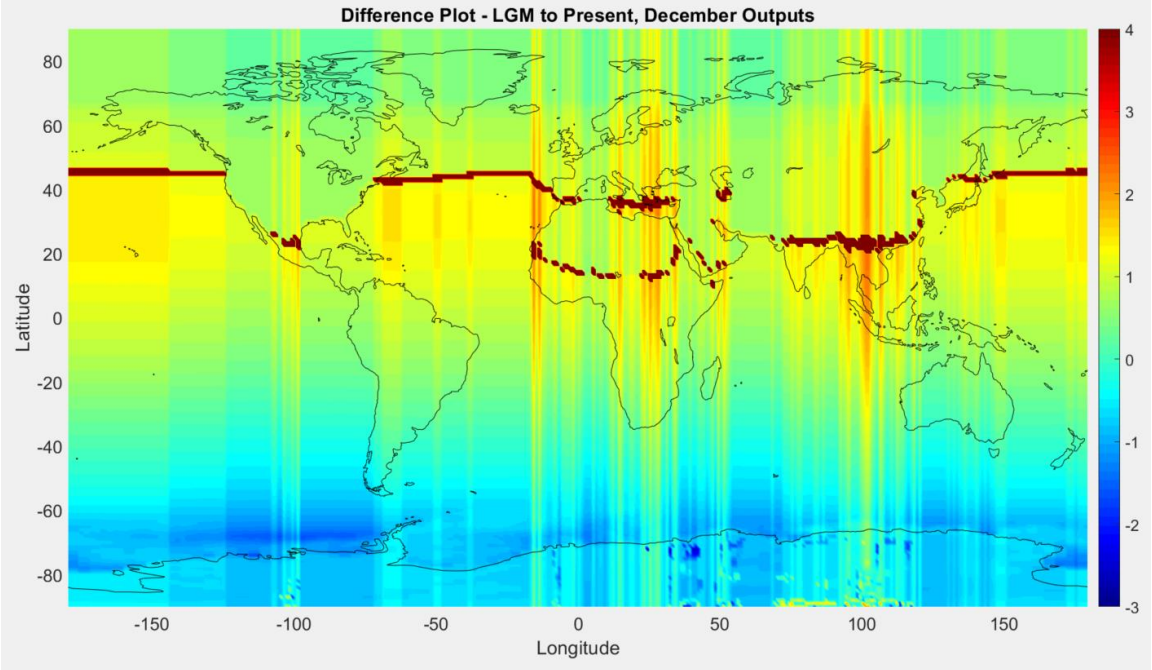

d

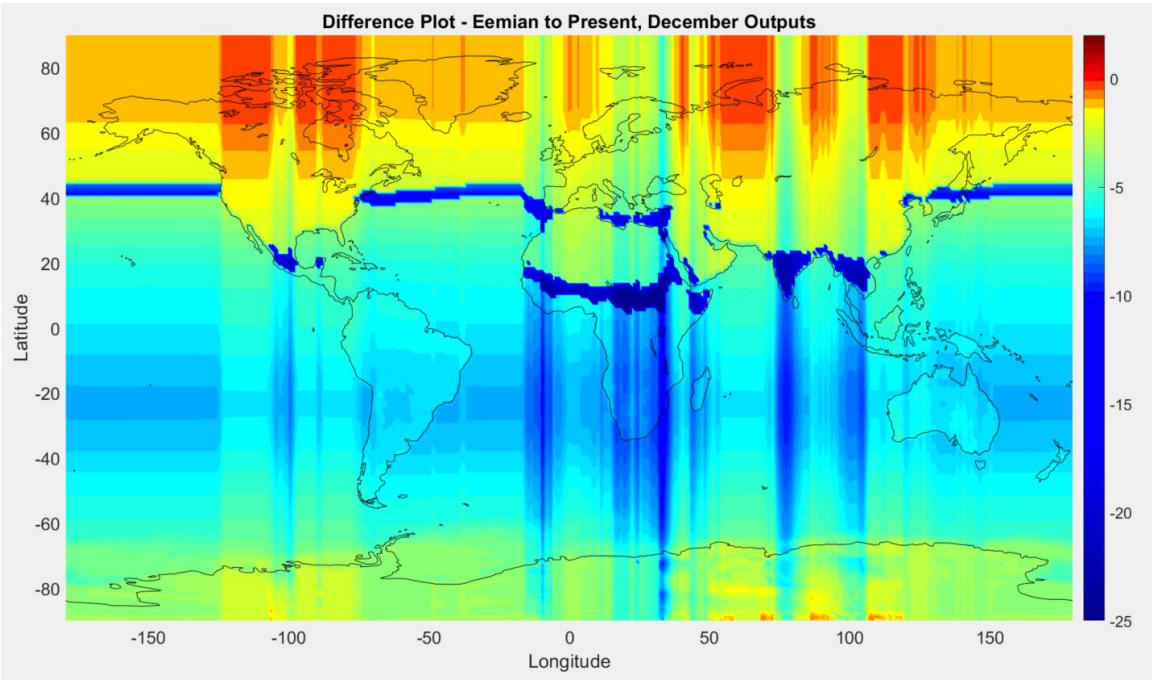

Figure 36: Difference plots between LGM and present day for June (a) and December (c), and Eemian and present day for June (b) and December (d) temperatures using the TwoD_CERES EBM. The color scale indicates difference in °C. The range is individualized for each month.

5.4: EBM parameter sensitivity

5.4.1: Starting temperatures

With limited parameterizations, simple experimentation to portray the effect that changing a specific parameter has on the Earth system can be carried out readily. **Figure 37** is one such example, where the impact of initial temperatures (TSTART) on climate outputs are examined.

Initial albedo plays a significant role in determining output temperatures, so a change in initial temperature was expected to be similarly impactful. However, when comparing realistic zonal temperatures to an initial temperature of 0°C across all latitudes, differences in output temperatures and albedos were minimal, resulting in only a ±0.3°C change across global mean temperature. Testing with initial temperatures set to 14°C across all latitudes produces nearly identical values to 0°C (12.130°C, **Figure 37b**), with global mean temperature reading 12.133°C. Setting initial temperatures to an extreme value, such as -100°C, will of course result in a larger impact, with the global mean temperature reaching -43.9°C, but this remains a small change comparatively to if initial surface or cloud albedo were changed to this extreme.

These tests indicate that using a simple near average global temperature across all latitudes rather than a hyper-realistic temperature for each zone of latitude results in comparable model outputs. Therefore, while a more realistic albedo may still be required, the model can simulate other planetary bodies without highly accurate zonal starting temperatures.

a.

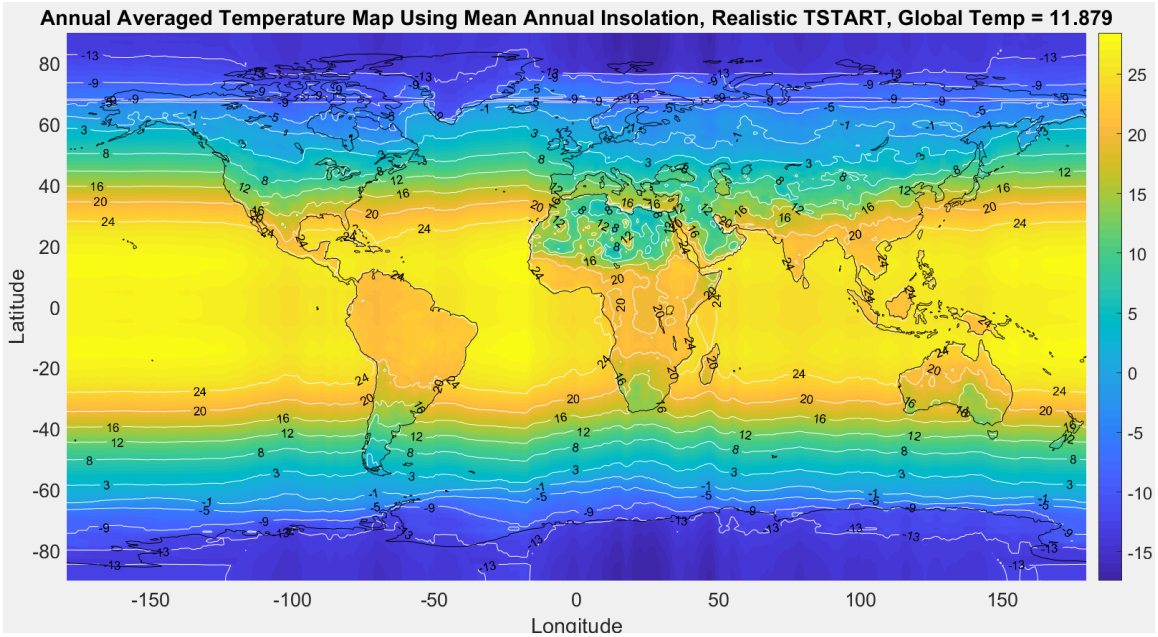

b.

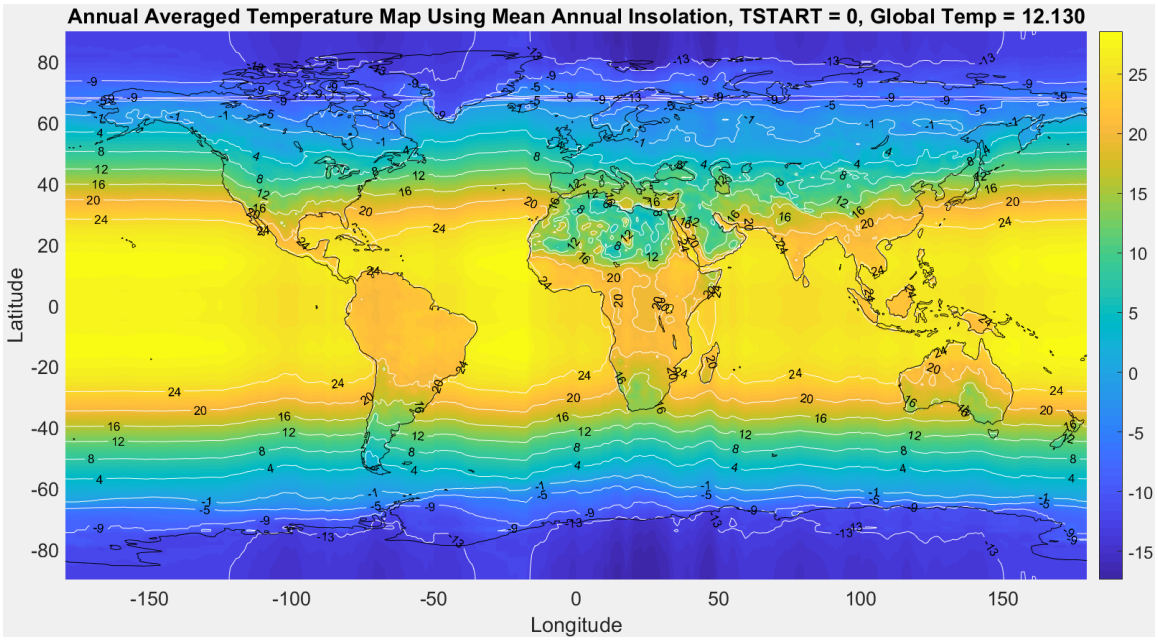

Figure 37: Global temperature maps for annual averaged CERES albedo using mean annual insolation for both a. realistic starting temperatures and b. 0°C starting temperatures for all zones of latitude.

5.4.2: Heat transport coefficient

Heat transport coefficient, C, influences the shape of the curve for the latitude of the ice-line as a function of input shortwave radiation, and global stability improves with a reduced meridional heat transport efficiency (Warren and Schneider, 1979). Global stability is defined by what fraction the solar constant must decrease in order to produce a snowball Earth (Lindzen and Farrell, 1977). It depends primarily on the values of B, C, and an albedo-temperature feedback coefficient (0.009 K^{-1}) (Sellers, 1969; Warren and Schneider, 1979). Global stability increases with reduced C because with less transport between neighboring zones, temperature (and affected, albedo) changes in one zone have less of an effect on others. In the case of zero heat transport, the albedo-temperature feedback would only occur withing that singular zone of latitude, and not impact the energy balance of other zones (Warren and Schneider, 1979).

5.4.3: Ice-albedo feedback

A Milankovitch-forced reduction in insolation triggers glacial advance, which then experiences ice-albedo feedback, enhancing the advance. As more ice covers the Earth, planetary albedo increases, reflecting more shortwave radiation out of the system, reducing heat in the Earth system. By contrast, when less ice covers the surface, Earth absorbs more solar energy, increasing temperatures. In both cases, this is a positive feedback, with more ice, Earth cools, and allows for the further advance of ice; with less ice, Earth heats up, causing ice to recede.

5.4.4: Milankovitch cycles

Milankovitch cycles can be used to gauge the global mean surface temperature (GMST) as a function of latitude and time, and the position of the ice line, in order to ascertain the inputs for an ice-albedo feedback model (McGehee and Lehman, 2012). GMST and the ice line location are more dependent on obliquity than eccentricity, and have no significant dependence on precession. Orbital eccentricity did have a substantial effect on GMST compared to ice volume, despite contributing less than obliquity. McGehee and Lehman's model, while accurately predicting the impact of Milankovitch cycles on the climate, otherwise shows a significant departure from observed climate, confirming that additional parameters beyond orbital parameters alone are needed to accurately model climate, but their inclusion improves the accuracy of said factors (McGehee and Lehman, 2012).

It should also be noted that the McGehee and Lehman model was able to more accurately represent climate for the early Pliocene, than for the late Pleistocene, where it had substantial difficulty due to factors other than ice-albedo feedback from Milankovitch cycles being more significant. Their model could not replicate the large 100,000 year glacial-interglacial cycles present during the time of the late Pleistocene. Ice-albedo feedback, while present, was not a dominant factor during near global glacial cycles of the Pleistocene. Yet, it was much more dominant during the early Pliocene when ice was predominantly in the Antarctic (McGehee and Lehman, 2012). The EBM models provided by this thesis replicate the influence of these orbital parameters, using

the input variables of obliquity and orbital eccentricity at the three time slices and through the editable input boxes in the GUI's.

5.4.5: Cloud albedo, critical temperature, and albedo of ice.

As with initial surface albedo, cloud albedo (CALB) significantly impacts the model output temperatures and albedo. Lowering CALB to 0.3, from 0.5, and changing no other parameters results in unrealistic warming (**Figure 38**) in comparison to **Figure 34a** (June, 0ka) which indicates a global temperature of 13.21°C and has an ice-line latitude in the Southern Hemisphere that extends much further northward.

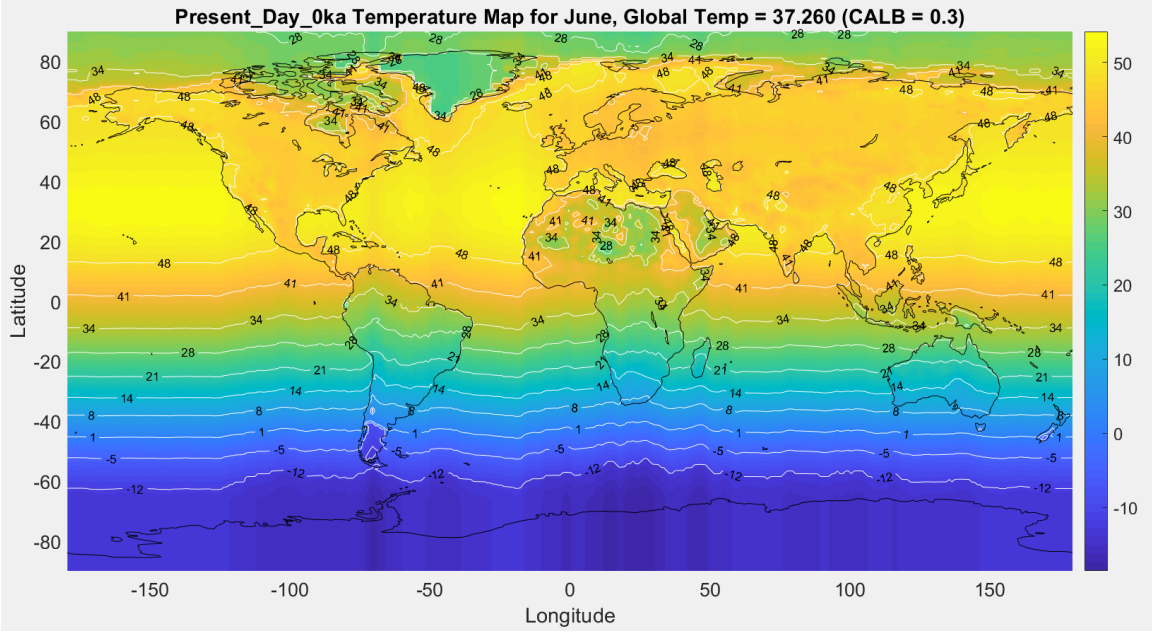

Figure 38: TwoD CERES temperature output map for present-day June, CALB = 0.3 instead of the default 0.5.

Changing other parameters, such as Tcrit results in significantly smaller variations. For example, setting Tcrit of land to -10°C (default = 0°C) outputs a global temperature of

13.81°C, a difference of only 0.5°C from default present day June output (**Figure 34a**). Setting Tcrit of the ocean to 0°C results in a global temperature of 9.278°C with Antarctic ice expanding to 30°S. Finally, a small change to α_{ice} from 0.62 to 0.7 results in **Figure 39**, global temperature drops to 7.483°C, and both ice sheets expand significantly.

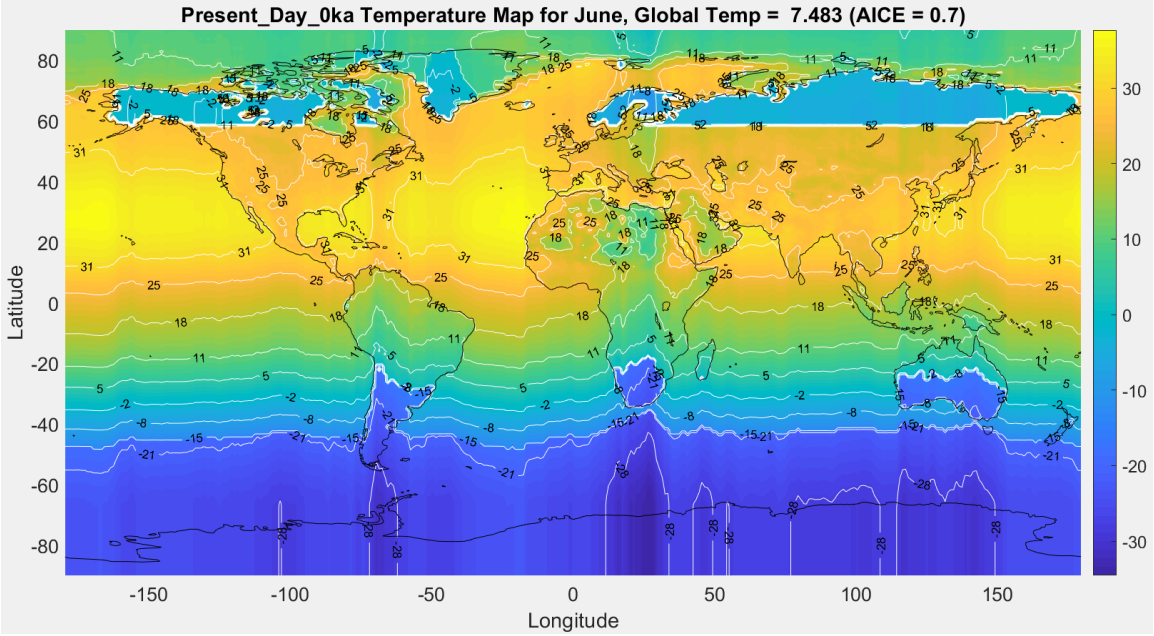

Figure 39: TwoD CERES temperature output map for present-day June, α_{ice} = 0.7 instead of the 0.62 default.

5.5: Mars

Here, preliminary discussion for Mars inputs is presented, confirming the critical importance of an accurate input albedo and OLR parameters A and B. While starting temperature (T_{Start}) is not as critical as albedo, it is set to the Martian global surface average temperature of -63°C.

With a significantly lower S of 586.2 W/m^2 (Q=S/4=146.55 W/m^2), surface temperatures on Mars are drastically lower than on Earth, to the point that both the critical temperatures of CO_2-ice and water-ice need to be accounted for. The critical freezing temperature of CO_2 at 6 mbar of pressure (the surface atmospheric pressure of Mars) is -123°C (Longhi, 2006), which is much lower than for water ice at -3°C. Mars surface pressure (P_{air}) fluctuates between 4.0 and 8.7 mbar, and is currently 6.36 mbar (NASA, 2016). The average surface temperature on Mars is -63°C (210 K), but winter temperatures at the South Pole can reach <134 K, or -139°C (Longhi, 2006). The southern ice cap is the only location where solid CO_2 ice (dry ice) can form, however, mixtures of CO_2 and H_2O, CO_2 clathrate (hydrate), and other eutectic mixtures between H_2O and CO_2 can form at higher temperatures and latitudes (Longhi, 2006). The differences of albedo of ice for water (α_{ice} = 0.62) and CO_2 (α_{ice} = 0.64) (Hoffert et al., 1981) in the visible band of the spectrum should not be significant, although further testing will have to be done for differences, for example, in the infrared. There is also not enough water-ice to cause significant melting or recharge of the Martian ice caps (Longhi, 2006). **Figure 40** shows the phase diagram of the CO_2-H_2O system in the Martian ice caps.

As illustrated by the differences between Earth's 'Zres' and 'CERES' initial albedo maps, to accurately model a planet in TwoD, a high-resolution albedo input map is required. For Mars, this was accomplished using the Mars Global Surveyor Thermal Emission Spectrometer (MGS TES) Global Bolometric Albedo Map which resolves Lambert albedo values at 7410m/pixel, or 8 pixels/degree (Christensen et al., 2001). This

map was downscaled to 1° x 1° resolution in order to achieve the same resolution used for Earth modeling (**Figure 41).**

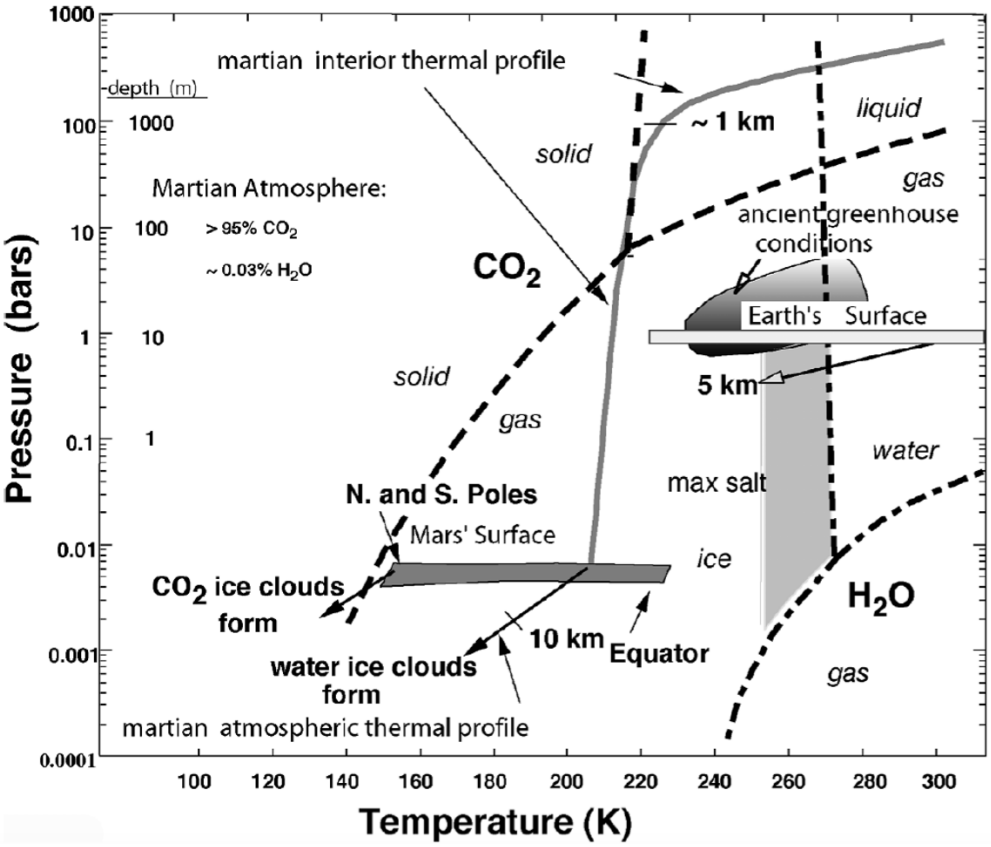

Figure 40: Mars' pressure-temperature phase profiles of H_2O (dash-dotted) and CO_2 (dashed) for Mars' current atmosphere, surface, and regolith (Fig. 1 of Longhi, 2006).

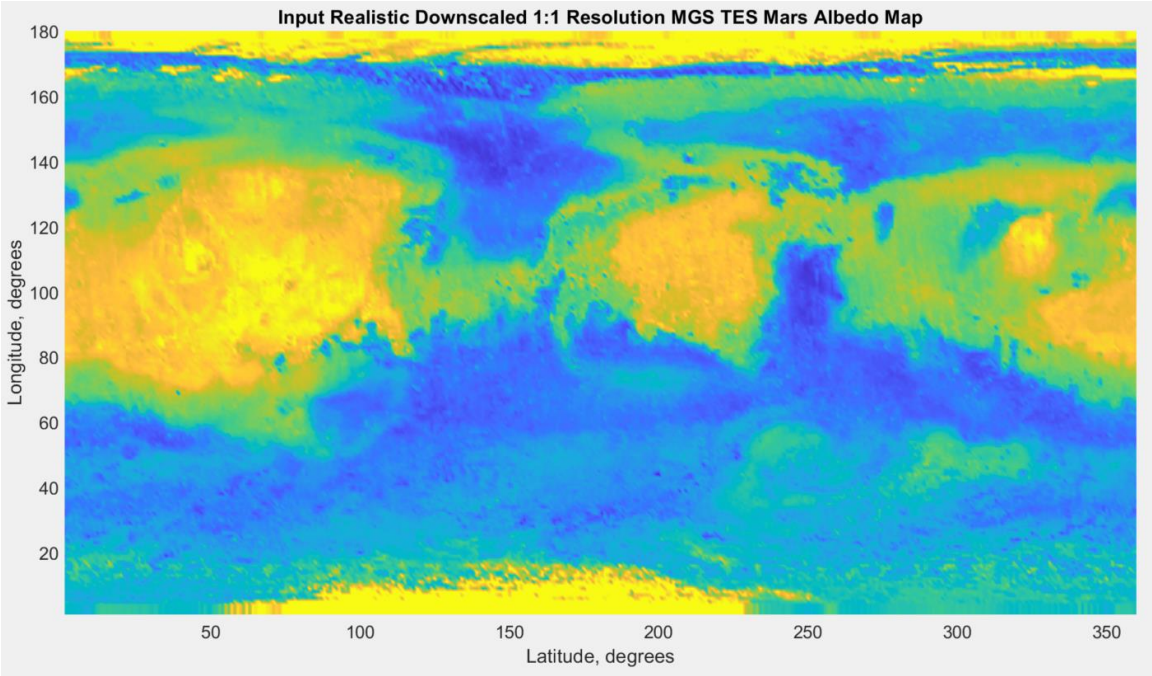

Figure 41: Input realistic downscaled 1º x 1º resolution MGS TES Mars albedo map

Table 5: A and B values for Mars (Nakamura and Tajika, 2001)

	$T_0 = 230.1$ K			
i	$a_i(A_1)$	$a_i(A_2)$	$b_i(B_1)$	$b_i(B_2)$
1	0.6449	0.1068	−0.003256	−0.00094
2	13.28	2.198	−0.06758	−0.0195
3	99.54	16.48	−0.5069	−0.1464
4	329.9	54.64	−1.68	−0.485
5	−372.7	−61.72	1.898	0.5479

On Mars, outgoing longwave radiation coefficient values A and B depend on the atmospheric pressure of CO_2 (Nakamura and Tajika, 2001). These coefficients were determined from radiative-convective calculations of Pollack et al. (1987), which include the greenhouse effects of CO_2 and H_2O. A and B are parameterized as a function of ρ:

Equation 18: $\boldsymbol{\rho = \log P_{air}}$

Where the surface pressure of CO_2, P_{air}, is in bars, and A_1/B_1 and A_2/B_2 are interchanged for $T > T_0$ (A_1/B_1) and $T < T_0$ (A_2/B_2) as used in **Equation 19**, which is reminiscent of **Equation 2**. T_0 is set equal to 230.1 K:

Equation 19: $\boldsymbol{I(\sin\theta) = A + BT(\sin\theta)}$

$$A = a_1\rho^4 + a_2\rho^3 + a_3\rho^2 + a_4\rho + a_5 \text{ (W/m}^2\text{)}$$

$$B = b_1\rho^4 + b_2\rho^3 + b_3\rho^2 + b_4\rho + b_5 \text{ (W/m}^2\text{K)}$$

Where $\boldsymbol{\theta}$ is latitude.

Mars's obliquity ranges from approximately 15° to 47.5° (Laskar et al., 2004b), and is currently 25.19° (NASA, 2016). Mars's orbital eccentricity is currently 0.09341233 (NASA, 2016), with a minimum of 0.00113993 and maximum of 0.1230998. Mars's obliquity and orbital eccentricity variations for 0-10 Ma are displayed in **Figure 42**. The large shift in obliquity at 5 Ma is due to Mars's chaotic obliquity and its modeled passage through a secular spin-orbit resonance (Touma and Wisdom, 1993).

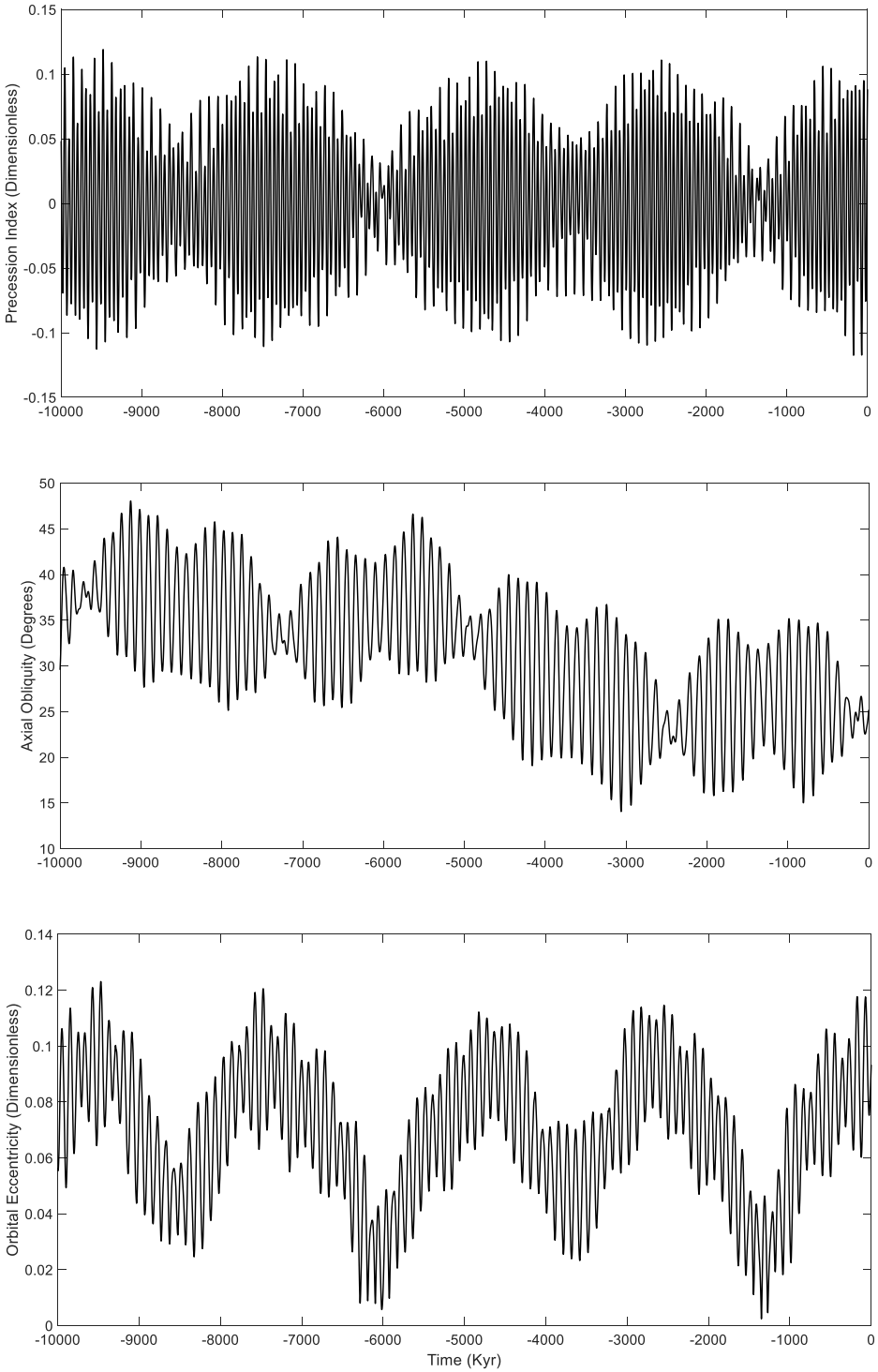

Figure 42: Mars' astronomical parameters according to the La2004 astronomical solution (Laskar et al., 2004b). Precession index (top), axial obliquity (middle), and orbital eccentricity (bottom), from -10 myr to present.

Using MGS TES albedo as an input, and Nadeau mean annual insolation for Mars at present day obliquity and orbital eccentricity produces the output global temperature and albedo displayed in **Figure 44.** Using the A and B values of Nakamura and Tajika (2001) with this first attempt at transitioning the Earth EBM results in temperatures that are far too warm for Mars. In **Figure 44**, parameters A, B, and C were therefore cherry-picked through model run testing to resemble observed Martian temperatures (**Figure 43**). More accurate outputs using the A and B values of Nakamura and Tajika (2001) would likely result if other parameterizations, such as the ability to swap A_1/B_1 with A_2/B_2 values at T_0 were introduced. Changes to CALB, C, cross-longitudinal heat transport, as well as latitudinal cloud fraction would also improve polar region outputs to be cold enough to produce CO_2 ice using **Table 5**'s parameterizations, while keeping equatorial regions warmer.

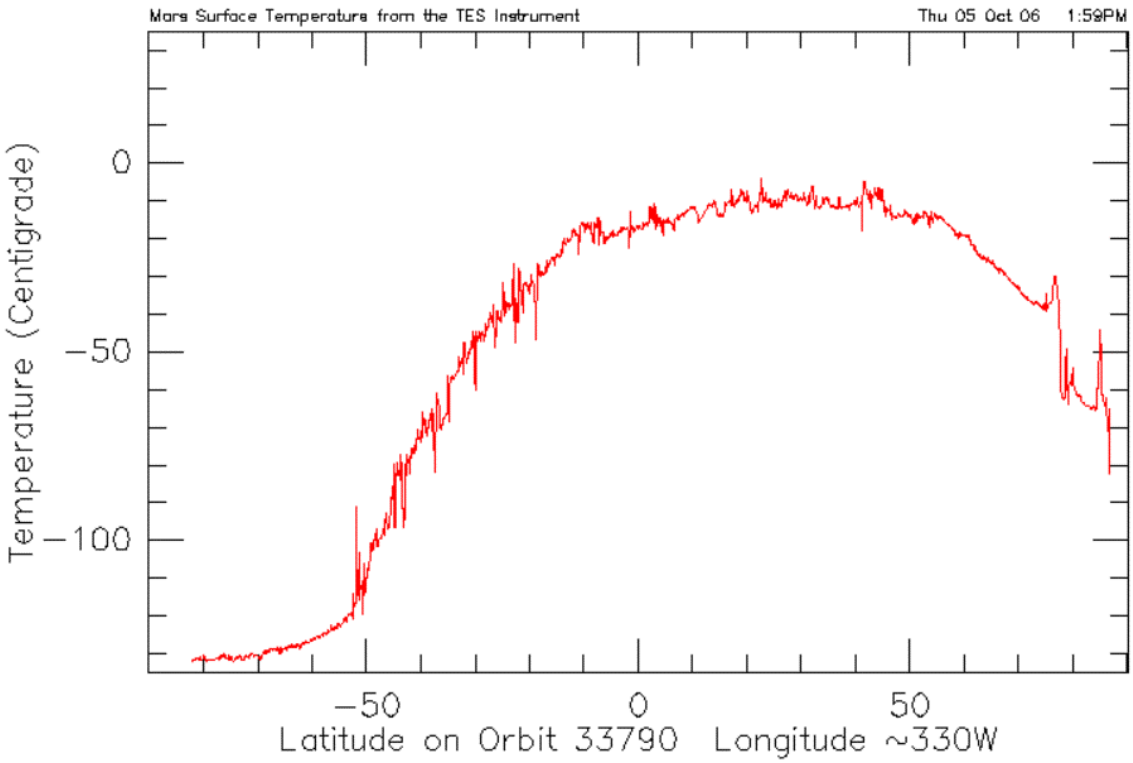

Figure 43: Observed pole to pole Martian surface temperatures from TES data.

Reducing heat transport, C, to sequester heat in the equatorial regions and glaciate polar regions results in model breakdown at $C < 1.74$ as specific lines of longitude glaciate completely compared to a cold but near uniform surface for other longitudes (**Figure 45**). Further changes to the 2D model are necessary before it can be used to reliably model Mars.

a.

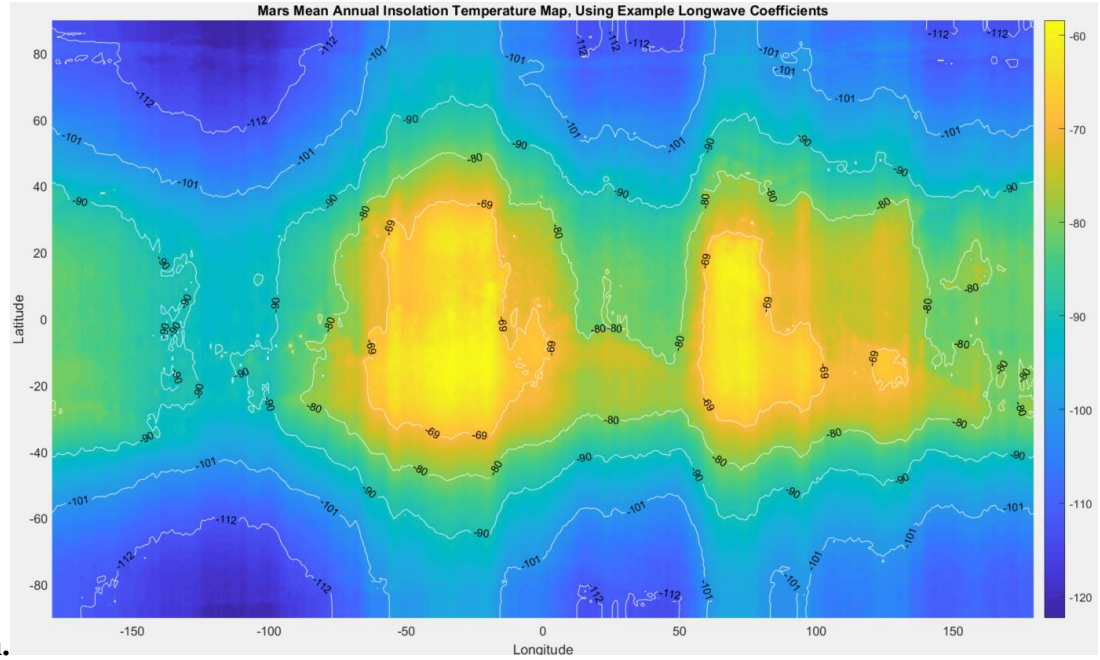

b.

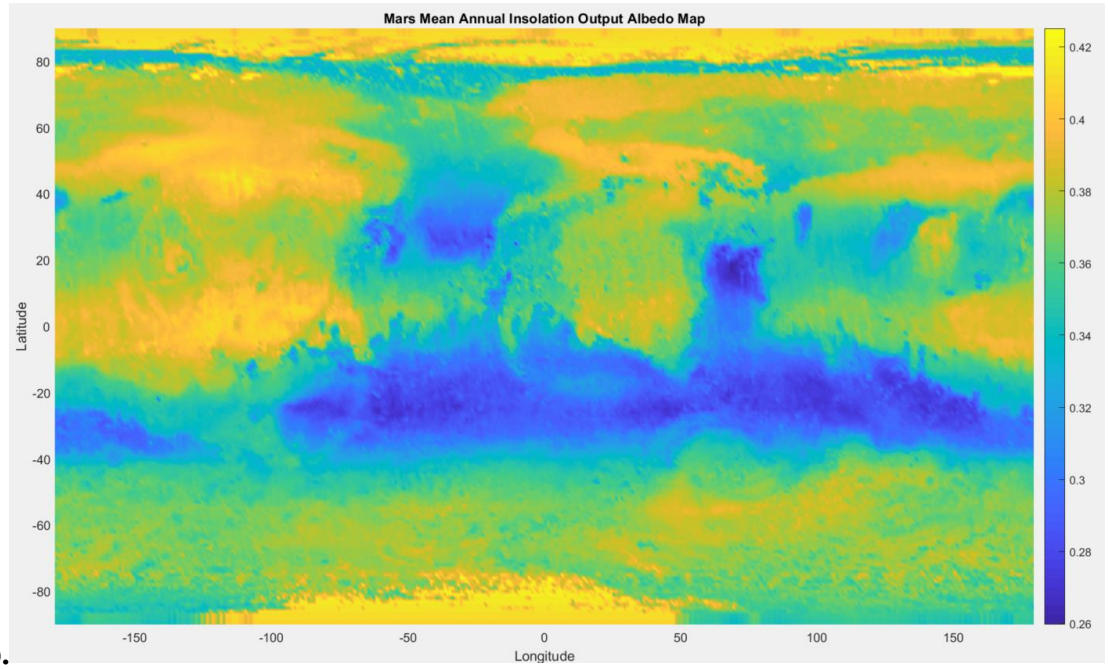

Figure 44: Example output temperature and albedo maps using TES initial albedo, and globally averaged starting temperature of -63°C.
S = 586.2 W/m^2, α_{ice} = 0.64, Tcrit = -123°C, β = 25.19°, e = 0.0935
Test parameters: CALB = 0.5, A = 120, B = 0.250732, and C = 1.80.

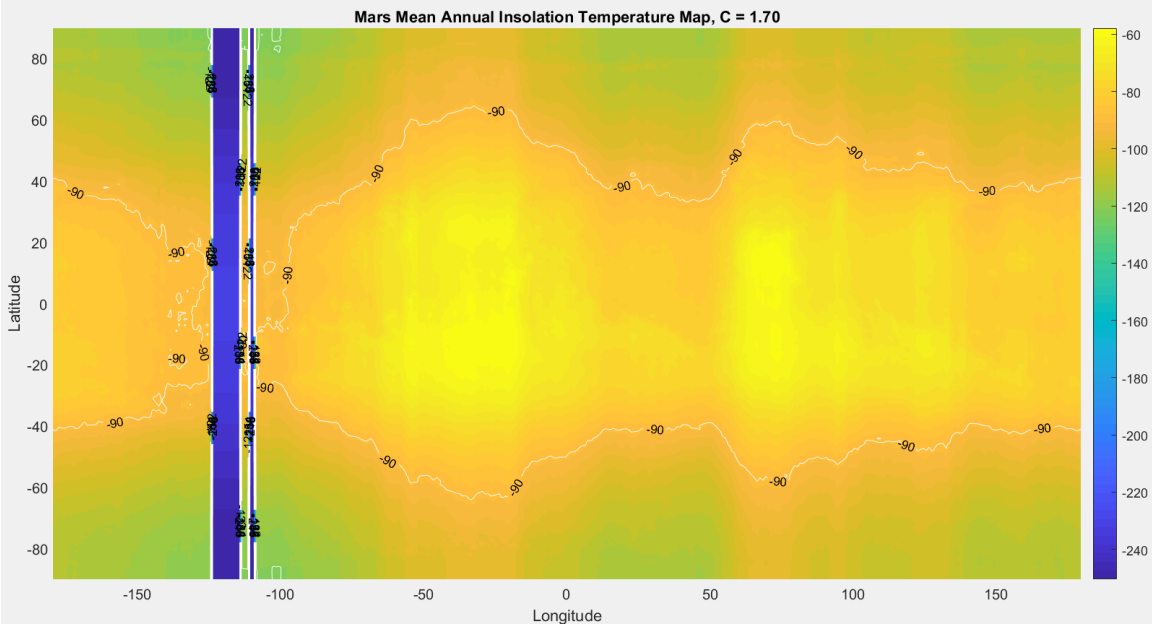

Figure 45: Mars EBM temperature output map using reduced latitudinal heat transport (C) = 1.70

5.6: Pluto

Pluto's atmosphere is dominated by nitrogen, which freezes at -210°C at Pluto's atmospheric pressure, 10 μbar (NASA, 2016). Thus, TCRIT was determined to be -210°C for purposes of modeling ice on Pluto. H_2O and CO_2 will always present as solid ice at these temperatures and pressures. This far from the Sun, Pluto only receives an S of 0.873 W/m^2.

NASA's New Horizons mission in 2015 revealed important information about Pluto, first, that its surface pressure has changed dramatically recently, as nearly half of its atmosphere has frozen onto the planet's surface giving us this new lower value of 10 μbar compared to much higher measurements from Earth previously (NASA, 2015). New Horizons also revealed detailed surface geology and volatile distribution maps (Grundy et

al., 2016). This is useful for defining an input albedo, which varies drastically across the planet. The equatorial region displays both light and darker regions (**Figure 49**), differing in temperature and volatile deposition (Earle et al., 2017). Pluto's nitrogen ice albedo (α_{ice}) has a reflectivity similar to Earth's water ice, at 0.62 (Lewis et al., 2020).

Pluto's obliquity is defined relative to the standard orbital plane orientation of the Solar System, although its positive (North) pole is opposite to that of all of the other planets. Currently, the obliquity is 119.59° and varies between 103° at a minimum and 128° at a maximum (NASA, 2016; Earle et al., 2017).

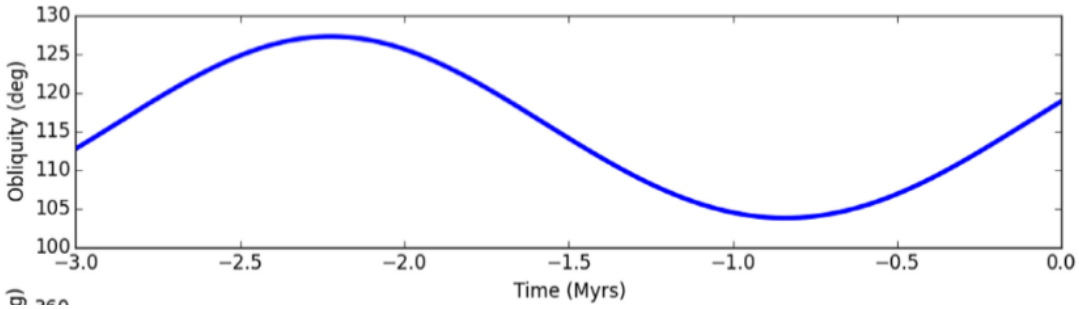

Figure 46: Variations in Pluto's obliquity over the last 3 myr (Earle et al., 2017).

Pluto's orbital eccentricity varies between 0.21 and 0.27 (Ito and Tanikawa, 2002), with a current value of 0.24880766 (NASA, 2016). As with the gravitational impact of Jupiter on Earth's and Mars's eccentricities, Pluto experiences orbital eccentricity variations primarily due to resonance with its nearest neighbor, Neptune (Ito and Tanikawa, 2002).

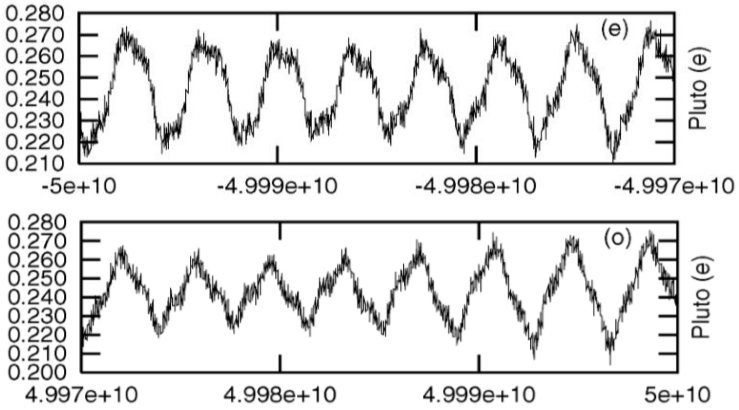

Figure 47: Pluto's orbital eccentricity for two 30 myr-long models (Ito and Tanikawa, 2002).

Initial albedo values for Pluto were derived from zonal averages in **Figure 48** (Buie et al., 1992). Updated albedo data from New Horizons would need to be among the objectives for future use of the model in order to improve outputs, and as such the imprecise model results are not presented here.

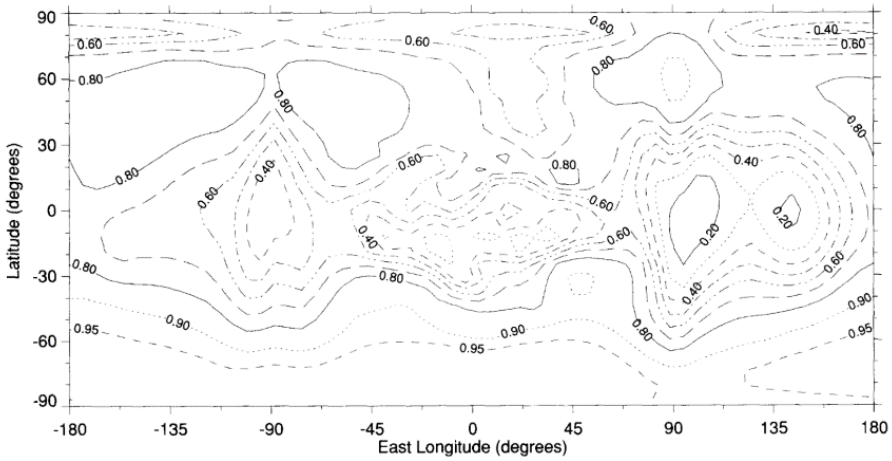

Figure 48: Albedo map of Pluto, used as input values based on a latitudinally zoned average (Buie et al., 1992).

Using a map of albedo, nitrogen ice can also be used to determine a higher resolution input albedo (Buratti et al., 2017, Lewis et al., 2020).

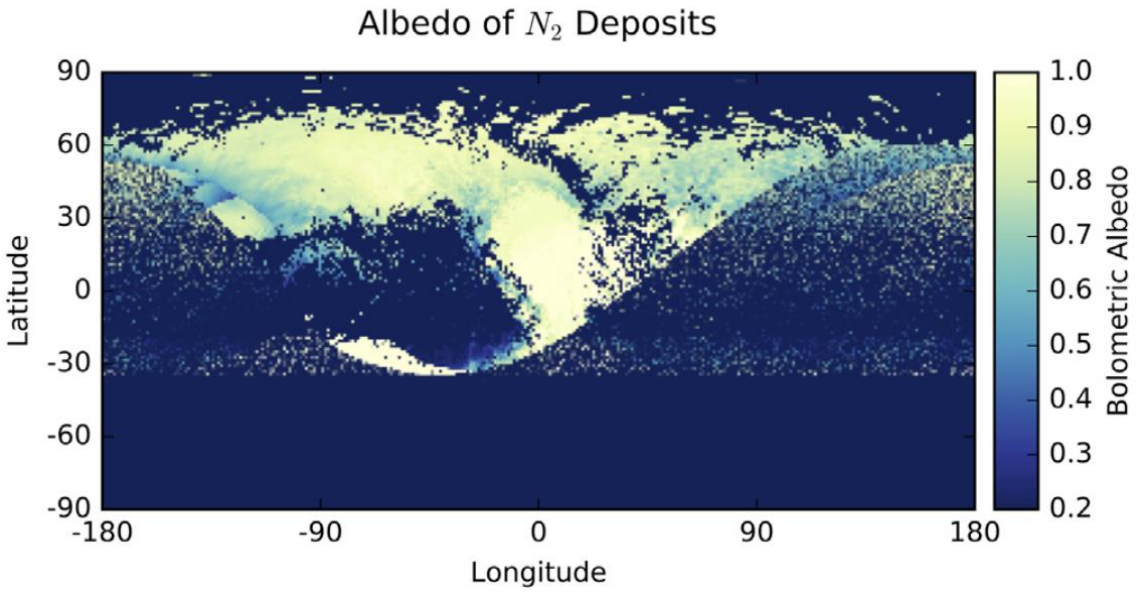

Figure 49: Bolometric albedo from Buratti et al. (2017) modeling deposits of nitrogen ice across Pluto's surface.

CHAPTER 6: CONCLUSIONS

Using a modernized energy balance model to simulate Earth and other planetary bodies in several model variations of increasing complexity, this study incorporated novel solutions to determine the significance of multiple orbital and climate related parameters. Enhancements to previous energy balance models using a conglomerate of interdisciplinary studies and unique solutions allowed for several accomplishments.

- A catalog of easy-to-use zero-dimensional, one-dimensional, and two-dimensional EBMs.
- Budyko-Sellers style energy balance modeling, examining the influence of solar flux on temperature and ice-line location with ice-albedo feedback is revitalized in the MATLAB environment with a Graphic User Interface (GUI).
- Milankovitch cycles are added to energy balance modeling for the first time.
- Orbitally forced mean annual insolation using sixth order Legendre series expansion is added to allow for basic modeling for any star-orbiting planet with non-zero obliquity and orbital eccentricity, and a rotation rate that is significantly faster than that of its orbit.
- Monthly insolation solutions are provided as inputs for three time slices, present-day (0ka), LGM (24ka) and Eemian Interglacial (128ka);

and the influence of obliquity in the absence of global circulation is highlighted.

- The inclusion and comparison of binary annual land and ocean albedo and realistic monthly albedo as inputs, where realistic albedo was shown to drastically improve Earth outputs.
- EBM iterations were increased to ensure that equilibrium is achieved.
- Many research questions can be pursued using the revamped, simple energy balance models provided, and preliminary discussion for use in non-Earth systems was introduced.
- Varied tests of input variable significance on climate results were conducted.

Initial albedo including surface, cloud, and ice, as well as changes to insolation-forced parameters such as coefficients A and B were revealed to result in the most significant changes to a system. Meanwhile, variations in initial temperatures were among the least significant to the outputs of the model.

The different models allowed for a more in depth look at the importance of specific model parameters, as limitations were placed to allow for a more generalized and accessible model. Both in-depth Earth studies and cursory exoplanetary research benefit from the simplistic modeling approach. The less computationally intensive modeling approach facilitates faster results about more specific inquiries.

Previous energy balance modeling was reviewed, and the tools for realistic simple modeling were created to assist in climate modeling of Earth, and the first steps are taken to introduce a comprehensive model to single-model multi-planetary research. Future work will entail the inclusion of more in-depth cloud and atmospheric forcing in the model. Cloud fraction profiles would need to be made time variable, and sensitivity tests should be run to determine the impact of what cloud forcing would accomplish. The addition of cross-longitudinal circulation, atmospheric diffusion, and a more complex heat capacity parameter that changes between land and ocean would improve zonal heat transfer. Model ability to work with non-Earth systems would need to be refined through the inclusion of updated OLR and heat transport classifications.

Another advancement would be to provide an outer loop to take output albedo and temperature maps and input them into a new run with a change in insolation. This can take place at multiple levels, such as: month-to-month, year-to-year for a single month, and year-to-year for annual average.

REFERENCES

Barkstrom, B. R., E. F. Harrison, and R. B. Lee, 1990. Earth Radiation Budget Experiment, Preliminary seasonal results. EOS Transactions, American Geophysical Union, 71. https://iridl.ldeo.columbia.edu/SOURCES/.NASA/.ERBE/.ERBS/.total/.albedo/

Barry, L., Craig, G. C., Thuburn, J. (2002). Poleward heat transport by the atmospheric heat engine. *Nature*, 415, 774-777. https://doi.org/10.1038/415774a

Berger, A. (1978). Long-Term Variations of Caloric Insolation Resulting from the Earth's Orbital Elements. *Quaternary Research 9, 139-167.* https://doi.org/10.1016/0033-5894(78)90064-9

Berger, A., Loutre, M.F., Yin, Q. (2010). Total irradiation during any time interval of the year using elliptic integrals. *Quaternary Science Reviews, Volume 29, Issues 17-18, 1968-1982.* https://doi.org/10.1016/j.quascirev.2010.05.007

Budyko, M. (1969). The effects of solar radiation on the climate of the Earth. *Tellus*, 21:5, 611-619. https://doi.org/10.3402/tellusa.v21i5.10109

Buie, M., Tholen, D., Horne, K. (1992). Albedo Maps of Pluto and Charon: Initial Mutual Event Results. *Icarus* 97, 211-227. https://doi.org/10.1016/0019-1035(92)90129-U

Buratti, B. J., Hofgartner, J. D., Hicks, M. D., Weaver, H. A., Stern, S. A., Momary, T., Mosher, J. A., Beyer, R. A., Verbiscer, A. J., Zangari, A. M., Young, L. A., Lisse, C. M., Singer, K., Cheng, A., Grundy, W., Ennico, K., Olkin, C. B. (2017). Global albedos of Pluto and Charon from LORRI New Horizons observations. Icarus, 287, 207-217. https://doi.org/10.1016/j.icarus.2016.11.012

Chavas, D. (2020). land_or_ocean.m, MATLAB Central File Exchange. https://www.mathworks.com/matlabcentral/fileexchange/45268-land_or_ocean-m

Christensen, P. R., Bandfield, J. L. Hamilton, V. E., Ruff, S. W., Kieffer, H. H., Titus, T. N., Malin, M. C., et al. (2001). Mars Global Surveyor Thermal Emission Spectrometer experiment: Investigation description and surface science results. *Journal of Geophysical Research, 106*(E10), 23823-23872. https://doi.org/10.1029/2000JE001370

Earle, A., Binzel, R., Young, L., Stern, S., Ennico, K., Grundy, W., Olkin, C., Weaver, H., & the New Horizons Geology and Geophysics Imaging Team. (2017). Long-term

surface temperature modeling of Pluto. *Icarus* 287, 37-46, https://doi.org/10.1016/j.icarus.2016.09.036

Ellis, J., Vonder Haar, T. (1976). Zonal average earth radiation budget measurements from satellites for climate studies. *Atmospheric Science Paper No. 240*. https://ntrs.nasa.gov/search.jsp?R=19770006645

Feulner, G. (2012). The faint young Sun problem. Reviews of Geophysics, 50, RG2006 1-29, https://doi.org/10.1029/2011RG000375

Fitzpatrick, R., (2012). An Introduction to Celestial Mechanics. Cambridge University Press. https://doi.org/10.1017/CBO9781139152310

Gotwals, B. (1998). Energy Balance Model. The Shodor Education Foundation. http://www.shodor.org/master/environmental/general/energy/energy.html

Graves, C., Lee, W. H., North, G. (1993). New Parameterizations and Sensitivities for Simple Climate Models. JOURNAL OF GEOPHYSICAL RESEARCH, VOL. 98, NO. D3, PAGES 5025-5036. https://doi.org/10.1029/92JD02666

Grundy, W. M., Binzel, R. P., Buratti, B. J., Cook, J. C., Cruikshank, D. P., Dalle Ore, C. M., Earle, A. M., Ennico, K., Howett, C. J. A., Lunsford, A. W., Olkin, C. B., Parker, A. H., Philippe, S., Protopapa, S., Quirico, E., Reuter, D. C., Schmitt, B., Singer, K. N., Verbiscer, A. J., Beyer, R. A., Buie, M. W., Cheng, A. F., Jennings, D. E., Linscott, I. R., Parker, J. Wm., Schenk, P. M., Spencer, J. R., Stansberry, J. A., Stern, S. A., Throop, H. B., Tsang, C. C. C., Weaver, H. A., Weigle II, G. E., Young, L. A., and the New Horizons Science Team. (2016). Surface Compositions across Pluto and Charon. *Science*. Vol 351, Issue 6279. https://doi.org/10.1126/science.aad9189

Hansen, J., Ruedy, R., Sato, M., Lo, K. (2010). Global Surface Temperature Change. Reviews of Geophysics, 48, RG4004, 1-29, https://doi.org/10.1029/2010RG000345

Hartmann, D. (2016). Global Physical Climatology. Second Edition. Elsevier Science, 485 p., https://doi.org/10.1016/C2009-0-00030-0

Hays, J.D., Imbrie, J., Shackleton, N.J. (1976). Variations in the Earth's Orbit: Pacemaker of the Ice Ages. *Science.* Vol. 194, Issue 4270, pp. 1121-1132 https://doi.org/10.1126/science.194.4270.1121

Hinnov, L. (2013). Cyclostratigraphy and its revolutionizing applications in the earth and planetary sciences. Geological Society of America Bulletin 2013;125, no. 11-12;1703-1734, https://doi.org/10.1130/B30934.1

Hoffert, M., Callegari, A., Hsieh, C., Ziegler, W. (1981). Liquid Water on Mars: An Energy Balance Climate Model for CO_2/H_20 Atmospheres. *Icarus* 47, 112-129, https://doi.org/10.1016/0019-1035(81)90096-8

Huybers, P., et al. (2006). Early Pleistocene Glacial Cycles and the Integrated Summer Insolation Forcing. *Science*. 313, 508-511. https://doi.org/10.1126/science.1125249

Ito, T., Tanikawa, K. (2002). Long-term integrations and stability of planetary orbits in our Solar system, *Monthly Notices of the Royal Astronomical Society*, Volume 336, Issue 2, 483–500, https://doi.org/10.1046/j.1365-8711.2002.05765.x

Jones, P. D., New, M., Parker, D. E., Martin, S., Rigor, I. G. (1999). Surface air temperature and its changes over the past 150 year. Reviews of Geophysics, 37, 173-199, https://doi.org/10.1029/1999RG900002

Kopp, G., Lean, J.L. (2011). A new, lower value of total solar irradiance: Evidence and climate significance, *Geophysical Research Letters*, 38, L01706, https://doi.org/10.1029/2010GL045777

Kostadinov, T. S., and Gilb, R. (2014). Earth Orbit v2.1: a 3-D visualization and analysis model of Earth's orbit, Milankovitch cycles and insolation. Geoscience Model Dev., 7, 1051-1068, https://doi.org/10.5194/gmd-7-1051-2014

Laskar, J., Robutel, P., Joutel, F., Gastineau, M., Correia, A.C.M., Levrard, B. (2004). A long-term numerical solution for the insolation quantities of the Earth. *Astronomy & Astrophysics*, 428, 261–285, https://doi.org/10.1051/0004-6361:20041335

Laskar, J., Correia, A. C. M., Gastineau, M., Joutel, F., Levrard, B., Robutel, P. (2004). Long term evolution and chaotic diffusion of the insolation quantities of Mars. *Icarus*, 170, 343–364, https://doi.org/10.1016/j.icarus.2004.04.005

Lean, J.L. (2010), Cycles and trends in solar irradiance and climate. *WIREs Climate Change*, Royal Geographical Society, 1(1), 111-122, https://doi.org/10.1002/wcc.18

Lewis, B. L., Stansberry J. A., Holler, B. J., Grundy, W. M, Schmitt, B., Protopapa, S., Lisse C., Stern S. A., Young, L., Weaver, H. A., Olkin, C., Ennico, K., and the New Horizons Science Team. (2020). Distribution and energy balance of Pluto's nitrogen ice, as seen by New Horizons in 2015. Icarus, 2020-01. P.113633. https://doi.org/10.1016/j.icarus.2020.113633

Li, J., Scinocca, J., Lazare, M., McFarlane, N., von Salzen, K. and Solheim, L. (2006). Ocean Surface Albedo and Its Impact on Radiation Balance in Climate Models. *Journal of Climate*, **19**, 6314–6333, https://doi.org/10.1175/JCLI3973.1.

Lindzen, R., Farrell, B. (1977). Some Realistic Modifications of Simple Climate Models. *Journal of Atmospheric Sciences*, 34, 1487-1501. https://doi.org/10.1175/1520-0469(1977)034<1487:SRMOSC>2.0.CO;2

Loeb, N.G., Doelling, D.R., Wang, H., Su, W., Nguyen, C., Corbett, J.G., Liang, L., Mitrescu, C., Rose, F.G., and Kato, S. (2018). Clouds and the Earth's Radiant Energy System (CERES) Energy Balanced and Filled (EBAF) Top-of-Atmosphere (TOA) Edition-4.0 Data Product. *Journal of Climate*, **31**, 895-918, https://doi.org/10.1175/JCLI-D-17-0208.1

Longhi, J. (2006). Phase equilibrium in the system CO_2-H_2O: Application to Mars, *Journal of Geophysical Research, Planets*, 111, https://doi.org/10.1029/2005JE002552

Lourens, L., and Tuenter, E. (2009). Chapter 5: The Role of Variations of the Earth's Orbital Characteristics in Climate Change, in Letcher, T.M., ed., Climate Change: Observed Impacts on Planet Earth, Elsevier Science, 103-123, https://doi.org/10.1016/B978-0-444-53301-2.00005-1

Mcgehee, R., Lehman, C. (2012). A Paleoclimate Model of Ice-Albedo Feedback Forced by Variations in Earth's Orbit. *SIAM Journal on Applied Dynamical Systems* 11.2: 684–707. https://doi.org/10.1137/10079879X

McGuffie, K., Henderson-Sellers, A. (2014). *A Climate Modelling Primer, Fourth Edition.* Wiley Blackwell, 456 p., https://doi.org/10.1080/00207233.2014.926135

McGuffie, K., Henderson-Sellers, A. (2005). *A Climate Modelling Primer, Third Edition.* John Wiley & Sons, Ltd., 280 p., https://doi.org/10.1002/0470857617

McGuffie, K., Henderson-Sellers, A. (1997). *A Climate Modelling Primer, Second Edition.* John Wiley & Sons, Ltd., 268 p.

McGuffie, K., Henderson-Sellers, A. (1988). *A Climate Modelling Primer, First Edition.* John Wiley & Sons, Ltd., 234 p.

Milankovitch, M. (1941). *Kanon der Erdbestrahlung und seine Anwendung auf das Eiszeitenproblem*: Royal Serbian Academy, Section of Mathematical and Natural Sciences, Belgrade, 633 p. (and 1998 reissue in English: *Canon of Insolation and the Ice-Age Problem:* Belgrade, Serbian Academy of Sciences and Arts, Section of Mathematical and Natural Sciences, 634 p.).

Nadeau, A., McGehee, R. (2017). A simple formula for a planet's mean annual insolation by latitude. *Icarus* 291, 46-50, https://doi.org/10.1016/j.icarus.2017.01.040

Nakamura, T., Tajika, E. (2001). Stability and evolution of the climate system of Mars. *Earth Planets Space*, 53, 851-859, https://doi.org/10.1186/BF03351682

NASA Earth Observatory. (2002). *Global Albedo*. MODIS Land Science Team. https://earthobservatory.nasa.gov/images/2599/global-albedo

NASA. (2015). New Horizons Reveals Pluto's Atmospheric Pressure Has Sharply Decreased. NASA/Johns Hopkins University Applied Physics Laboratory/Southwest Research Institute. https://www.nasa.gov/feature/new-horizons-reveals-pluto-s-atmospheric-pressure-has-sharply-decreased

NASA Space Science Data Coordinated Archive. (2016). *Planetary Fact Sheets.* NASA Goddard Space Flight Center. https://nssdc.gsfc.nasa.gov/planetary/factsheet/

National Snow and Ice Data Center. (2020). All About Sea Ice. National Snow and Ice Data Center. https://nsidc.org/cryosphere/seaice/index.html

North, G. (1975). Theory of Energy-Balance Climate Models. *Journal of Atmospheric Sciences*. 32. 2033-2043. https://doi.org/10.1175/1520-0469(1975)032<2033:TOEBCM>2.0.CO;2

North, G., Cahalan, R., Coakley, J., (1981). Energy Balance Climate Models. *Reviews of Geophysics and Space Physics.* 19. 91-121. https://doi.org/10.1029/RG019i001p00091

North, G., Kim, K. (2017). *Energy Balance Climate Models.* Wiley-VCH, 369 p., https://doi.org/10.1002/9783527698844

Passos, D., Brandão, S., Lopes, I. (2007). On the luminosity evolution of the Sun during the last 7 millennia. *Advances in Space Research.* 40. 990–995, https://doi.org/10.1016/j.asr.2007.02.095

Raymo, M., Lisiecki, L., Nisancioglu, K. (2006). Plio-Pleistocene Ice Volume, Antarctic Climate, and the Global d18O Record. *Science*. Vol 313. 492-495. https://doi.org/10.1126/science.1123296

Raymo, M., Huybers, P. (2008). Unlocking the mysteries of the ice ages. *Nature*. Vol 451. 284-285. https://doi.org/10.1038/nature06589

Seitz, R., 2011. Bright water: hydrosols, water conservation and climate change. *Climatic Change*, *105*(3-4), pp.365-381. https://doi.org/10.1007/s10584-010-9965-8

Sellers, W. (1969). A Global Climate Model Based on the Energy Balance of the Earth-Atmosphere System. *Journal of Applied Meteorology*, 8, 392-400, https://doi.org/10.1175/1520-0450(1969)008<0392:AGCMBO>2.0.CO;2

Siler, N., Roe, G., Armour, K. (2018). Insights into the Zonal-Mean Response of the Hydrologic Cycle to Global Warming from a Diffusive Energy Balance Model. Journal of Climate, 31 (18). 7481-7493. https://doi.org/10.1175/JCLI-D-18-0081.1

Touma, J., Wisdom, J. (1993). The Chaotic Obliquity of Mars. *Science*, 259(5099), 1294-1297. https://doi.org/10.1126/science.259.5099.1294

Walsh, J., Rackauckas, C. (2015). On the Budyko-Sellers energy balance climate model with ice line coupling. *Discrete and Continuous Dynamical Systems*, Series B, 20(7), 2187-2216, https://doi.org/10.3934/dcdsb.2015.20.2187

Ward, W. (1974). Climatic Variations on Mars, 1. Astronomical Theory of Insolation. *Journal of Geophysical Research*, 79(24), 3375-3386, https://doi.org/10.1029/JC079i024p03375

Warren, S., Schneider, S. (1979). Seasonal Simulation as a Test for Uncertainties in the Parameterizations of a Budyko-Sellers Zonal Climate Model. *Journal of the Atmospheric Sciences*, 36, 1377-1391. https://doi.org/10.1175/1520-0469(1979)036<1377:SSAATF>2.0.CO;2

Zachos, J., Pagani, M., Sloan, L., Thomas, E., Billups, K. (2001). Trends, rhythms, and aberrations in global climate 65 Ma to present, *Science*, 292, 686–693. https://doi.org/10.1126/science.1059412

BIOGRAPHY

Christian Johann Taubenberger graduated from West Springfield High School, Springfield, Virginia, in 2013. He received his Bachelor of Science in biology, with a focus in environmental conservation, and a minor in astronomy, from George Mason University in 2017. He has been working on his Master of Science in the Earth Systems Science Program at George Mason University under Linda Hinnov since Spring 2018. His goal is to direct his diverse physical and life science background into the fields of astrobiology and Earth science at NASA Goddard, post-graduation.